Multi-compartmental nature of nanoparticles and their biological effects

Dissertation
zur Erlangung des Doktorgrades
an der Fakultät für Mathematik, Informatic und Naturwissenschaften
Fachbereich Physik
der Universität Hamburg

vorgelegt von

Bing Qi

Hamburg

2022

Gutachter/innen der Dissertation:	Prof. Dr. Wolfgang J. Parak Prof. Dr. Viacheslav Nikolaev
Zusammensetzung der Prüfungskommission:	Prof. Dr. Florian Grüner Prof. Dr. Wolfgang J. Parak Prof. Dr. Viacheslav Nikolaev Prof. Dr. Alf Mews Dr. Neus Feliu Torres
Vorsitzende/r der Prüfungskommission:	Prof. Dr. Florian Grüner
Datum der Disputation	1-SEP-2022
Vorsitzender Fach-Promotionsausschuss PHYSIK:	Prof. Dr. Wolfgang J. Parak
Leiter des Fachbereichs PHYSIK:	Prof. Dr. Günter H. W. Sigl
Dekan der Fakultät MIN:	Prof. Dr. Heinrich Graener

Abstract

When the size of materials is reduced to the nanoscale, there always come with some unique properties that differ from their bulk counterparts, such as fluorescent, superparamagnetic, plasmonic, etc. Particularly, in recent years, the advancements in engineering nanoparticles (NPs) have led to diverse applications in biomedical fields, including biosensors, bioimaging, drug delivery, and vaccines. However, in most cases, NPs were applied upon exposure to a biological environment, which will inevitably adsorb some biological molecules, such as proteins, sugars, lipids, nuclear acids, as well as some ions. In that case, NPs will form a biomolecular layer, called “protein corona”. Up to now, various studies reported that protein corona plays a critical role in the interaction between NPs and cells or even the body. For example, the protein corona can reduce the cellular uptake efficiency, alter biodistribution in our bodies, and decrease the toxicity of NPs both in vitro and in vivo. The protein corona can also decrease the targeting capability of NPs by covering some targeting ligands. In addition, to keep the colloidal stability in biological fluids, NPs are always modified with different surface ligands or polymers. Therefore, NPs should not be regarded as homogeneous entities anymore, but as hybrid NPs with multi-compartments comprising of inorganic core, engineered polymer shell, and biomolecular layer. Furthermore, since most studies previously focused on the qualitative aspects, it is challenging to compare those results among different studies. Thus, there is a need to study the multi- compartmental NPs and their interaction with biological environments in a quantitative way. In this thesis, we divided it into three parts and quantitatively evaluated the biological effects of multi-compartmental NPs. In the first part, inductively coupled plasma mass spectrometry (ICP- MS) was introduced to quantify the different biodistributions of gold (Au) and iodine, in particular, an Au NPs library with different sizes and surface ligands was prepared, and the impacts of size and surface chemistry on biodistributions of NPs was evaluated. In the second part, the multi-compartmental NPs were labeled with different elements. Upon incubation with human cervical cancer cells (HeLa), the association between protein corona and cellular uptake was quantitatively investigated. The important role of surface chemistry on the binding affinity toward different proteins was proposed. In the third part, the protein corona of NPs by conjugating atenolol with bovine serum albumin (BSA) was exploited. With the transcytosis capability of BSA, we can bypass the barrier of capillary, deliver atenolol to cardiomyocytes, and selectively bind the subpopulation of β1- adrenergic receptors. Thus, the therapeutic efficacy of atenolol compared to the small molecules was further improved.

Zusammenfassung

Wenn die Größe von Materialien auf die Nanoskala verringert wird, treten immer einzigartige Eigenschaften auf, die sich von ihren Gegenstücken im Volumen unterscheiden, zum Beispiel Fluoreszenz, Superparamagnetismus, Plasmonen, usw. Vor allem hat die Entwicklung von Nanopartikeln (NPs) in den letzten Jahren verschiedenartige Anwwendungen in biomedizinischen Bereichen wie Biosensoren, Bioimaging, Arzneimittelabgabe sowie Impstoffe angeführt. Trotzdem legen NPs in meisten Fällen in biologischer Umgebung frei und danach adsobieren unweigerlich einige biologische Moleküle z.B. Proteine, Zucker, Lipide, Nuklearsäuren und manche Ionen. Dann bilden NPs eine biomolekulare Schicht, die als „Proteinkorona“ bezeichnet wird. Laut bisheriger Ergründung spielt die Proteinkorona eine entscheidende Rolle in der Wechselwirkung zwischen NPs und Zellen bzw. NPs in Körpern. Proteinkorona kann beispielsweise zelluläre Aufnahmeeffizienz verschlechtern, Bioverteilung in Körpern verändern und Giftigkeit der NPs in vitro sowie vivo verringern. Die Proteinkorona kann auch die Targeting-Fähigkeit von NPs verringern, indem sie einige Targeting-Liganden abdeckt.Wegen Abdeckung von Zielliganden kann Proteinkorona ebenso Targeting-Fähigkeit der NPs verschwächen. Außerdem sind NPs immer mit unterschiedlichen Oberflächenliganden oder Polymeren modifiziert, um kolloidale Stabilität in biologischen Flüssigkeiten zu halten. Deshalb sollten NPs nicht mehr als homogene Einheiten betrachtet werden, sondern als hybride NPs mit mehreren Kompartimenten, die aus einem anorganischen Kern, einer konstruierten Polymerhülle und einer biomolekularen Schicht bestehen. Heute konzentieren sich meiste Studien auf der qualitativen Aspekten. Trotzdem ist es schwierig, die Ergebnisse zwischen verschiedenen Studien zu vergleichen. Daher besteht die Notwendigkeit, die Multikompartiment-NPs und ihre Wechselwirkung mit biologischen Umgebungen quantitativ zu untersuchen. In dieser Arbeit sind die biologischen Wirkungen von NPs mit mehreren Kompartimenten - aufgeteilt in drei Teile - quantitativ bewertet. Im ersten Teil ist die induktiv gekoppelte Plasma-Massenspektrometrie (ICP-MS) eingeführt, um die unterschiedlichen Bioverteilungen von Gold (Au) und Jod zu quantifizieren, insbesondere sind Au-NPs mit unterschiedlichen Größen und Oberflächenliganden vorbereitet und Auswirkungen der Größe sowie Oberflächenchemie zur Bioverteilung von NPs verglichen. Im zweiten Teil sind die Multikompartimente von NPs mit verschiedenen Elementen markiert. Nach der Inkubation mit menschlichen Gebärmutterhalskrebszellen (HeLa) sind jeweils ein Zusammenhang zwischen Proteinkorona und zellulärer Aufnahme quantitativ bewertet und wichtige Rolle der Oberflächenchemie für die Bindungsaffinität zu verschiedenen Proteinen eingebracht. Im dritten Teil ist Proteinkorona von NPs weiter verwandt, indem Atenolol mit Rinderserumalbumin (BSA) konjugiert ist. Mit der Transzytosefähigkeit von BSA können die Kapillarbarriere umgegangen, Atenolol an Kardiomyozyten abgegeben und die Subpopulation von β1-adrenergen Rezeptoren selektiv verbunden werden. Damit kann sich die therapeutische Wirksamkeit von Atenolol im Vergleich zu den kleinen Molekülen weiter

verbessern.

Table of Contents

1 Introduction

What is nano? The word 'nano' originated from a Greek prefix, meaning 'dwarf'. Now it refers to a length scale, which is a billionth of a meter (10^{-9} m). It is no doubt this tiny scale is invisible to our naked eyes. In nature, there are various natural or synthetic materials at the nanoscale, including hemoglobin, antibody, DNA, virus, volcanic ash, exhaust from vehicles, etc. Taking the COVID-19 pandemic as an example, the enveloped SARS-Cov-2 virus with about 100 nm diameter infected host cells via the high affinity between receptor- binding domain (RBD) of spike protein from the viruses and ACE2 receptor from host cells[1-3]. The virus hijacks host cells and replicates more viral RNA for further infection through a series of membrane fusion processes. Additionally, the widely used mRNA vaccine with an average diameter of 100 nm, composed of mRNA chain in the core and lipid NPs as a shell, benefits people against viruses via triggering an immune response in our body and plays a significant role in ending the global pandemic[4]. Therefore, there is an urgent need to study nanomaterials surrounding our lives and how they can be applied in our daily lives. This process is called nanotechnology. According to the strategic plan of the National Nanotechnology Initiative(NNI), nanotechnology is defined as a study about the understanding and control of matter at dimensions between 1 and 100 nm where unique phenomena enable novel applications[5]. Like the mRNA vaccine aforementioned, it is an excellent application of nanotechnology in medicine.

1.1 A glance at nanotechnology history

The history of nanotechnology can be traced back to the early medieval period, the mystery of the Roman Lycurgus cup, which is jade green when light is reflected in front of it while turns red when light is transmitted from behind, was not revealed until the 1990s. The tiny silver (Ag) and Au NPs with a diameter of ca. 50 nm distributed in the glass gives rise to different optical phenomena. Also in the middle age, the church windows shone with different luminous colors due to the presence of noble metal NPs. In the 17th century, Damascus blades with extraordinary strength and flexibility were used by Muslims, high resolution transmission electron microscopy images indicate the steel containing carbon nanotubes and cementite nanowires could explain the remarkable mechanical properties[6-8]. All of the cases demonstrated the unique properties of nanomaterials compared to their bulk counterpart. Although the long history of applications of nanotechnology, the development of modern nanotechnology began in the last decades. The lecture "There's plenty of room at the bottom" presented by American physicist and Nobel Prize laureate Richard Feynman was considered a sign of the introduction of nanotechnology conception. And 15 years later, Japanese engineering professor, Norio Taniguchi, coined the term nanotechnology[9]. The real bloom of nanotechnology began in the 1980s. The invention of the scanning tunneling microscope (STM), followed by the emergence of the atomic force

microscope (AFM) and scanning probe microscope (SPM), etc. highly promoted the progress of nanotechnology[6]. With the help of advanced instruments, a series of new class carbon-based nanomaterials were discovered, including fullerenes[10], carbon dots[11] as well as graphene[12-13]. And diverse nanomaterials, such as inorganic, organic as well as natural nanomaterials can be prepared using different physical and chemical methods or characterized, nanotechnology is being applied in many aspects including electronics, biosensing, bioimaging, drug delivery, catalysis, etc. And it is attracting scientists from different fields like physics, chemistry, biology, pharmacy, medicine, engineering, and computer science[14-18]. In this thesis, we mainly focus on the biological applications of nanotechnology. For other fields, we recommend referring to other books or reviews[19-21].

1.2 Multi-compartmental nature of NPs in a biological environment

When it comes to biological effects, nanomaterials or NPs (In the following contents, we mainly use NPs) will be inevitably exposed to biofluids. Unlike the NPs in cups, glass, or swords, which are commonly within or on the surface of a substrate, NPs always tend to aggregate or agglomerate in solution due to some weak interaction among different NPs, including Van der Waals force, electrostatic interaction, hydrophobic interaction, hydrogen bonds, etc[22]. Therefore, good colloidal stability is a prerequisite for NPs application in biological environments[23-24]. To keep NPs stable in solution, generally, a surface chemistry procedure is necessary. Conceptually, NPs in biological media can be categorized into a multi-compartmental system (NPs' core, engineered polymer shell, and the biomolecular layer via adsorption or chemical linkage). The NPs' core (mainly refers to as the inorganic core in this thesis) is the initial NPs, which endows some physical properties, like being plasmonic, magnetic, and fluorescent. The engineered polymer shell provides colloidal stability and allows NPs to be individual in solution. And the biomolecular layer gives NPs a biological identity, which might be good or bad[25-26].

NP core: There are two approaches for NPs preparation, top-down and bottom-up[27-29]. The top-down approach means cutting bulk materials into pieces on a nanoscale, a typical top-down approach is photolithography, which is commonly used in the semiconductor industry[30]. For instance, ASML Holding can achieve 5 nm chip preparation by extreme ultraviolet lithography (EUV). EUV is a photolithography technique using extreme ultraviolet at a certain wavelength. Other top-down approaches also include mechanical milling, nanolithography, etc. However, fine lithography instruments are very expensive, and the materials used are also of a high standard. It is also difficult to acquire smaller NPs. Additionally, NPs produced via top-down often come with surface defects.

The bottom-up approach means assembling many atoms or molecules into a nanostructure as Feynman's

hypothesis in his presentation. This approach using supramolecular interaction (Van der Waals force, electrostatic interaction, hydrophobic interaction, hydrogen bonding, and π-π interaction, etc) creates linkage of building blocks, further achieves atoms and molecules assembling at the nanoscale, or even larger. Chemical synthesis, particularly, wet chemical synthesis is the most popular bottom-up approach[31]. Atoms and small molecules in solutions are integrated into NPs driven by supramolecular interaction under specific conditions, such as pH, temperature, concentration, solvents, and reaction time. Using wet chemical synthesis, NPs can be fabricated with well-controlled, including size, shape, compositions, structure, and crystallinity. Of note, NPs prepared using this method are initially in solution, either hydrophilic solvents or hydrophobic solvents, which are more suitable for application in biological environments. Therefore, in this thesis, the focus will be given to wet chemical NPs synthesis and its effects in biological environments. Diverse applications of NPs with their intrinsic physical properties can be found in the biomedical field[32]. For instance, quantum dots (QDs) with different emission wavelengths are widely used in bioimaging *in vitro* and *in vivo*[33]. Plasmonic NPs, such as Au and Ag NPs, as the most common surface-enhanced Raman scattering (SERS) substrates, enable a great increase in the limit of detection at a single-molecule level[34]. Iron oxide NPs due to their magnetic property are used as the contrast agents of magnetic resonance imaging (MRI)[35] or tracers of magnetic particle imaging (MPI)[36]. In addition, many NPs are used to treat tumors through photothermal, magnetothermal, photodynamic therapy, or by triggering immune responses. Utilizing the enhanced permeability and retention (EPR) effect or antibody passively or actively delivers small molecules to targets[37- 38]. All cases above demonstrated the great potential of NPs from basic life science to more clinical related fields such as medicine and pharmacy.

Engineered polymer shell: NPs core synthesized by wet chemical approach always comes with the presence of surface ligands[39]. Either small molecules or macromolecule ligands ensure NPs grow in a controllable way and well disperse in the initial solution. For example, cetyltrimethylammonium bromide (CTAB) is used for controlling the anisotropic growth of Au nanorods (Au NRs)[40]. Citrate anions are reducing agents of Au ions and also stabilizers to maintain colloidal stability in Turkevinch's protocol[41]. However, in general, NPs capped with those ligands are not always ideal for exposure in biological environments[26]. For instance, the initial colloidal stability of Au NPs provided by citrate ions via electrostatic force is insufficient when exposed to phosphate buffer (PBS) or cell medium (Figure1-1). The presence of counterions in media would easily counteract the charges on the NPs surface, and NPs tend to aggregate or agglomerate. Another point is that some NPs are prepared in organic solvents, in that case, the NPs are hydrophobic. For example, iron oxide NPs[42-43] and QDs[44] are widely synthesized through decomposing organic reagents under high temperatures. NPs exposed in biological media are supposed to be hydrophilic, hydrophobic NPs would aggregate via hydrophobic interaction, thus, a phase transfer or surface modification step is usually necessary. Therefore,

despite the increasing number of benefits provided by NPs, the colloidal stability of NPs is the pride of place for further translation and application.

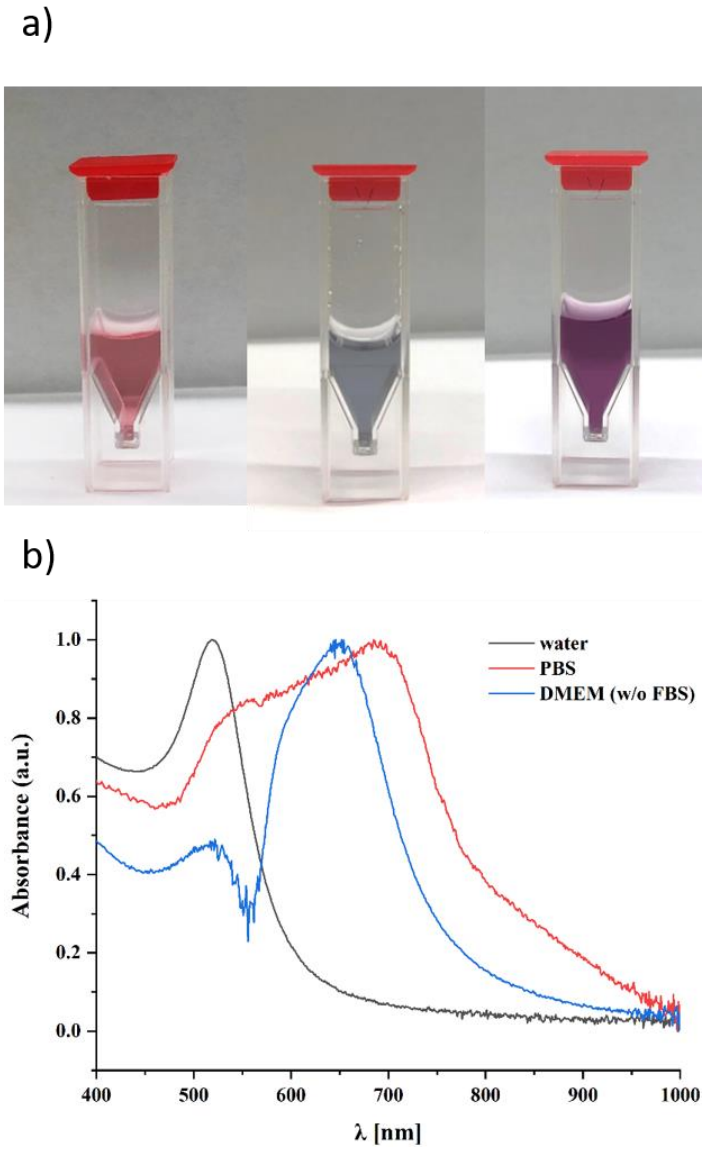

Figure1-1. *(a) Images of citrate-capped Au NPs dispersed in different media, left: Milli-Q water, middle: PBS buffer right: DMEM without FBS. (b) UV-Vis spectra of citrate-capped Au NPs dispersed in different media.*

A great option to improve colloidal stability is to use the amphiphilic polymer. Poly (isobutylene-alt-maleic anhydride)-graft-dodecyl (PMA) is an amphiphilic polymer developed by our group[45-46], which is composed of maleic anhydride as the backbone and dodecylamine (DDA) as the side chain. PMA is used to transfer NPs from being hydrophobic to hydrophilic, the alkyl chains from the organic ligands of NPs interact with DDA side chains via strong hydrophobic interaction, meanwhile, the anhydride rings were exposed outside and hydrolyzed into hydrophilic carboxyl groups. After PMA coating using a rotary evaporator, NPs could disperse in multiple aqueous solutions with excellent colloidal stability. In addition, PMA could be further modified by attaching amino groups of other molecules through an anhydride ring-opening reaction, such as fluorophores, difunctional chelates, etc. With modified PMA-coated NPs, multifunctional nanosystems can be achieved, such as bioimaging, drug delivery, and targeting[47-48]. Another common approach to improve colloidal stability is PEGylation. Poly (ethylene glycol) (PEG) is a synthetic polymer, also known as polyethylene oxide (PEO). In the biomedical field, PEG is a U.S. Food and Drug Administration (FDA) approved gold standard to prolong blood circulation of drugs and improve drug stability[49-50]. For example, both mRNA-1273 (Moderna) and BNT162b2 (Pfizer-BioNTech) vaccines incorporate PEGylating lipids to increase lipid NPs colloidal stability and reduce nonspecific protein adsorption as well as clearance of the reticuloendothelial system[51]. Besremi is another new FDA-approved PEGylated drug, which is used for the treatment of polycythemia vera[52]. By attaching PEG molecules and interferon covalently, the activity duration of interferon in the human body is greatly increased. PEGylation is also widely studied in nanotechnology, especially, PEG molecules with thiol groups have a strong binding affinity to metal atoms by forming dative bonds. Steric hindrance created by the PEG layer provides colloidal stability of NPs when electrostatic force is insufficient to keep NPs stable in biofluids[53]. In addition, PEG molecules are soluble in some organic solvents, such as chloroform ($CHCl_3$), thus, PEGylation is also a choice for phase transfer[54].

Biomolecular layer: Unlike the bulk materials, the higher surface free energy of NPs leads to adsorption of proteins, DNA, sugars, lipids, and ions on the surfaces once exposed to biological environments, forming so- called "biomolecular corona"[55], now it is mainly called "protein corona", coined by Dawson group in 2007[56]. It suggests that the formation of protein corona endows NPs with a new biological identity different from the initial physicochemical properties themselves. Afterward, an increasing number of studies prompt a deeper understanding of protein corona. For example, Lundqvist and co-workers found NPs size and surface properties play an important role in determining protein corona profile[57]. Milani et al. proposed the conception of the soft and hard corona to interpret the kinetics changes of the protein corona[58]. The hard corona on the surface of NPs is irreversible, whereas the weakly bound soft corona on the outside could dynamic exchange with proteins in the media in a competitive manner based on the Vroman effect. A comprehensive proteomics analysis of NPs exposure in human blood plasma was carried out by Tenzer and colleagues, 125 proteins

identified in plasma corona were analyzed using bioinformatics methods, indicating the complexity of plasma corona[59]. Furthermore, a great variety of evidence indicates the formation of protein corona will lead to various biological responses, including cellular uptake, reduced toxicity, complement activation, blood coagulation, autophagy, etc[60-64]. In addition, protein corona will also change the biodistribution of NPs *in vivo*[65], greatly limiting the clinical translation of nanomedicine. It was reported that only 0.7% of administered nanoparticles were able to reach the tumor targets, there was only 0.9% of efficiency even for active targeting[66]. Protein corona is one of the main reasons resulting in low delivery efficiency except for some natural biological barriers *in vivo*.

Although vast amounts of efforts have been made, a detailed understanding of protein corona is still urgently needed. To date, reducing or exploiting are two main directions for protein corona study. As mentioned above, PEG is widely regarded as a stealth polymer due to hydration of hydrophilic polyether backbone preventing protein adsorption, however, there are still some other proteins adsorbed to PEGylated NPs, such as clusterin[67]. How those proteins function towards protein corona formation is still far from clear. Zwitterionic NPs also draw plenty of attention as a novel strategy to reduce protein adsorption, like PEGylation, zwitterionic polymer reduces protein adsorption as a result of inducing a hydration layer as a steric hindrance effect to cover active binding targets[68]. Unlike reducing protein adsorption, since protein corona profiles vary as NPs physicochemical properties, scientists are trying to acquire desired protein corona via controlling some properties, such as size, shape, composition, as well as surface modification. For instance, due to the capacity in translocating across the blood-brain barrier, Wang et al designed a graphene quantum dots (GQDs) based inhibitor to treat neurodegenerative diseases by driving human islet amyloid polypeptide (IAPP) fibrillization off-pathway to eliminate toxicity, the latter is considered as the hallmark of type 2 diabetes[69]. Rodriguez and co-workers developed NPs linked with CD47 glycoprotein, CD47 is a membrane protein in mice, which can impede phagocytic clearance by signaling with phagocyte receptor[70]. In that system, integrating CD47 with NPs greatly enhanced the delivery efficiency of NPs.

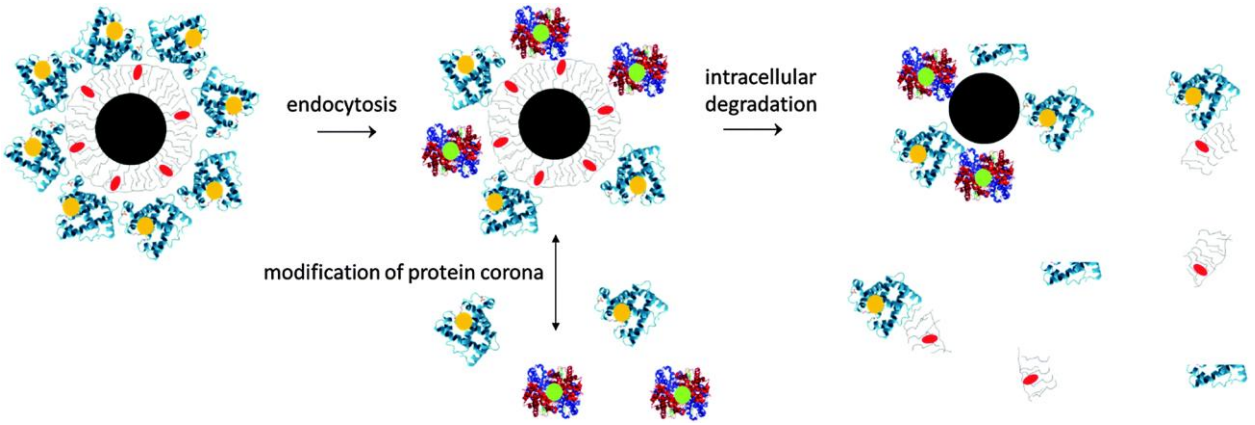

Figure 1-2. *A sketch of multi-compartmental NPs exposed to biological environments and interaction with cells upon endocytosis. (NP core: drawn in black; Engineered polymer shell: drawn in grey; Biomolecular layer: drawn in blue).*[26]

1.3 Motivation of this study

Thanks to the sustaining efforts of scientists, some new insights towards NPs have come into our classical theory in the last decades. However, most studies were performed from a qualitative view, which likely makes them difficult to compare with each other among different studies. Therefore, it is somehow reasonable that many similar studies often lead to debatable conclusions. It is challenging to make other variables at the same condition in different studies, while some of which might be crucial for those studies. Given the multi- compartmental nature of NPs in biological environments, there is a need to have a better understanding of those nano-bio interactions in a quantitative way. Herein, we quantitatively evaluated the biological effects of multi-compartmental Au NPs with different ligands from plants to animals, even more, detailed cells. We hope our study could help find something new and make a small contribution to the application of NPs in the biomedical field.

2 Quantitative evaluation of the biodistributions of gold and iodine in Matricaria chamomile with ICP- MS

2.1 Introduction

Climate change has been becoming a serious issue around the world, such as ice melting, sea-level rise, biodiversity loss, etc. leading to more and more extreme weather emerging, of which, the most significant cause is human activities, including increased fossil fuel usage, deforestation, and increasingly intensive agriculture[71-72]. As a result, a growing chorus of greenhouse gases is released into the environment, which disrupts the balance of our ecological system. Fortunately, many countries are prioritizing this issue and taking action to prevent our planet from being inhabitable. For example, Paris Agreement is the most important global response among over 170 countries to tackle climate change[73-74]. Therefore, for our future, it is urgent to stop climate change.

Plants are considered a pivotal lever that influences climate change[75]. One reason is that forests are the second biggest carbon sink after the ocean on earth. 30 % of carbon emissions are stored in forests[76]. Reducing the level of atmospheric carbon dioxide by planting more and more trees is the most potential and simple way of climate change mitigation. Another aspect is current industrial agriculture is the main cause of the generation of greenhouse gases[77]. Industrial agriculture practices such as increased use of pesticides and synthetic fertilizers are generating more and more greenhouse gases throughout manufacture, transport, and application[78]. Monocultures change biodiversity and make the ecological system unstable[79]. Deforestation and degradation are reducing the capability to store carbon[80]. Especially, the shortage of food caused by extreme weather further speeds up the vicious circle[81]. Thus, there is an urgent need to keep the balance between food supply and carbon sequestration.

Nanotechnology has been showing great potential in multiple fields including energy, food, biomedicine, environment, etc[82-85]. Equally, all these applications can play a significant role in climate change mitigation. With the property of high surface area, nanomaterials could absorb greenhouse gases directly[86]. Lightweight materials made from nanomaterials are a great alternative for vehicles[87]. Nanomaterials as catalysts enable us to improve fuel efficiency and reduce consumption[88]. Nanotechnology could enhance the battery power by orders of magnitude, which would greatly promote the popularity of new energy vehicles[89]. Without doubts, nanotechnology can also be applied to optimizing plants to indirectly mitigate climate change. One promising

strategy is to transplant the conception of drug delivery from medicine to plants. Like some small molecules drugs or biomacromolecules delivered by nanomaterials to some desired targets in our body, various nutrients, even genetic materials are also necessary to be delivered to plants to facilitate the growth of plants[90-92]. While the existence of biological barriers in plants always makes it difficult to achieve[93]. Nanoparticles are widely studied as carriers in nanomedicine, which could facilitate targeted delivery *in vivo*. Likewise, we can also deliver nutrients or genetic materials to plants with nanoparticles so that get some more sustainable plants or new species. However, the study of NPs delivery in plants is not as common as in animals[94], especially how physicochemical properties of NPs affect the delivery is still poorly understood[95-96]. For instance, is this process also as size-dependent on NPs as that in animals? Does the polymer shell around NPs also affect the biodistribution in plants? And are there also protein corona formation upon NPs exposure in plant environments? What is the relationship between the polymer shell and protein corona in plants? Altogether, there are too many questions that need to be detailed and studied.

In the present work, we prepared a library of hydrophilic Au NPs with different sizes and different polymer shells. Matricaria chamomile was chosen as the plant model. Upon exposure to different Au NPs, as well as gold salts, gold (III) chloride trihydrate, and iodine (potassium iodide and iohexol), we quantitatively evaluated the biodistribution of gold and iodine in chamomile at different incubation times. Furthermore, we introduced ICP-MS as a quantitative evaluation technique in NPs quantitative analysis, which provides a good reference for multi-compartmental NPs quantification in more complex environments.

2.2 Experiments and methods

2.2.1 Preparation of Au NPs, gold salts, and iodine

The library of Au NPs was prepared by my colleague, Yang Liu. According to different protocols, we obtained different sizes of Au NPs stabilizing with different polymer shells. Of which, 6-aza-2-thiothymine-capped Au NPs, acetylcysteine-capped Au NPs, BSA-capped Au NPs, and PMA-capped Au NPs were denoted as ATT@Au NPs, ACC@Au NPs, BSA@Au NPs, and PMA@Au NPs, respectively. PMA@Au NPs with different sizes were synthesized with the seed growth method in an aqueous solution and post-overcoated with PMA polymer. Gold (III) chloride trihydrate ($HAuCl_4 \bullet 3H_2O$, #16961-25-4), potassium iodide (KI, 99.99%, #204102), and iohexol (#74147) were directly purchased from Sigma-Aldrich.

2.2.2 Chamomile incubation with gold and iodine

Chamomile was bought from a flower shop in Hamburg. The physical samples were shown in Figure 2-1.

Chamomile with similar sizes was chosen and cut into a single flower with a ca. 4 cm length stem. 1mL of Au NPs with the concentration of 100 μg/mL was added to a 2-mL Eppendorf tube, respectively. Three as- cut flowers were placed in one tube and incubated for 6 h, 12 h, 24 h, and 48 h. As shown in Figure 2-2, make sure the end of the tail was immersed in the solution. To have a better reference, KI or iohexol with 100 μg/mL of iodine concentration were also added to the solution.

Figure 2-1. *Photos of chamomile (Photos taken by Yang Liu).*

Figure 2-2. *Picture for gold ($HAuCl_4$ and Au NPs) and iodine (KI and iohexol) solution incubated with chamomile (Photo taken by Yang Liu).*

2.2.3 ICP-MS measurement

ICP-MS is a technique that mass spectrometer tandemmed with inductively coupled plasma. Inductively coupled plasma is the high temperature (>7,000 K) ions source of samples which ionized by inductively heating argon gas with an electromagnetic coil. Of which, the single positive charged ions were extracted into the mass spectrometer, according to the difference in mass-to-charge (m/z) ratio, different elements or isotopes can be separated. Finally, the ions signals were recorded by a detector, and the concentration of different elements or isotopes was acquired. ICP-MS is a highly sensitive technique with a very low limit of detection (ppb to ppt level) and multiplex property. It is widely used in trace element quantification.

2.2.3.1 ICP-MS samples preparation

After incubation, the flowers were cut into six parts (the length of each stem was ca. 1 cm) as shown in Figure 2-3A and weighed for each part. Then, each part of the flower was placed into a glass tube and burned under a heating gun until carbonization. Next, 200 μL of aqua regia was added into the tube to digest each part for 48 h. The samples were diluted by 1.8 mL of 2% concentrated hydrochloric acid (HCl, % v/v, 34-37 %, Fisher chemical, #4121030), and the black insoluble substances were filtered with a syringe filter (pore size: 0.22 μm). The filtrate was transferred into a 5 mL PFA tube for ICP-MS measurement.

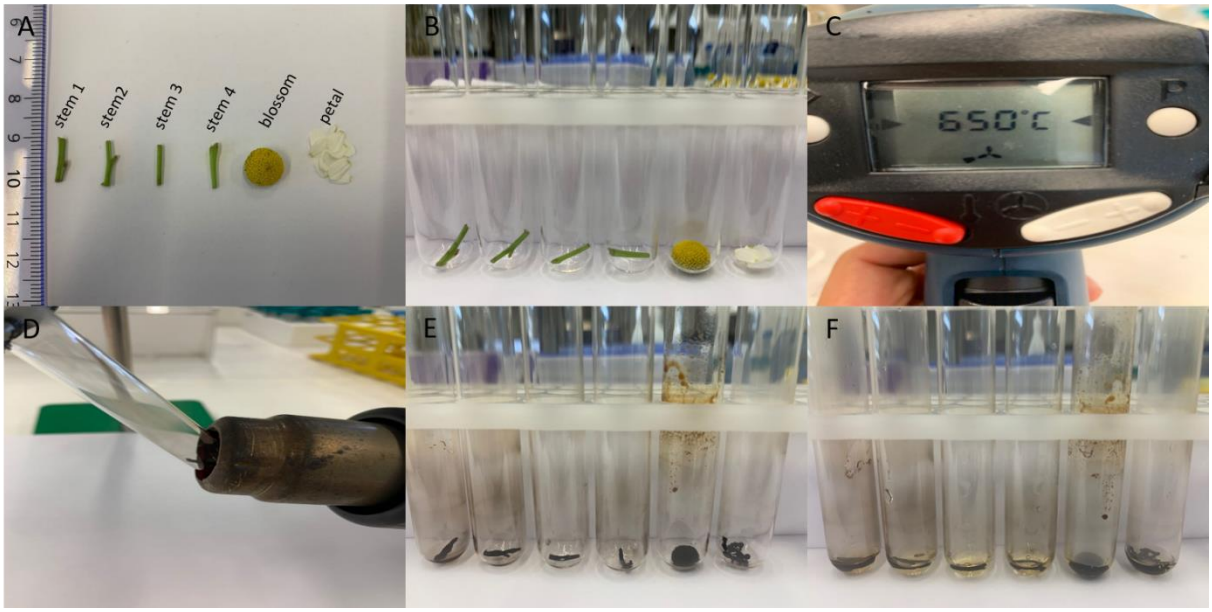

Figure 2-3. *(A) Each flower is divided into 6 parts. (B) The flower parts are put in separate glass tubes. (C, D) A heating gun is used for burning the flower parts at 650 ℃. (E) Picture of the different flower parts after burning. (F) The burned flower parts are digested in 200 µL aqua regia for 48 h. (Photos taken by Yang Liu)*

2.2.3.2 ICP-MS measurement and data evaluation

All samples were measured with an Agilent 7700 series ICP-MS. Each group of samples was at least triplicate. For each flower that was incubated with Au NPs or KI/iohexol the following values were recorded at the respective incubation time points in an Excel file: Mass of all 6 flower parts (stem 1, stem 2, stem 3, stem 4, blossom, petals), *i.e.* m_{flower}(stem 1), m_{flower}(stem 2), m_{flower}(stem 3), m_{flower}(stem 4), m_{flower}(blossom), m_{flower}(petals), and the mass of Au and/or I found in the respective flower part, *i.e.* m_{Au}(stem 1), m_{Au}(stem 2), m_{Au}(stem 3), m_{Au}(stem 4), m_{Au}(blossom), m_{Au}(petals), m_{I}(stem 1), m_{I}(stem 2), m_{I}(stem 3), m_{I}(stem 4), m_{I}(blossom), m_{I}(petals). Note, that the drastic outliers were removed from the statistics.

2.3 Results and discussions

2.3.1 Characterization of the library of Au NPs

The transmission electron microscopy (TEM) images of the library of Au NPs were shown in Figure 2-4. The diameters of the Au NPs range from 1 nm to 100 nm. The size distributions of different Au NPs in TEM images were acquired by counting 100 of NPs with Image-J software. The histograms were shown in Figure 2-5. Other characterizations including ultraviolet-visible (UV-Vis) absorption spectra, dynamic light scattering (DLS), and zeta potential were also performed (not shown here), please refer to Yang's thesis or our publication for the detailed results.

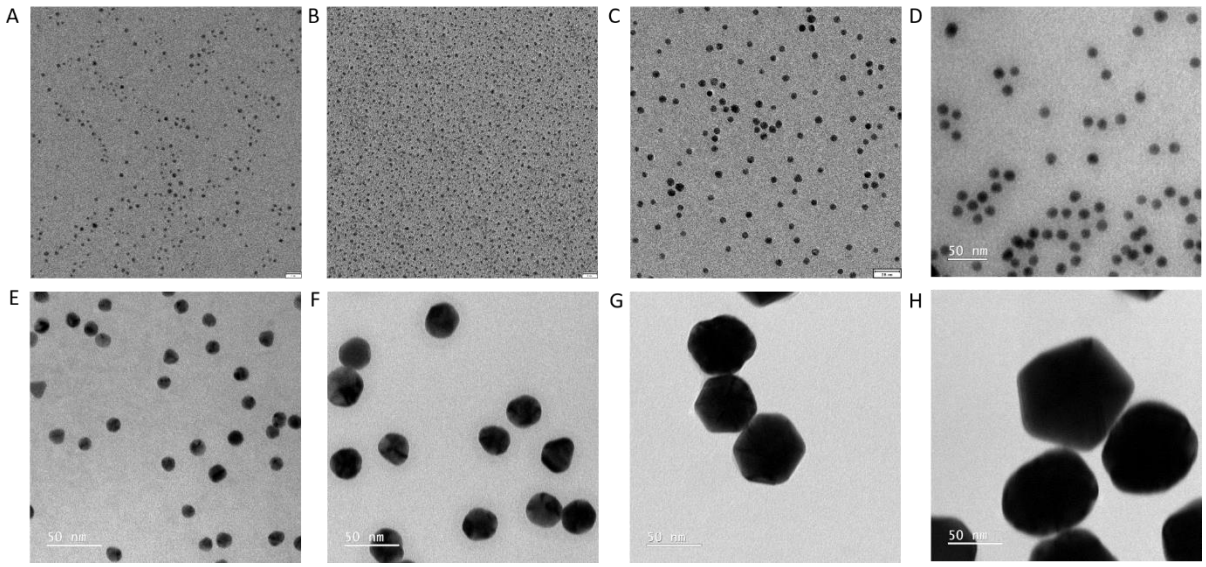

Figure 2-4. *TEM images of the library of Au NPs. (A) ATT@Au NPs (scale bar: 9 nm), (B) ACC@Au NPs (scale bar:7 nm), (C) PMA@Au NPs (5nm core, scale bar: 20 nm), (D) BSA@Au NPs (scale bar: 50 nm), (E) PMA@Au NPs (14 nm core, scale bar: 50 nm), (F) PMA@Au NPs (31 nm core, scale bar: 50 nm), (G)PMA@Au NPs (54 nm core, scale bar:50 nm), (H) PMA@Au NPs (94 nm core, scale bar: 50 nm) (Images taken by Marta Gallego).*

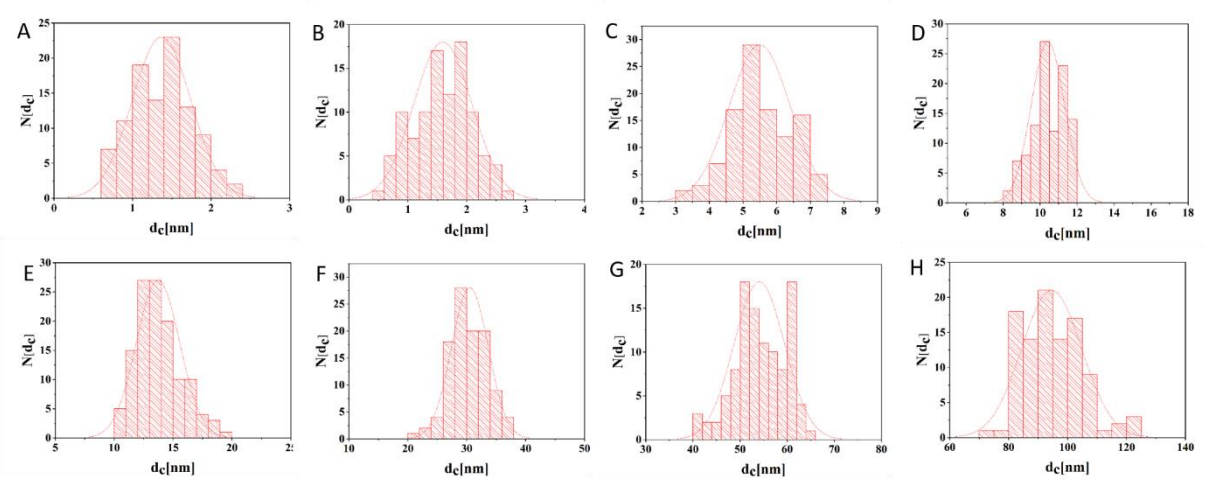

Figure 2-5. *Histograms of the library of Au NPs core size distribution. (A) ATT@Au NPs (1.37±0.37 nm), (B) ACC@Au NPs (1.56±0.52 nm), (C) PMA@Au NPs (5nm core, 5.49±0.91 nm), (D) BSA@Au NPs (10.42±0.90 nm), (E) PMA@Au NPs (14 nm core, 13.72±1.83 nm), (F) PMA@Au NPs (31nm core, 30.52±3.12 nm), (G)PMA@Au NPs (54 nm core, 53.90±5.33 nm), (H) PMA@Au NPs (94 nm core, 94.48±10.20 nm) (Histograms plotted by Yang Liu).*

2.3.2 Quantitative evaluation of the biodistributions of gold and iodine in chamomile

2.3.2.1 Different biodistributions of gold and iodine

As shown in Figure 2-6 and Figure 2-7, the biodistribution of iodine and gold is significantly different. In the case of iodine (both KI and iohexol), the petals absorbed the most iodine after 48 h incubation. While compared to the iohexol group, at 24 h incubation more KI was accumulated in the stem rather than in petals, indicating the iodine absorption of the KI group was slower than the iohexol group. In contrast, regardless of the sizes of NPs, gold (both $HAuCl_4 \cdot 3H_2O$ and Au NPs groups) was mainly accumulated in stem 1 except ACC@Au NPs group, suggesting the difficult transportation of gold. For ACC@Au NPs, there is a similar biodistribution as iodine. We speculated that the different biodistributions are likely due to there might be some ionic channels or transporters existing on the cells of petals for iodine and ACC@Au NPs uptake. Although there are no relevant iodine-specific ionic channels or transporters reported yet, some analogs such as chloride transporters might be able to do this job. For ACC@Au NPs, the surface ligands are acetylcysteine. There are various natural amino acid transporters in plant cells, therefore, the absorption of ACC@Au NPs was much easier than other Au NPs or Au ions.

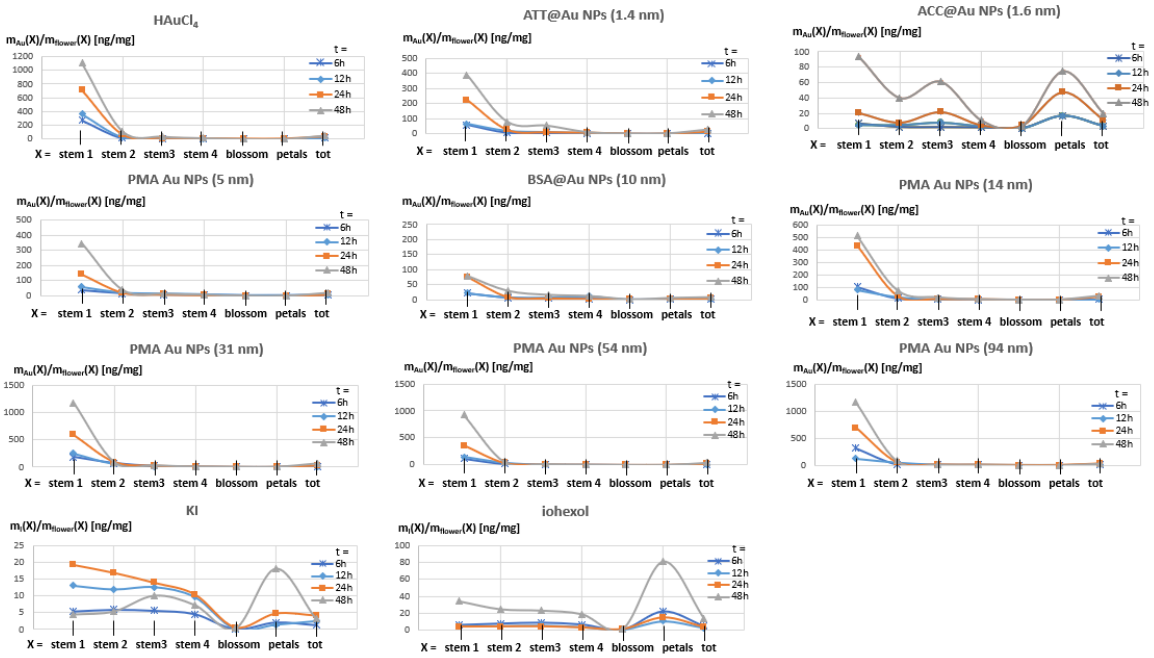

Figure 2-6. *The amount of gold or iodine found in the respective flower parts, normalized to the mass of the flower parts, plotted versus the position of the flower parts along the stem.*

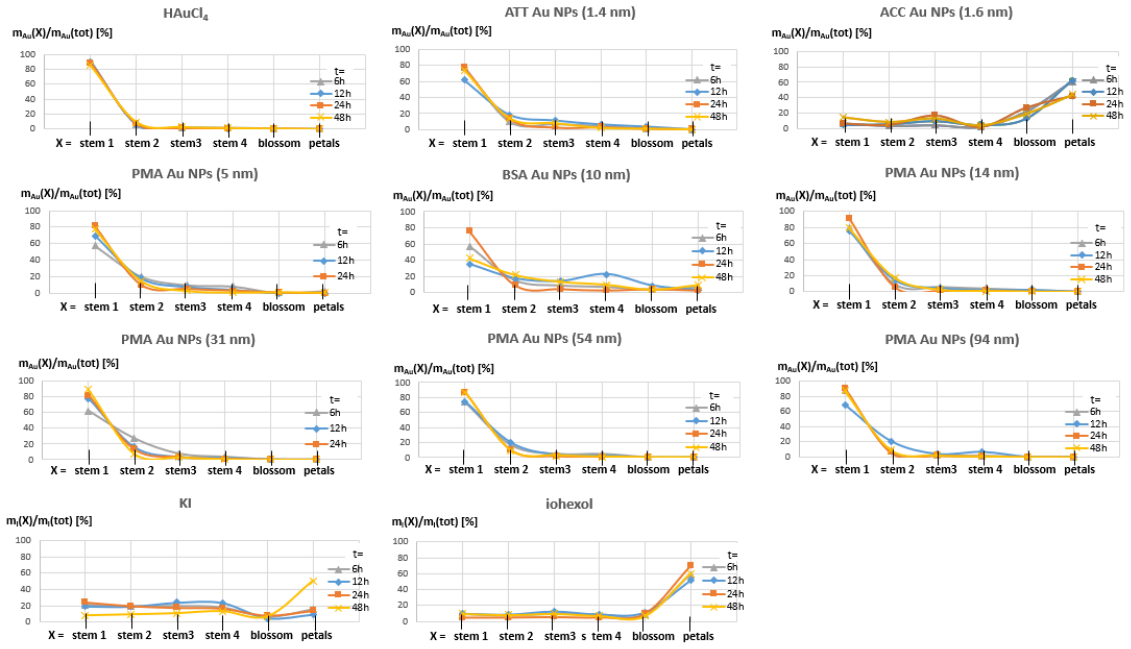

Figure 2-7. *The amount of gold or iodine found in the respective flower parts, normalized to the total mass of gold or iodine found in the whole flower, plotted versus the position of the flower parts along the stem.*

2.3.2.2 Time-dependent transportation of iodine and gold

In Figure 2-8 and Figure 2-9, it is obvious that the accumulation of gold and iodine was time-dependent. After 48 h incubation, the maximum uptake of gold was ca. 1200 ng per 1 mg of flowers, and the maximum of iodine was ca. 80 ng per 1 mg of flowers. The different accumulation amounts of gold and iodine might result from the special internal structure in the stem. The vascular tissues of plants are responsible for the transportation of substances. There are two types of vascular tissues, called xylem and phloem. Xylem transports water and minerals via transpiration while phloem transports nutrients via diffusions, such as sugars or amino acids. Both the processes are driven by physical forces. Therefore, all of the uptaken elements would increase with the increase of incubation time. In addition, phloem is composed of live cells, in which sieve plates play important roles in nutritional choice and preventing animal intrusion. Therefore, we suspect that those Au NPs apart from ACC@Au NPs would be considered exogenous substances so they are not able to be transported via the phloem. The xylem consists of elongated dead cells without cytoplasm, and there are no sieve plates in the xylem. In this case, the xylem pathway is a better choice for NPs transportation. However, given the vascular structure of chamomile was not our focus in this study, more detailed structural information should be involved in the future. In addition, the percentage of iohexol in petals was much higher than in other parts of the flower even at 6 h incubation, whereas the same phenomenon was observed in the KI group until 48 h incubation (Figure 2-9 left), suggesting the slower transportation of KI, which has a good agreement with that mentioned above.

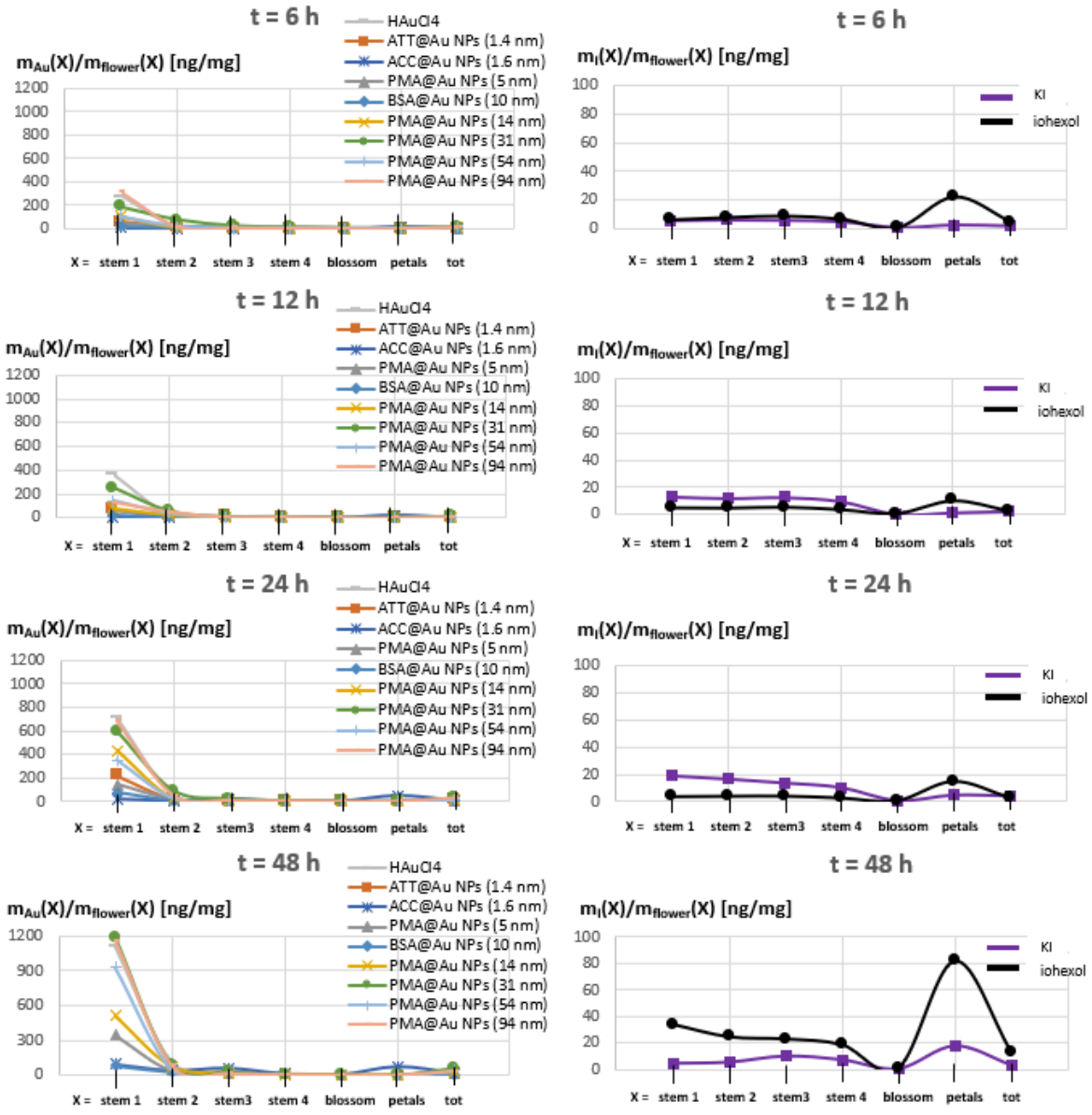

Figure 2-8. *The amount of gold or iodine found in the respective flower parts, normalized to the mass of the flower parts, plotted versus the position of the flower parts along the stem.*

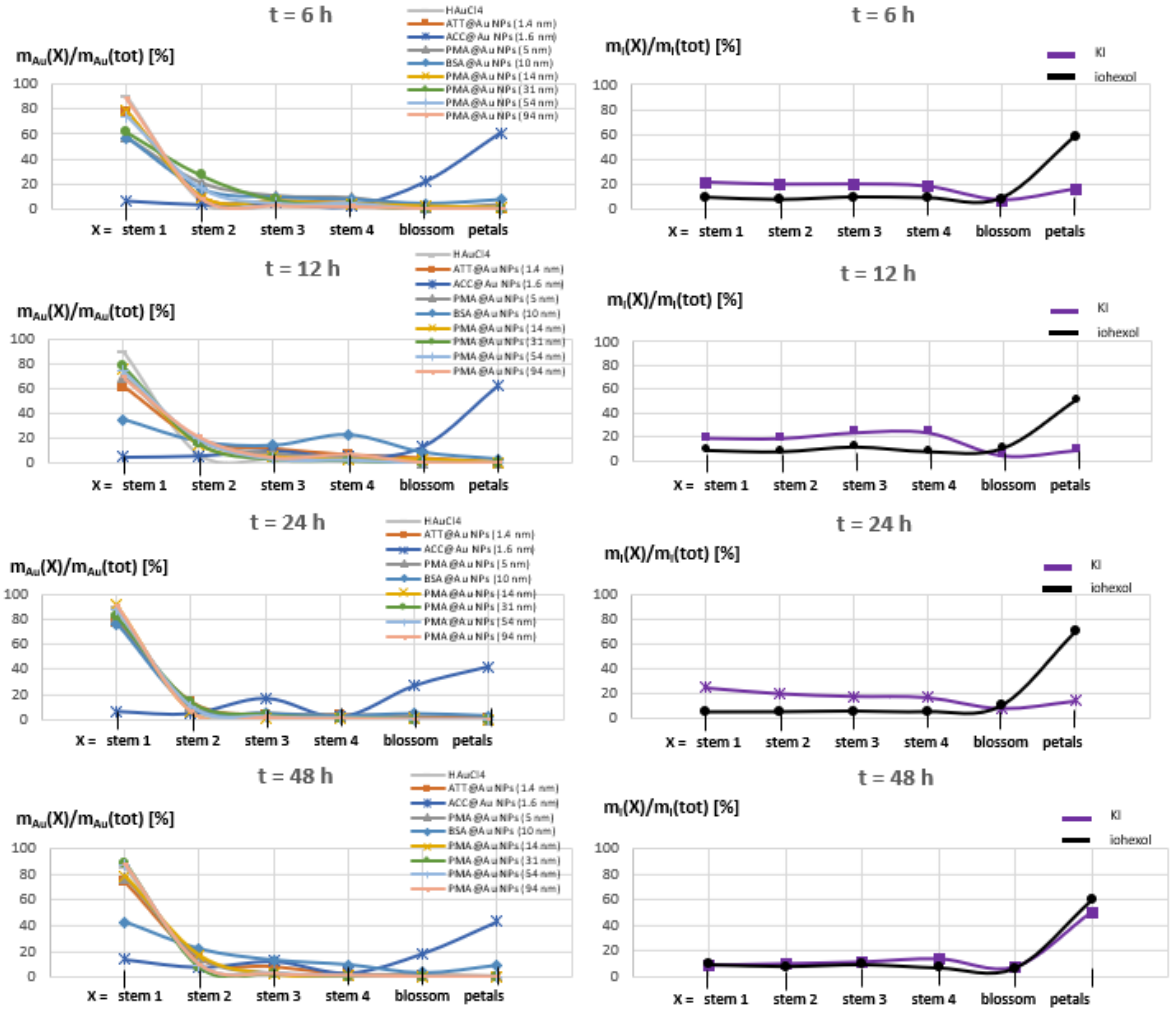

Figure 2-9. *The amount of gold or iodine found in the respective flower parts, normalized to the total mass of gold or iodine found in the whole flower, plotted versus the position of the flower parts along the stem.*

2.3.2.3 Size-dependent transportation of Au NPs

Although the sizes of ACC@Au NPs (1.6 nm) and ATT@Au NPs (1.4 nm) are similar, the different biodistributions demonstrated that the surface chemistry is crucial to Au NPs transportation in plants. To prove the impacts of sizes of Au NPs on transportation in chamomile, we also compared the biodistributions of different sizes of Au NPs with the same surface coating, PMA (Figure 2-10). The accumulation of PMA@Au NPs in chamomile increased as the size increased until achieving the maximum absorption at 31 nm. Then, the accumulation of gold decreased. However, the strong size dependence of PMA@Au NPs uptake remains unknown. Note that PMA@Au NPs were all stuck in the part of stem 1.

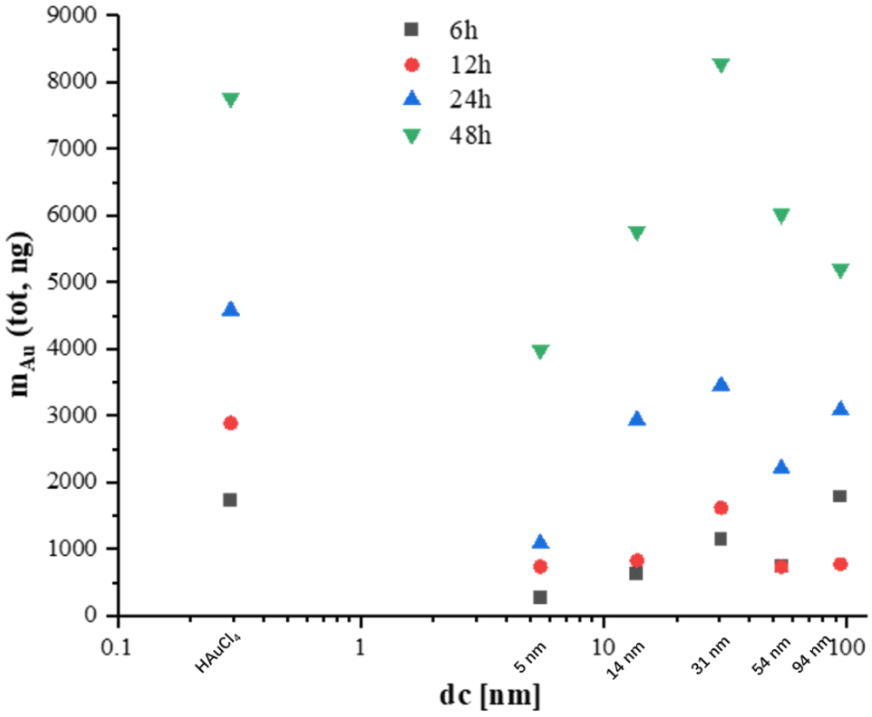

***Figure 2-10**. The total amount of gold found in one whole flower plotted versus the core diameter of the different PMA@ Au NPs*

2.4 Conclusion

In this study, we incubated chamomile with different gold and iodine solutions at different times and studied the biodistributions of gold and iodine in plants. We found that the biodistributions of iodine were quite different compared to most gold salts/NPs. ACC@Au NPs were the only ones with a similar biodistribution to iodine. The surface ligands of ACC@Au NPs were acetylcysteine, which is one form of amino acid. We guess that ACC@Au NPs were considered nutrients by plants, and resulted in the different accumulations compared to other AuNPs. It indicates that surface ligands play a significant role in NPs transportation. In addition, the transportation of NPs shows a strong size-dependent property. For all the PMA@Au NPs with different sizes, PMA@Au NPs (31nm) can deliver the most gold to plants, however, almost all the Au NPs were stuck in the stem 1. All the gold and iodine solutions uptaken were time-dependent, which suggested a passive transportation process in our study. Moreover, we used ICP- MS, a high sensitive multiplex elements analysis technique, to quantify the amounts of Au NPs accumulated in plants, which paves the way for multi- labeled NPs quantification in more complex biological environments.

3 Quantitative evaluation of protein adsorption on NPs and its effects on cellular uptake

3.1 Introduction

The increasing number of studies of nanotechnology has greatly prompted the applications of nanomaterials in biomedical fields. Of which, drug delivery gains much more attention from pharmaceutical companies, biotechnology companies, and scientists with different backgrounds[18, 97-99]. Especially, as the concept of "precision medicine" was proposed, the demands for more intelligent nanodrugs are increasing[100]. Despite the great popularity of nanomedicine, there are still too few nanodrugs approved by the U.S. FDA or the European medicines agency (EMA) compared to plentiful drugs in the preclinical and clinical study[101-102].

One of the causes is the complexity of biological environments. Once upon exposure to biological fluids like blood, urine, and saliva, NPs will inevitably adsorb various biomolecules forming so-called "protein corona"[56]. This layer of protein corona confers NPs a new and mysterious "biological identity", which changes the physicochemical properties of pristine NPs and makes them uncontrollable as an intelligent theradiagnostic platform. For instance, protein corona could affect the efficiency of cellular uptake. Yan et al. reported the different impacts of protein corona on cellular uptake among different immune cells[103]. In the case of human monocytic cells (THP-1), the formation of protein corona could decrease the internalization efficiency of nanoporous polymer particles, whereas, for differentiated macrophage-like cells (dTHP-1), there were no significant changes. In another study, Schöttler and co-workers found the abundance of apolipoprotein J could inhibit the cellular uptake of polystyrene NPs in macrophages[67]. Besides, the presence of complement protein, immunoglobulins, and fibrinogen was also reported that related to cellular internalization[104-106]. Protein corona can also decrease the targeting efficiency of nanodrugs and subsequently change the biodistribution in vivo[107- 109]. One biggest advantage of nanodrugs is the targeting capability by the EPR effect or conjugated with antibodies. However, in a meta-analysis of the Chan group, only 0.7% of administered NPs were delivered to solid tumors as desired[66]. Except for the intrinsic physiological barriers in the body, the formed protein corona can cover the conjugated antibodies or change the physicochemical properties of NPs so that not suitable for the EPR effect anymore. As a result, the targeting capability was inhibited and the NPs were restricted in other organs, even causing toxicity. Moreover, the composition of protein corona varies among NPs with different sizes, shapes, hydrophilicity, surface chemistry, chirality, etc[110-119]. Even for the same NPs, protein corona could also alter dynamically[120-121]. All mentioned above make protein corona difficult to clarify but essential for nanodrugs translation.

In this study, we prepared two types of NPs with different surface chemistry, and systematically studied the association between protein corona and cellular uptake. Based on the multi-compartmental nature of NPs, we labeled each compartment with a specific element, and quantitatively evaluated the cellular uptake efficiencies from different compartments via ICP-MS. We found that for those NPs with different surface chemistry, the amounts of internalized core and protein corona layer are not always consistent. To figure it out, we further studied the protein adsorption processes of two types of NPs in situ by fluorescence correlation spectroscopy (FCS) and finally related it to cellular internalization.

3.2 Experiments and methods

3.2.1 Synthesis of 17 nm Au NPs

The 17 nm citrate-capped Au NPs were prepared via reducing $HAuCl_4 \bullet 3H_2O$ by sodium citrate dihydrate according to a modified Bastus' method[122]. Briefly, 0.2 mmol sodium citrate dihydrate (Alfa Aesar, #6132- 04-3) dissolved in 150 mL Milli-Q water was placed in a 250 mL three-neck round-bottomed flask connected with a condenser and heated up with a heating mantle until boiling. After ca. 5 min, 0.025 mmol of $HAuCl_4 \bullet 3H_2O$ dissolved in 1.5 mL Milli-Q water was quickly injected under vigorous stirring for another 10 min. During this time, the mixture's color change was observed from pale yellow to light blue and then to wine red, indicating the growth of Au NPs. Then, the Au NPs solution was cooled down to room temperature under stirring. The products were purified by centrifugation at 9,000 rpm for 30 min, the supernatant was discarded and the precipitate was redispersed in Milli-Q water. Purification was carried out twice and the precipitate was collected for further characterization and modification.

3.2.2 Au NPs shell labeling

In this study, amphiphilic polymer PMA and poly (ethylene glycol, PEG) were used as two different surface chemistry strategies. Gadolinium (Gd) labels were conjugated to two polymers using different difunctional chelates 1,4,7,10-tetraazacyclododecane-1,4,7,10-tetraacetic acid (DOTA) derivatives, respectively. DOTA is a macrocyclic chelator with thermodynamic stability and kinetic inertness which has been widely investigated in a range of biomedical applications, including MRI (Gd^{3+}), positron emission tomography (PET, $^{68}Ga^{3+}$, $^{86}Y^{3+}$, $^{64}Cu^{2+}$) imaging, and single-photon emission computed tomography (SPECT, $^{111}In^{3+}$) imaging[123]. Attaching labeled DOTA complexes to the Au NPs polymer shell enables us to detect the time-dependent changes of two shells in biological environments, like the degradation of the polymer shell of Au NPs upon cellular endocytosis. It is worth noting that to perform a quantitative evaluation of cellular uptake experiment, non-specific adsorption of Gd tags is supposed to be avoided. In our previous study, DOTA complexes were

often used as a post-labeling strategy i.e., metal ions were chelated after polymer modified with DOTA[124]. However, there is also electrostatic force between metal ions and the functional groups (- COO^- , -PO_3^{2-}, etc.) of the polymer itself, which is always a challenge for a quantitative study. Therefore, in the present study, we choose a pre-labeling approach.

3.2.2.1 PMA Au NPs labeling

PMA was an amphiphilic polymer developed by our group, which could be further modified by attaching other molecules with amino groups, including fluorophores, difunctional chelates, etc., of which DDA, provided the hydrophobic side chains and maleic anhydride rings from the backbone of PMA hydrolyzed forming hydrophilic carboxyl groups. The schematic illustration was shown in Figure 3-1.

a)

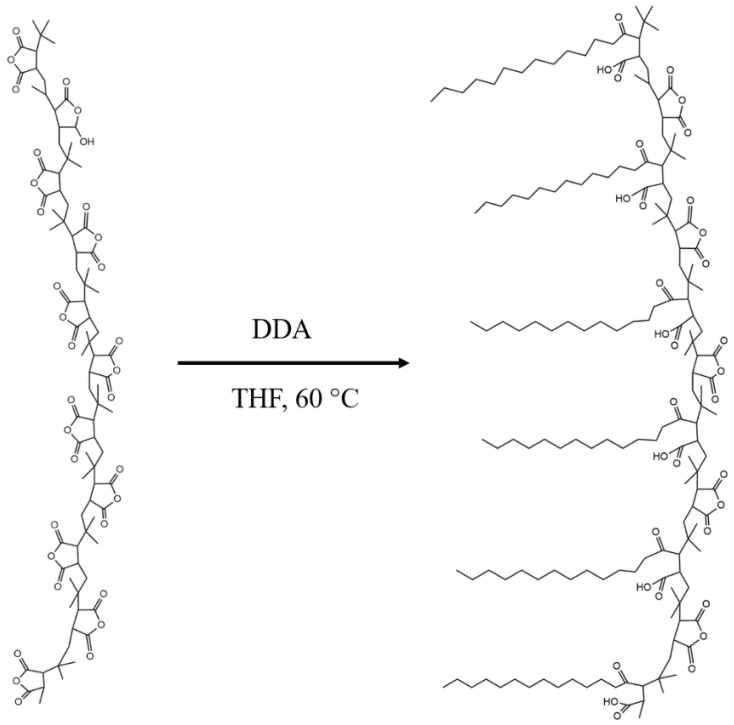

poly (isobutylene-alt-maleic anhydride) normal PMA

b)

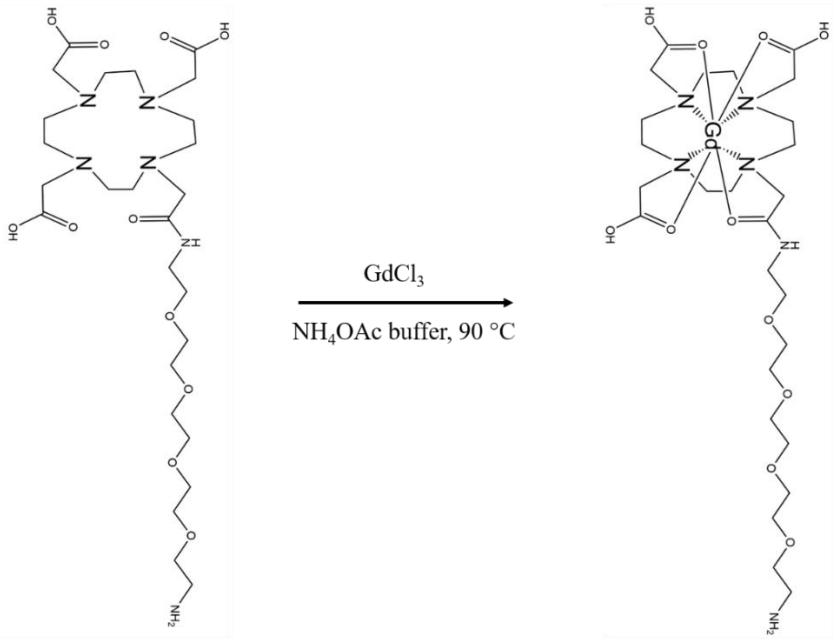

DOTA-PEG_4-NH_2 Gd-DOTA-PEG_4-NH_2

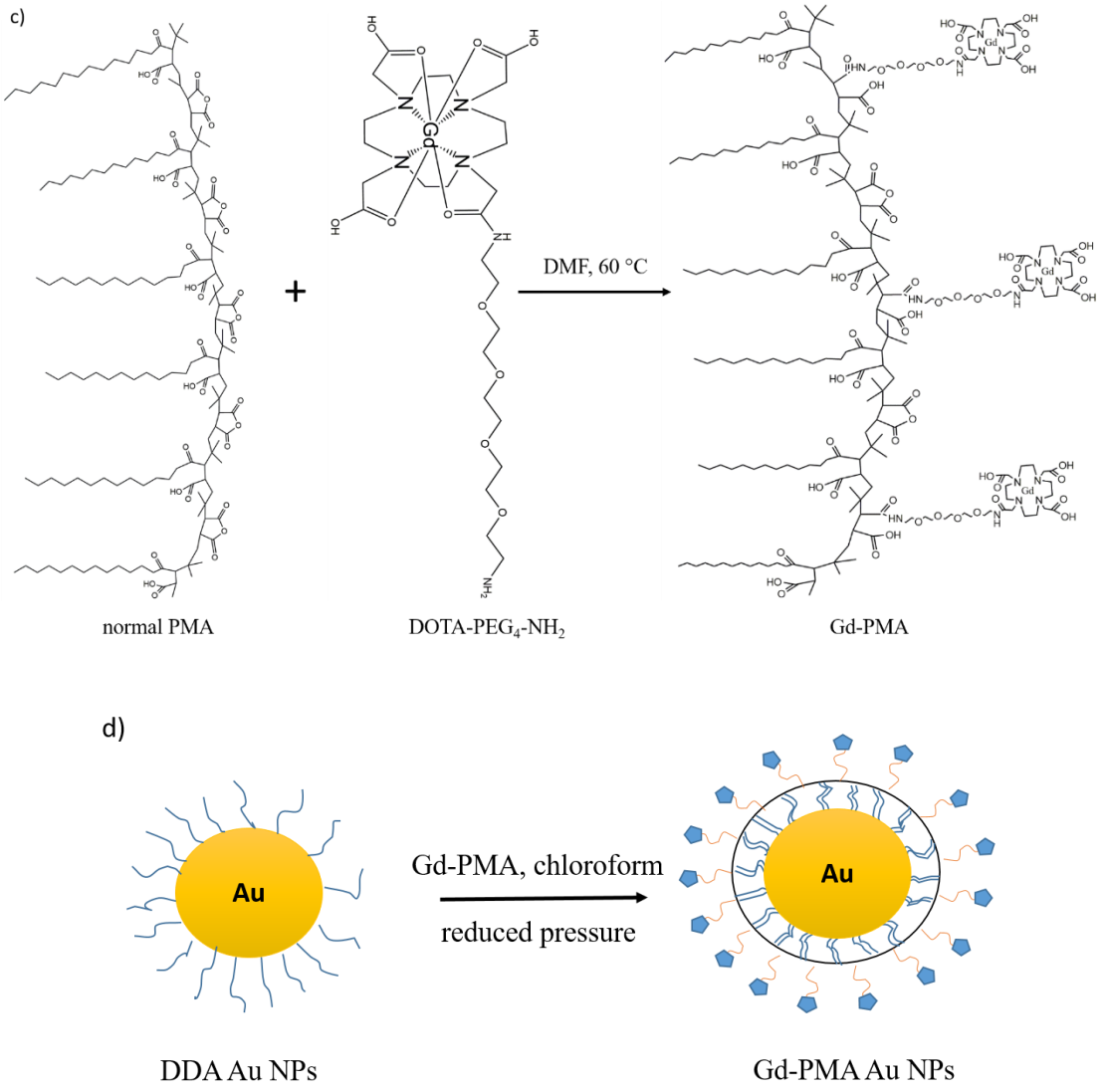

Figure 3-1. *Scheme of Gd labeled PMA Au NPs (Gd-PMA Au NPs) preparation. (a) Synthesis of normal PMA. (b) Preparation of Gd-DOTA-PEG₄-NH₂ complexes. (c) Synthesis of Gd labeled PMA (Gd-PMA). (d) Polymer coating.*

1) Preparation of Gd labeled PMA

1.1) Preparation of Gd labeled DOTA chelator (Gd-DOTA-PEG_4-NH_2)

DOTA chelator labeling with Gd was done by Malte Holzpfel from Wolfgang Maison group. 68.1 mg of DOTA-PEG_4-NH_2 (109 μmol, 1.00 eq) (#C125, CheMatech) and 43.9 mg of gadolinium (III) oxide (121 μmol,1.11 eq) (Gd_2O_3, Sigma, #12064- 62-9) were dissolved in 3.50 mL of ammonium acetate (NH_4OAc) buffer (pH 5.5) and stirred for 3 h at 90 °C. Then, the solution was freeze-dried and purified by reversed-phase column chromatography (C18, H_2O/CH_3CN with 0.1% HCO_2H, 99:1→0:1). The product Gd- DOTA-PEG_4-NH_2 yielded as a white solid (64.5 mg, 83.0 μmol, 76%).

1.2) Synthesis of normal PMA

The normal PMA was prepared as reported in the previous study[46]. 3.084 g of poly (isobutylene-alt-maleic anhydride) (average Mw~ 6,000g/mol, 39 monomer units for each polymer, Sigma, #531278) was placed in a 150 mL round-bottom flask. Then, 100 mL of tetrahydrofuran (THF, Aldrich #186562) was injected, followed by adding 2.70 g of DDA (98%, Fluka, # 44170). The mixture was vigorously stirred at 60 °C overnight and slowly evaporated by a rotary evaporator (Heidolph, Germany) until a thin PMA film formed around the flask bottom. 40 mL of anhydrous $CHCl_3$ (VWR, #22707.320) was added to redissolve the PMA film under sonication. Finally, the amphiphilic polymer was yielded with a 0.5 M of monomer concentration.

1.3) Synthesis of Gd labeled PMA (Gd-PMA)

In a 25 mL round-bottom flask, 2.329 mL of normal PMA (0.5 M) and 27.2 mg of Gd- DOTA- PEG_4-NH_2 were dissolved in 20 mL of dimethylformamide (DMF, Sigma-Aldrich, #227056) under stirring at 60 °C for 6 h. Afterward, the mixture was completely evaporated under reduced pressure and redissolved in 23.29 mL of $CHCl_3$. The final Gd labeled PMA was acquired with 0.05 M of monomer concentration.

2) Polymer coating

Before polymer coating, we conducted a phase transfer procedure to make citrate-capped Au NPs from being hydrophilic to hydrophobic. Excess α-Methoxy-ω-mercapto PEG (CH_3O-PEG-SH, 2k Da, Rapp Polymere, #122000-40, c_{PEG}/c_{NPs}=30,000) was dissolved in as-prepared citrate capped Au NPs under stirring for 2 h. The PEGylation was performed by forming dative bonds due to Au atoms from the Au NPs surface coordinating with sulfur atoms of PEG molecules. Then the PEGylated Au NPs were washed twice by centrifugation at 9,000 rpm for 30 min to remove excess CH_3O-PEG-SH molecules. Next, in a 150 mL round-bottom flask, the precipitate of PEGylated Au NPs was resuspended in 40 mL of Milli-Q water under vigorously stirring,

followed by adding 40 mL of $CHCl_3$ and a certain amount of DDA (c_{DDA}/c_{NPs}=10,000,000) until PEGylated Au NPs in H_2O phase transferred to $CHCl_3$ phase, indicating hydrophobic DDA-capped Au NPs yielded. The DDA-capped Au NPs in $CHCl_3$ were centrifuged three times (9,000 rpm, 30 min) to remove excess DDA molecules. For each centrifugation, the precipitate was collected. Then, all the collected Au NPs dispersed in fresh $CHCl_3$ and the concentration was determined by a UV-Vis spectrum.

Polymer coating was performed by hydrophobic interaction of DDA alkane chain from Au NPs and PMA under reduced pressure evaporation. The amount of PMA monomer units used was calculated based on the total surface area of NPs. In this study, we adopted $R_{P/Area}$=2000 units/nm^2, which referred to as 2000 monomer units were added per nm^2 of effective NPs surface area. The effective NPs surface area was calculated according to the number of NPs times the surface area of one single NP. The formulas were shown below.

$N = C^* V^* N_A$

$A_0 = 4\pi^* (d_{eff} / 2)^2$

$d_{eff} = d_{core} + 2\ l_{ligand}$

$A = N^* A_0$

N: Number of Au NPs in the solution

C: Molar concentration of the Au NPs solution (mol/l)

V: Volume of the Au NPs solution (l)

N_A: Avogadro constant

A_0: Surface area of a single Au NPs (nm^2)

d_{eff}: Effective diameter of one Au NP

d_{core}: The average diameter of Au core

l_{ligand}: The thickness of the surfactant shell, which was assumed 1nm (nm)

A: The total surface area of all the Au NPs

In general, DDA-capped Au NPs and Gd-PMA were mixed in 50 mL of $CHCl_3$ in a 150 mL round-bottom flask. The mixture was slowly evaporated three times until all solvent was completely gone under a reduced pressure evaporator. 5 mL of borate buffered saline (BBS, 50 mM, pH 10) was added with several seconds of sonication. When Gd-PMA coated Au NPs redispersed in the aqueous solution, a washing step with Milli-Q water was carried out by centrifugation (9,000 rpm, 30 min, 4 times) to remove excess Gd-PMA, and the precipitate was purified Gd-PMA Au NPs.

3.2.2.2 PEG AuNPs labeling

PEG is intensively used to extend the circulation time of drugs or provide colloidal stability of NPs as stealth

polymer via steric repulsion. By conjugating with another DOTA chelator, PEGylated NPs can also be labeled with radioactive and nonradioactive heavy metal elements, including Gd, indium, etc.

1) Ligand exchange

75 mL of 20 nM citrate-capped Au NPs and 135 mg of HS-C_2H_4-CONH-PEG-O-C_3H_6-COOH (3k Da, Rapp Polymere, #133000-4-32, c_{PEG}/c_{NPs} =30, 000) were placed in a 100 mL flask under magnetic stirring at room temperature overnight. Afterward, the mixture was washed twice by centrifugation (30 min at 9,000 rpm), yielding PEGylated Au NPs with carboxyl groups.

2) Gd labeling of PEGylated Au NPs

Gd labeled PEGylated Au NPs were prepared by EDC coupling, where a difunctional chelator p- NH_2- Bn- DOTA (Macrocyclics, #B-200) with Gd tag conjugated with carboxyl groups of PEGylated Au NPs. In general, 20 mg of p-NH_2-Bn-DOTA was mixed with 22.9 mg of gadolinium (III) chloride hexahydrate ($GdCl_3 \cdot 6H_2O$, Sigma-Aldrich, #G7532) in 3.8 mL of 4- Morpholineethanesulfonic acid (MES hydrate, Sigma-Aldrich, #M8250-100G) buffer (50 mM, pH 6) in a 15 mL glass vial. The mixture was stirred at 90 °C for 1 h, yielding Gd labeled p-NH_2-Bn-DOTA chelator. Then, 146 μL of PEGylated Au NPs (522 nM) was added to another vial, followed by adding 77.4 mg of N-(3-Dimethylaminopropyl)-N′-ethyl carbodiimide hydrochloride (EDC, Sigma, #161462) with stirring at room temperature for 20 min to activate the carboxyl groups of PEGylated Au NPs. Thereafter, the activated Au NPs were concentrated by an Amicon Ultra-15 centrifugal filter unit (MWCO:100k Da, 15 mL, Sigma- Aldrich) to remove the by-product and excess EDC. Next, 238 μL of Gd labeled p- NH_2-Bn-DOTA chelator prepared above was mixed with the activated PEGylated NPs under stirring overnight. The products were purified four times by centrifugation at 9,000 rpm for 30 min.

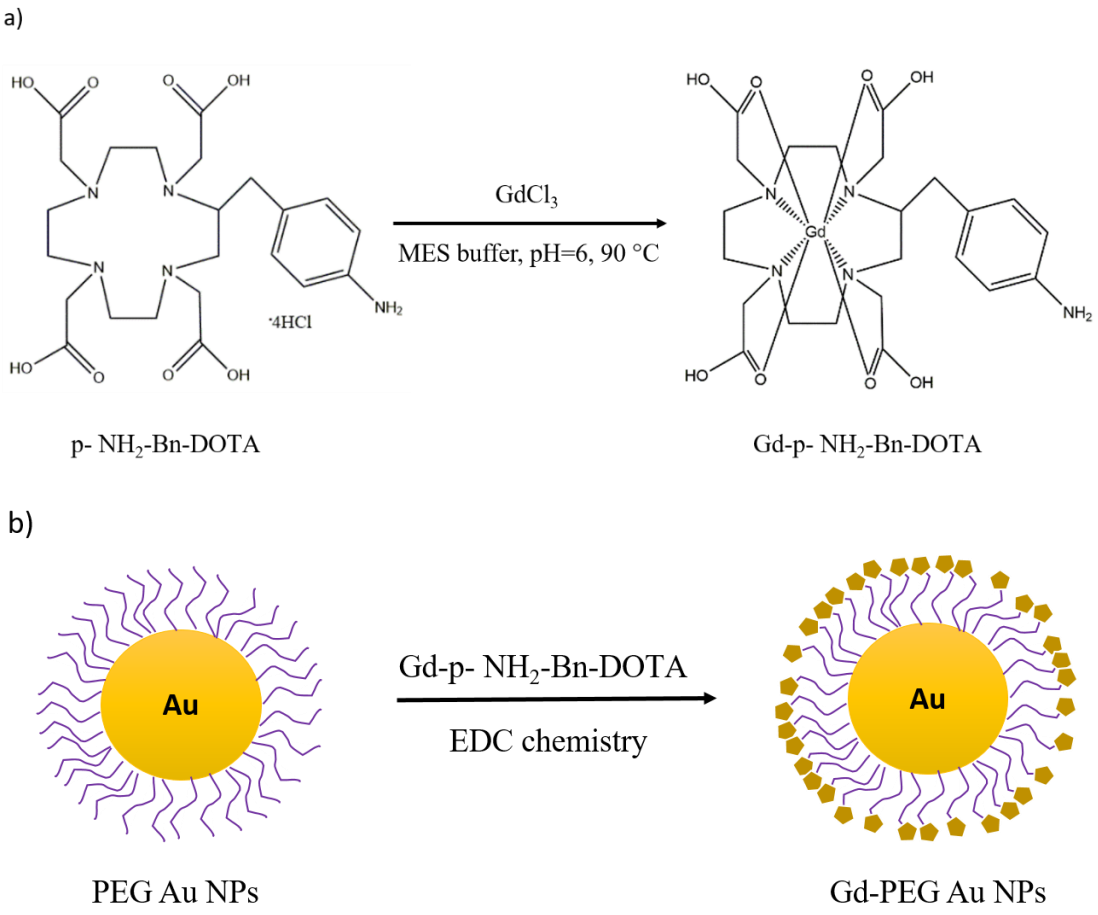

Figure 3-2. *Scheme of Gd labeled PEG Au NPs (Gd-PEG Au NPs) preparation. (a) Synthesis of Gd labeled p- NH2- Bn-DOTA. (b) Preparation of Gd labeled PEG Au NPs (Gd-PEG Au NPs).*

To make sure there was no nonspecific adsorption presence of Gd ions, Gd-PMA AuNPs and Gd- PEG Au NPs were both concentrated using Ultra-15 centrifugal filters (MWCO: 100k Da), and the filtrates were collected and measured by ICP-MS until no Gd signal was detected.

3.2.3 Protein labeling

3.2.3.1 Labeling of BSA with iodine (I-BSA)

1) Preparation of I-BSA

BSA (Sigma-Aldrich, #A2153) was labeled with 3-Iodobenzylamine hydrochloride (TCL, #I07101G). The labeling procedure was carried out by EDC chemistry. Briefly, 47.5 mg of BSA were dissolved in 3 mL of MES buffer (50 mM, pH 6) under gentle stirring at room temperature, and 26 mg of EDC powders were added to the protein solution for 20 min to activate the carboxyl group on BSA. 19 mg of iodine molecules were then added to the mixture (c_{BSA}/c_{Iodine} = 1:100) and incubated for 4 h.

2) Purification

The products above were transferred to an Amicon Ultra-4 centrifugal filter (MWCO: 3k Da, Merck, #36100101) and washed several times by centrifugation at 9,000 rpm for 30min to get rid of EDC by-products and excess iodine molecules. For each centrifugation, the filtrates were collected and measured by ICP-MS until no iodine molecules were detected. Herein, 4 times of washing was enough to remove unreacted iodine molecules. Afterward, the concentration of I-BSA was determined by Bradford assay according to the standard protocol.

3.2.3.2 Transferrin labeling with Europium (Eu-Tf)

1) Preparation of Eu-Tf

Holo-bovine-transferrin (Tf, 88k Da, Sigma-Aldrich, #T1283) was labeled with Europium (III) chloride ($EuCl_3$, Sigma-Aldrich, #429732). The protocol was carried out as follows. Firstly, 57 mg of Tf were dissolved in 20 mL of N-2-Hydroxyethylpiperazine-N'-2-ethane sulphonic acid (HEPES, #7365-45-9) buffer (100 mM, pH 8.5), 27 mg of difunctional chelator DOTA-NHS ester (Macrocyclcis, B-280) were then immediately added to Tf solution with gentle shaking for 4 h at room temperature. Herein, to avoid hydrolysis, DOTA- NHS ester should be prepared freshly. Afterward, an Ultra-4 centrifugal filter (MWCO: 3k Da) was used to filter DOTA-NHS ester hydrolysis by-products at 9,000 rpm for 30 min. The concentrated products

were transferred to MES buffer (50 mM, pH 6), followed by adding 5 mg of $EuCl_3$ with gentle shaking at 43°C for 1 h.

2) Purification

Excess and nonspecific adsorbed Eu ions were removed by an Amicon centrifugal filter (MWCO: 3k Da). Again, the filtrates were collected and measured by ICP-MS until no Eu atoms were detected. The same with I-BSA, 4 times washing was applied in our study. Afterward, the concentration of Eu-Tf was determined by Bradford assay according to the standard protocol.

3.2.3.3 Sodium dodecyl sulfate-polyacrylamide gel electrophoresis (SDS-PAGE)

Since both amino and carboxyl groups are on BSA molecules, it is inevitable to form linked BSA. To confirm this, SDS-PAGE was used to identify the labeled BSA.

Gel preparation. 10% of separating gel and 4% of stacking gel were prepared according to the recipes in Table 3-1. Generally, clean up all the stuff and set the casting frame (1.5 mm thickness of gap) on a casting stands before gel preparation. 7 mL of 10 % separating gel solution prepared according to the recipe was immediately poured into the gap of a casting frame. 3 mL of Milli-Q water was filled on top of the separating gel until an overflow. After ca. 20-30 min, Milli- Q water was discarded when gelation of separating gel solution. Next, stacking gel solution was prepared and immediately pipetted into the gap until an overflow. A 10-well comb was inserted carefully without trapping bubbles under the teeth. Waiting another 20-30 min until gelation.

Sample preparation. Protein samples were mixed with the same volume of loading buffer (2×Laemmli buffer, Bio-Rad, #161-0737) and boiled at 120 °C for 10 min.

Sample loading and running. Gels in glass plates were taken out from the casting frame and set in a cell buffer dam. Electrophoresis buffer was poured into the inner chamber of the cell buffer dam until an overflow, also in the outer chamber, a required amount of electrophoresis buffer was added. Next, 20 μL of samples and 10 μL of the marker were loaded into each well of stacking gel, respectively. Then cover the lid and set the volt at 100 V and time at 110 min.

Gel staining and destaining. After gel electrophoresis, the gel was taken out of the chamber carefully and placed in a glass beaker. Coomassie blue dye was added to ensure submerge the gel, and shaken at least for 2 h. Afterward, coomassie blue dye was discarded and a certain amount of destaining solution was added for 24 h. The destaining solution should be changed 2-4 times during that time. Finally, the gel was taken out and

photographed.

Table 3-1. *Recipes of separating and stacking gels.*

	Separating gel	*Stacking gel*
	4%	*10%*
40% Acrylamide solution (Bio-Rad, #1610146)	*0.5 mL*	*2.5 mL*
1.5 M Tris-HCl buffer, pH 8.8	-	*2.5 mL*
0.5 M Tris-HCl buffer, pH 6.8	*1.25 mL*	-
Mill-Q water	*3.23 mL*	*4.95 mL*
10% APS (Sigma, #215589)	*50 μL*	*100 μL*
TEMED (Sigma, #T9281)	*5 μL*	*4 μL*

APS: ammonium persulfate; TEMED: tetramethylethylenediamine

Table 3-2. *Recipe of coomassie blue dye.*

Coomassie blue G-250 (Roth, #9598.1)	*1 g*
Isopropanol (Sigma, #67630)	*250 mL*
Acetic acid (Sigma,#A6283)	*100 mL*
Mill-Q water	*650 mL*

Table 3-3. *Recipe of destaining solution.*

Methanol (Roth, #4627.6)	*400 mL*
Acetic acid	*100 mL*
Mill-Q water	*500 mL*

3.2.4 Cell culture

HeLa cells were used as the cell model, which was purchased from American Type Culture Collection (ATCC, Manassas, VA, USA). HeLa cells were cultured in the DMEM cell medium supplemented with 10% of fetal bovine serum (FBS, Biochrom, #S0615) and 1% of Gibco Penicillin-Streptomycin (P/S, Fisher scientific, 10.000 U/mL, #11548876) in an incubator with 5% of CO_2 at 37°C.

3.2.4.1 Cell viability

Before the endocytosis experiment, a resazurin assay was conducted to evaluate cell viability upon NPs/protein exposure[125].

In general, 100 μL of HeLa cell suspension at a density of 7.5×10^5 cells/mL in complete medium were seeded in a 96-well plate (Sarstedt, Germany) overnight. For each well, the growth area is 0.32 cm^2. The stock solution of as-prepared Au NPs was diluted by a complete cell medium to a concentration series from 0.234 μg/mL to 480 μg/mL (Table 3-4). Then, the old cell medium was aspirated and 100 μL of Au NPs suspension in cell media was added to each well. After 24 h incubation with Au NPs, cells were washed with 100 μL of PBS buffer once. Resazurin sodium salt (Sigma-Aldrich, # R7017) dissolved in the complete cell medium with a concentration of 25 μg/mL was added to each well and incubated in the incubator for 4 h. The color of the mixture changed from blue-violet to magenta, indicating resazurin was reduced to fluorescent resorufin. A fluorometer (Fluorolog-3, Horiba Jobin Yvon, USA) coupled with a microplate reader was used to record the emission spectra from 570 nm to 650 nm upon excitation at 560 nm. Three independent experiments were conducted and triplicates for each experiment. The intensity at 585 nm is the value of the maximum spectrum, and the intensity at 645 nm is the background. The cell viability (V) was calculated as follows normalized maximum intensity equation:

$$V = \frac{I(NP\_585nm) - I(NP\_645nm)}{I(ctr\_585nm) - I(ctr\_645nm)} \times 100\%$$

I (NP_585 nm): Fluorescence intensity of cells with NPs exposure at 585 nm
I (NP_645 nm): Fluorescence intensity of cells with NPs exposure at 645 nm
I (ctr_585nm): Fluorescence intensity of cells without NPs exposure at 585nm
I (ctr_645nm): Fluorescence intensity of cells without NPs exposure at 645nm

Meanwhile, we evaluated the toxicity of labeled proteins (I-BSA and Eu-Tf) and free ions (Gd^{3+} and Eu^{3+}) as the protocol aforementioned. The exposure concentrations were listed in Table 3-5 and Table 3-6. Of note, we did the cellular uptake experiment later in DMEM cell medium without 10% FBS, therefore, the cellular toxicity assay of labeled proteins was also done without FBS.

Table 3-4. *Exposure concentrations of Au NPs for cell viability assay. Each concentration was diluted by a two-fold serial dilution.*

Samples	***Concentration range (μg/mL)***
Gd-PMA Au NPs	*0.234-480*
Gd-PEG Au NPs	*0.234-480*

Table 3-5. *Exposure concentrations of labelled proteins for cell viability assay. Each concentration was diluted by a two-fold serial dilution.*

Samples	***Concentration range (μg/mL)***
Eu-Tf	*0.195-400*
I-BSA	*0.390-800*

Table 3-6. *Exposure concentrations of free ions (Eu or Gd) for cell viability assay. Each concentration was diluted by a two-fold serial dilution.*

Samples	***Concentration range (ng/mL)***
Eu ions	*1.465-3000*
Gd ions	*1.465-3000*

3.2.4.2 Cellular uptake experiment

1) Au NPs-proteins complexes endocytosis study

2 mL of HeLa cell suspension in DMEM complete medium were seeded in a 6-well plate (Sarstedt, Germany) with a growth area of 8.87cm^2 at a density of 2.0 ×10^5 cells/mL. On the next day, 120 μg/mL of Au NPs were mixed with 200 μg/mL of I-BSA and 50 μg/mL of Eu-Tf in a DMEM cell medium without FBS. The old medium in each well was discarded and the mixed Au NPs-proteins complexes were added immediately. After 0, 6, 12, 18, and 24 h of incubation, the supernatants in the plate were collected for ICP- MS measurement, and cells were washed with PBS buffer three times to get rid of the non-endocytosed complexes, followed by the addition of 200 μL of 0.05% trypsin-EDTA (Thermo Fisher, 0.05%, #2530054) to detach cells. 1 mL of PBS was then added to each well, all the cells were collected and 10 μL of cell suspension was taken and counted by cell counting chamber (Neubauer Chamber, Celeromics Technologies, Spain). Next, the rest cell suspensions were centrifuged at 4,000 rpm for 10 min, the cell pellets were collected in 2 mL Eppendorf tubes for ICP-MS measurements. Three independent experiments were conducted and duplicated for each batch.

2) Free ions endocytosis study

To better compare with NPs cellular uptake study, control samples containing only Eu ions or Gd ions were evaluated. Herein, the same concentration of free ions in DMEM cell medium as the labels from Au NPs proteins complexes were prepared, i.e., HeLa cells exposed to Gd ions with the same Gd amount of Gd- PMA Au NPs and Gd-PEG Au NPs, HeLa cells exposed to Eu ions with the same Eu amount of Eu- Tf. Hela cells at a density of 2.0 $\times 10^5$ cells/mL in a 6-well plate were exposed to the free ions solution. Time- dependent incubation as mentioned above was carried out. The supernatant and cell pellets were collected and determined the concentration by ICP-MS.

3.2.4.3 ICP-MS measurement

1) ICP-MS sample preparation

We collected the Au NPs-proteins complexes before exposure, supernatant after incubation, and cell pellets, and then measured the concentrations via ICP-MS. The protocols of ICP-MS sample preparation are as follows.

NPs-proteins complexes and supernatant digestion. 50 μL of samples were digested in 75 μL of concentrated nitric acid (HNO_3, 67 wt%, Fisher chemical, USA) overnight, then 150 μL of concentrated HCl was added overnight. On the next day, 2 mL of 2 % of HNO_3 was added to dilute the samples and transferred into a 5 mL PFA tube for ICP-MS measurement.

Cell pellet digestion. For the cell pellets collected in 2 mL Eppendorf tubes, 75 μL of concentrated HNO_3 was added overnight, then 150 μL of concentrated HCl was added to samples overnight. On the third day, 2 mL of 2 % of HNO_3 was added to diluted samples and transferred into 5 mL PFA tubes ready for ICP- MS measurement.

2) ICP-MS measurement and quantification

All the samples were measured by ICP-MS (Agilent 7700 Series, USA). The mass concentrations of Au, Gd, Eu, and I in PFA tubes were recorded. By multiplying dilution factors and sample volumes, the initial masses of each element were obtained.

3.2.5 Protein adsorption measurement

3.2.5.1 Preparation of PMA QDs and PEG QDs

Hydrophobic CdSe/ZnSe/ZnS core-shell-shell quantum dots (QDs) were provided by Fraunhofer Zentrum für Angewandte Nanotechnologie (CAN).

1) Preparation of PMA QDs

PMA-coated CdSe/ZnSe/ZnS QDs were prepared using our normal PMA synthesized aforementioned. Briefly, 0.4 mL of hydrophobic CdSe/ZnSe/ZnS QDs (15.8 μM) in hexane and 0.2 mL of PMA (0.5 M) in chloroform were injected into a round-bottom flask with 50 mL of $CHCl_3$. The mixture was slowly evaporated three times under a reduced pressure vacuum system until a thin film formed. 15 mL of borate buffered saline was added under sonication for several seconds. When QDs were completely dispersed in buffer, three times ultracentrifugation (40,000 rpm, 30 min) was performed to wash out the excess PMA micelles. The precipitate was collected and dispersed in 5 mL of Milli-Q water.

2) Preparation of PEG QDs

0.2 mL of hydrophobic CdSe/ZnSe/ZnS QDs (15.8 μM) in hexane was injected into 20 mL of $CHCl_3$, followed by adding 50 mg of HS-C_2H_4-CONH-PEG-O-C_3H_6-COOH (3k Da). The mixture was stirred at 50°C overnight. Then, the solvent was evaporated completely by an evaporator and 5 mL of Milli-Q water was added to dissolve the PEGylated QDs. Excess PEG molecules were washed twice by a centrifuge filter (100k Da), and large aggregates were removed by three times centrifugation (12,000 rpm, 10 min).

3.2.5.2 FCS measurement

Herein, FCS measurements were performed in an LSM 880 upright microscope (Zeiss, Germany) with a C- Apochromat 40×/1.20 W Corr M 27 objective (Zeiss, Germany) at 25 °C. A laser at 488 nm was used as an excitation light source. A brief measurement process was introduced below. For more detailed protocol, please refer to the guide to basic FCS experiments provided by Zeiss.

Calibration of observation volume. Before the measurement, fluorophore rhodamine 6G (R6G) with a diffusion coefficient of 280 μm^2 /s was used to calibrate the observation volume. The lateral focus radius (ω_r) and axial focus radius (ω_z) were determined to be 199 nm and 750 nm, respectively.

Samples preparation. Proteins (BSA or Tf) dissolved in Milli-Q water with a series of concentrations were incubated with a certain amount of PMA-QDs and PEG-QDs for 30 min. 40 μL of samples were put in a 35mm glass-bottom dish (ibidi Gmbh, Germany, #81218-200) and covered with a cover glass (Zeiss, Germany, #10474379). The dish with the sample was assembled with the lid and placed upside down under the microscope.

Samples measurement. Adjust the focus to ensure it is on the samples. The signals were recorded in 10 times series, and each time series were measured 10 times. The average was obtained by averaging the repeats of different time series, and the standard deviation was calculated. It is worth noting that adjusting laser power to keep the value of counts per molecule (CPM) at 1-15 kHz molecule per volume could get the best signal- to- noise (S/N). The movement of nanoparticles in this scenario was considered a simple independent translational diffusion. And the correlation function is defined with the following equations, provided by Zeiss ZEN software:

$$G(\tau) = 1 + A * \sum_{i=1}^{3} \frac{\Phi_i}{(1+(\frac{\tau}{\tau_{d,i}})^{\alpha_i})^{e_{d1}} * ((1+(\frac{\tau}{\tau_{d,i}})^{\alpha_i} * \frac{1}{S})^{0.5})^{e_{d2}}}$$

$$A = \frac{S}{N}$$

$$\Phi_i = \frac{f_i * \eta_i^2}{\sum_{1=i}^{3} (f_i * \eta_i)^2}$$

$$S = \frac{\omega_z}{\omega_r}$$

G (τ): correlation function

A: amplitude

N: average number of molecules in the observation volume

i: index of component (1, 2, 3)

Φ_i: fractional intensity

f_i: fraction of molecules

η_i: molecular brightness

$\tau_{d,i}$: diffusional correlation time

S: structural parameter

ω_z: axial focus radius

ω_r: lateral focus radius

α_i: anomaly parameter

In the present case, there is only one component (QDs or R6G) in the solution, i is supposed to be 1, Φ_i is also

1, and α_i is 1 due to free diffusion. And e_{d1} and e_{d2} are fixed value 1 for three-dimensional diffusion. Therefore, the average number of molecules N and diffusional correlation time τ_d could be fitted.

3.3 Results and discussions

3.3.1 Characterization of Gd-PMA Au NPs and Gd-PEG Au NPs

To determine the molar concentration of Au NPs, a UV-Vis spectra-based method was employed[126]. Briefly, the absorbance of 17 nm Au NPs with a plasmonic peak at 518 nm was recorded by a UV-Vis spectrometer. The extinction coefficient (ε) at this wavelength was calculated by the following equation:

$$\ln \varepsilon = k \ln D + a$$

Where D is the core diameter, k = 3.3211, and a = 10.80505. Therefore, $\varepsilon = 6.01 \times 10^8\ M^{-1}\ cm^{-1}$. According to the Lambert-Beer law:

$$A = \varepsilon bc$$

Where A is the absorption intensity, and b is the optical path length (1 cm). By calculation, the sample concentration c is acquired.

The Gd-PMA Au NPs and Gd-PEG Au NPs were characterized by UV-Vis absorption spectroscopy, TEM, DLS, and zeta potential shown in Figure 3-3 to Figure 3-6. For both Gd-PMA Au NPs and Gd- PEG Au NPs, Gd labeling did not make the plasmonic peak shift. TEM images were acquired with a JEM- 1400PLUS HC microscope (JEOL, Germany). By measuring the diameters of 100 different Au NPs from TEM images, the histograms and Gaussian fitting were plotted. For Gd- PMA Au NPs, the core diameter was 17.01 ± 0.03 nm, and for Gd-PEG Au NPs, the core diameter was 17.21 ± 0.05 nm. The hydrodynamic diameter of two kinds of Au NPs in Milli- Q water was measured by a DLS Nano ZS (Red badge) (Malvern, England, ZEN3600) including a He-Ne gas laser with the beam wavelength at 633 nm. 0.65 mL of Au NPs dispersion was equilibrated for 3 min in a transparent UV-cuvette (Sarstedt, Germany, #67.758.001). The size of Gd- PMA Au was 24.37 ± 0.87 nm and for Gd-PEG Au NPs was 28.08 ± 0.81 nm. Still, the increased diameter than the size of TEM images was due to the hydrated layer. Overall, compared to nonlabeling Au NPs, there were no significant changes after Gd labels modification. Zeta potentials were measured with the same instrument as DLS. 1 mL of Au NPs dispersion with a certain concentration was injected in a disposable capillary zeta cell (Malvern, UK, #DTS1070). All the samples were equilibrated for 3 min before measurement and carried out at 25°C. The zeta potentials were - 29.7 ± 1.91 mV and -42.6 ± 0.49 mV for

Gd-PMA Au NPs and Gd-PEG Au NPs, respectively.

To validate BSA was crosslinked after labeling with iodine, SDS-PAGE was performed and shown in Figure 3-7, compared to the nonlabeling BSA, it is obvious that there were a lot of I-BSA accumulated at the beginning of the gel (molecular weight > 250k Da), which means the I-BSA was a multimer.

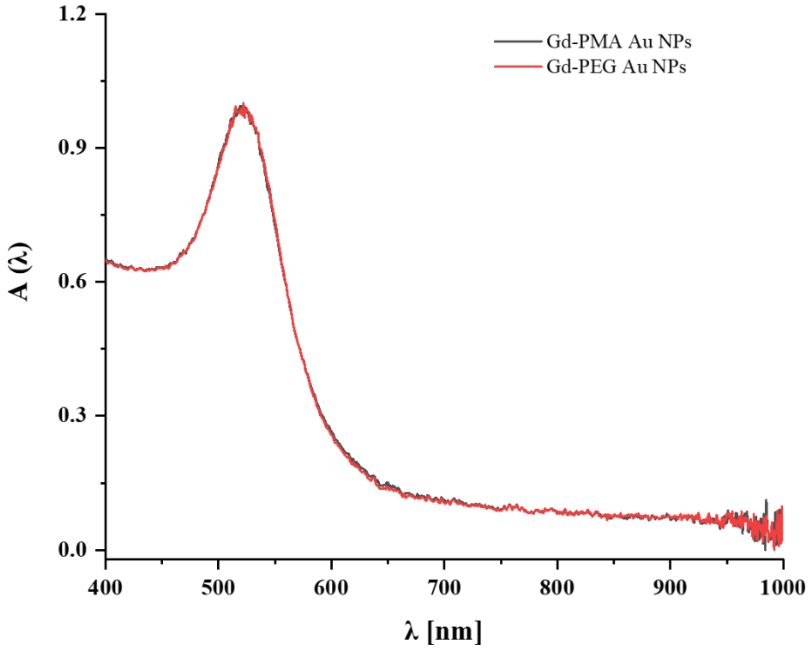

Figure 3-3. *Normalized UV-Vis spectra of Gd-PMA Au NPs (black line) and Gd-PEG Au NPs (red line).*

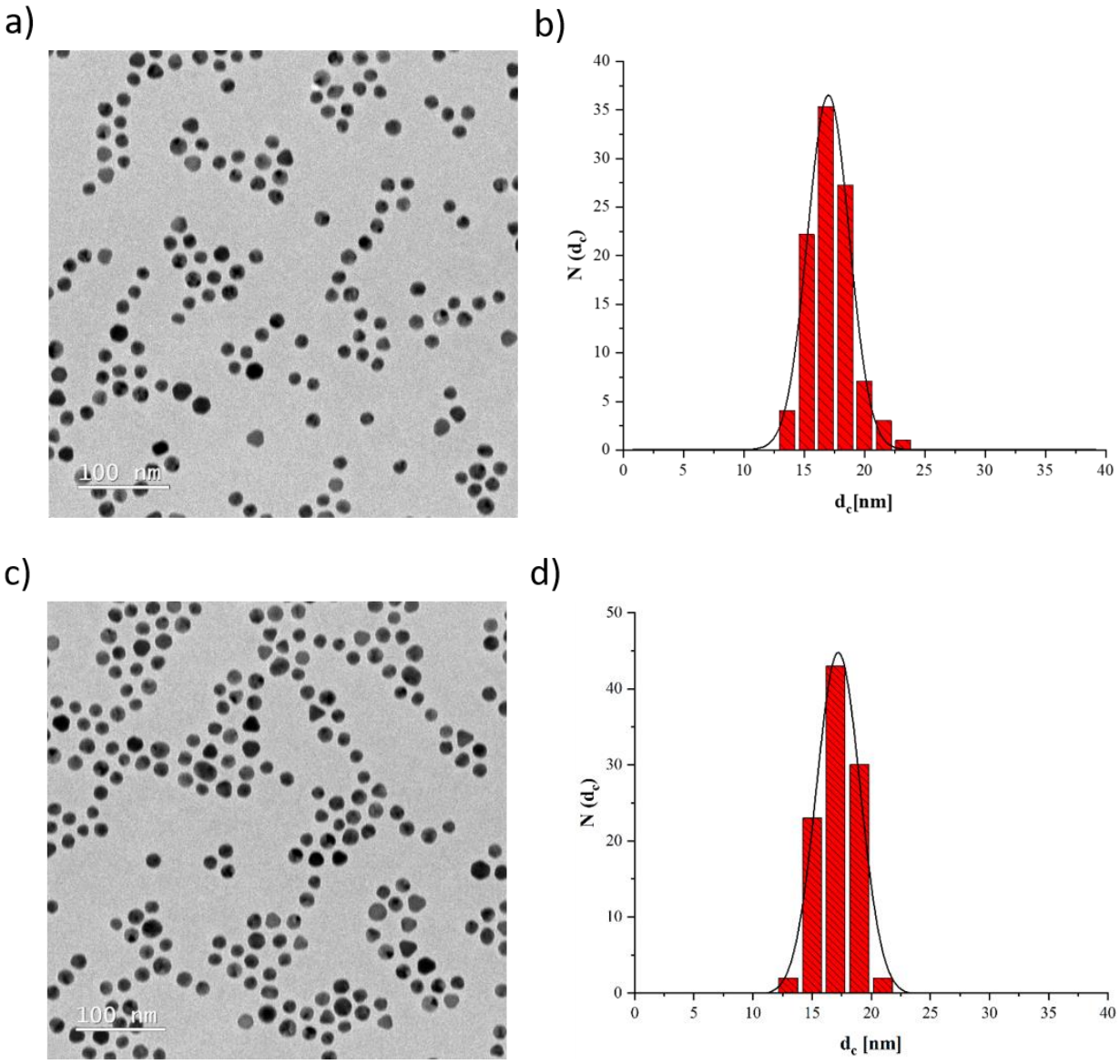

Figure 3-4. *TEM images and size distribution of Au NPs. (a) TEM image of Gd-PMA Au NPs. (b) Histogram and Gaussian fitting of the size distribution of Gd-PMA Au NPs core. (c) TEM image of Gd-PEG Au NPs. (d) Histogram and Gaussian fitting of the size distribution of Gd- PEG Au NPs core (TEM images were taken by Andreas Kornowski).*

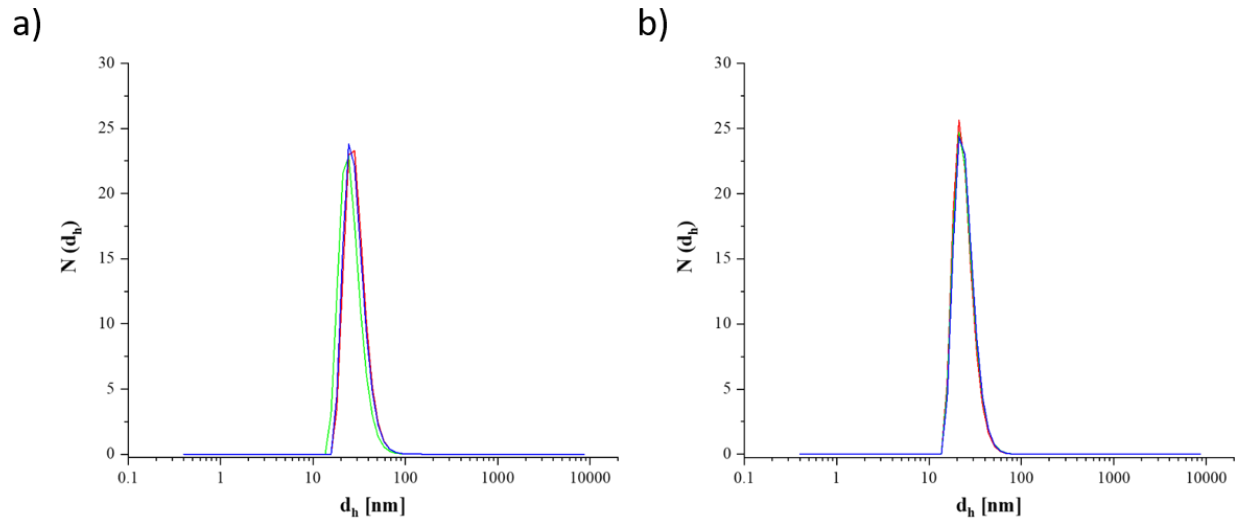

Figure 3-5. *Hydrodynamic diameters of Au NPs. (a) The hydrodynamic diameter of Gd- PMA Au NPs in Milli-Q water. (b) The hydrodynamic diameter of Gd-PEG Au NPs in Milli- Q water.*

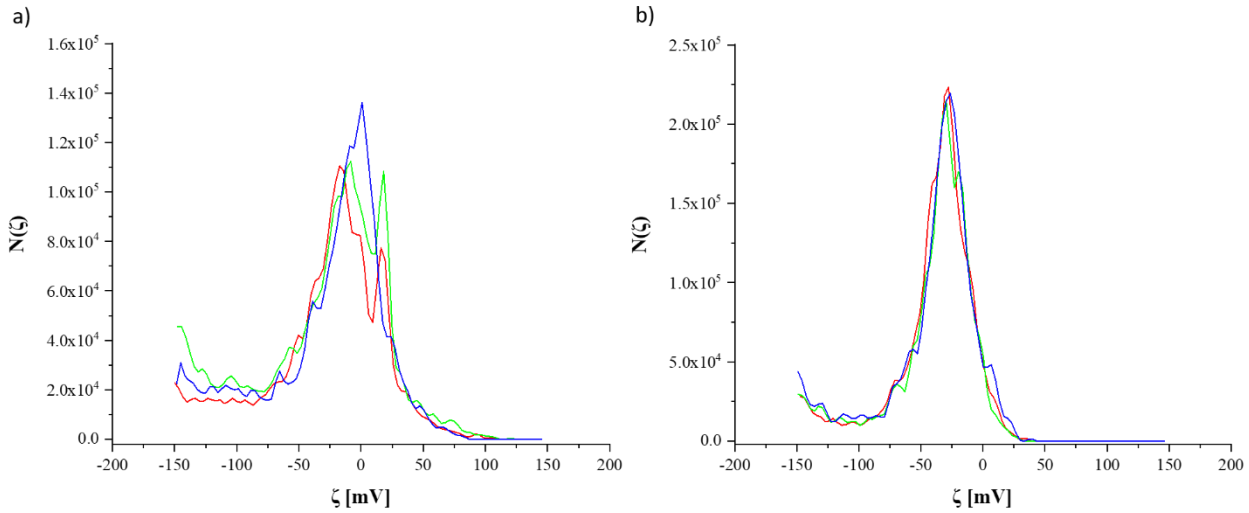

Figure 3-6. *Zeta potentials of Au NPs. (a) Zeta potential of Gd-PMA Au NPs dispersed in Milli-Q water. (b) Zeta potential of Gd-PEG Au NPs dispersed in Milli-Q water.*

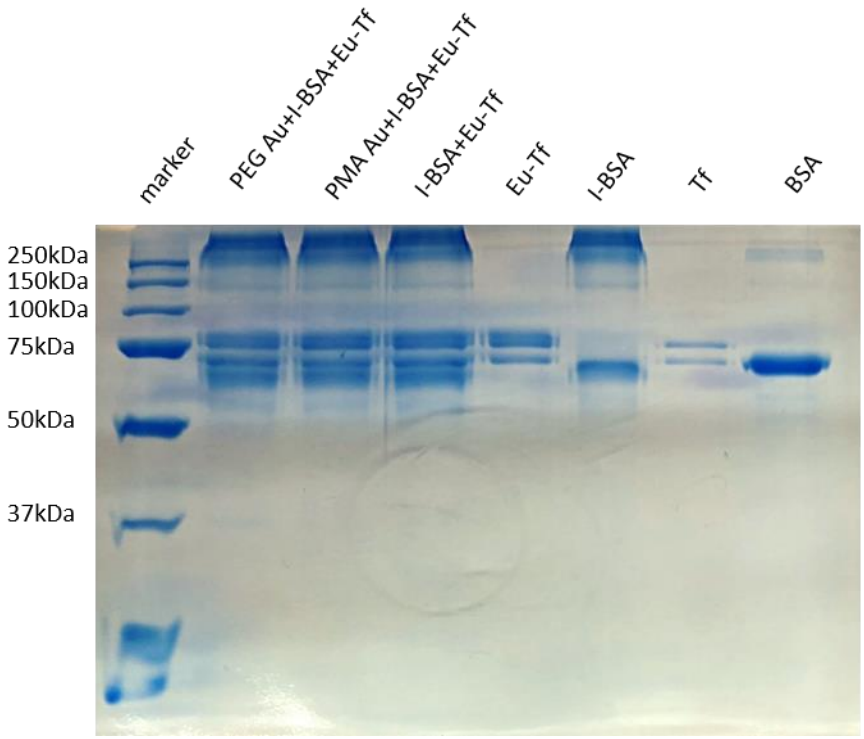

Figure 3-7. *Image of protein samples separated by SDS-PAGE. I-BSA was crosslinked whereas Eu-Tf was still in a single protein molecule level.*

3.3.2 Cellular uptake study

3.3.2.1 Cell viability

Resazurin assay was widely used to quantify the number of live cells and monitor cell viability and material cytotoxicity[127]. Non-fluorescent blue resazurin in an oxidized state was reduced to a red resorufin by the mitochondrial respiratory chain of live cells. The products, resorufin, can be measured by the fluorometric/colorimetric method, which is directly proportional to the number of live cells. The excitation and emission peak of resorufin can be traced at 560 nm and 585 nm, respectively.

The concentration-dependent cell viability curves upon NP-proteins complexes exposure were plotted in Figure 3-8 and fitted with a sigmoidal function, which is expressed as follows:

$$V = \frac{I_{\max} - I_{\min}}{1 + \left(\frac{c_{NP}}{c_{NP\_50}}\right)^{p}} + I_{\min}$$

Where c_{NP_50} is the NPs concentration at which cell viability has been reduced to half of its activity (IC50). The value of IC50 of Gd-PMA Au NPs was 589.32 μg/mL and for the Gd-PEG Au NPs group, there was no decrease in cell viability occurred than the highest exposure concentration. Then, we evaluated the toxicity of labeled BSA and Tf shown in Figure 3-9. The cell viabilities of I-BSA or Eu-Tf were no significant changes among exposure concentrations. We also evaluate the toxicity of free ions (Eu^{3+} and Gd^{3+}) in the DMEM cell medium with 10 % FBS, and the results shown in Figure 3-10. The values of IC50 of Eu ions and Gd ions were 2.18 μg/mL and 1.58 μg/mL, respectively.

Therefore, we finally used 120 μg/mL Au NPs, 200 μg/mL I-BSA, and 50 μg/mL Eu-Gd μg/mL as the safety concentrations in the following cellular uptake study. In this case, the exposure concentrations of Eu and Gd ions were both lower than 1 μg/mL, which is the limit of safety concentrations.

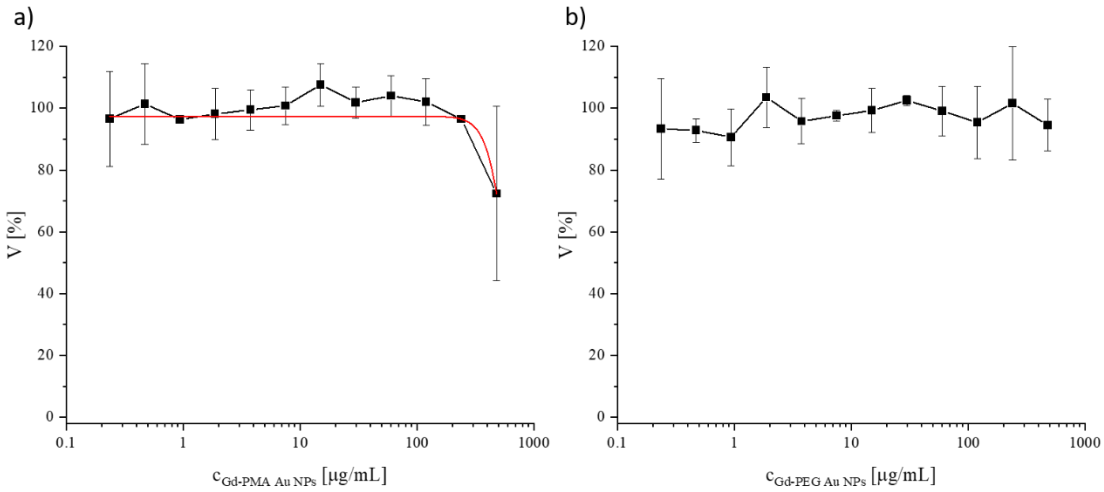

Figure 3-8. *Cell viability of HeLa cells exposed to Au NPs in DMEM cell medium (with 10 % FBS) for 24 h. (a) Gd-PMA Au NPs. (b) Gd-PEG Au NPs.*

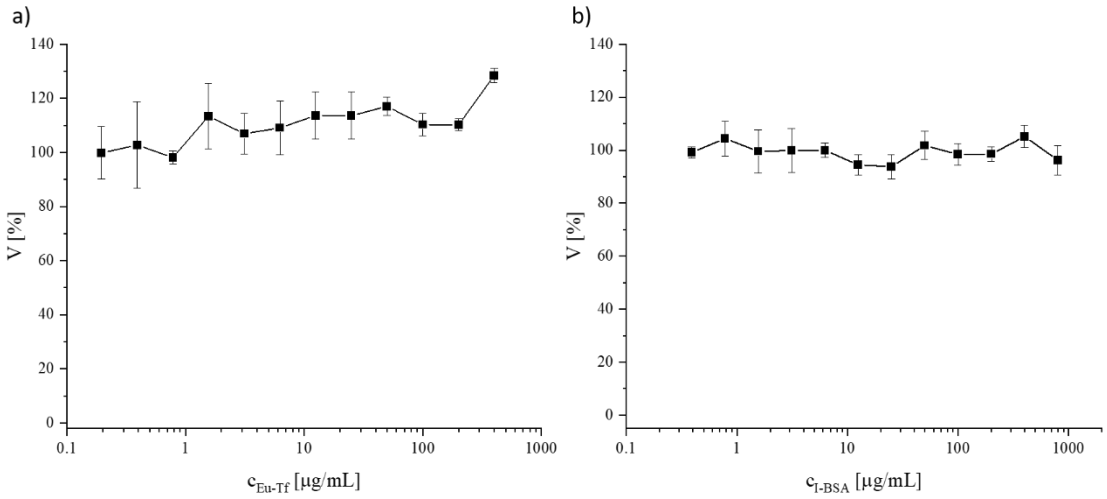

Figure 3-9. *Cell viability of HeLa cells exposed to Eu-Tf or I-BSA in DMEM cell medium (without 10 % FBS) for 24 h. (a) Eu-Tf. (b) I-BSA.*

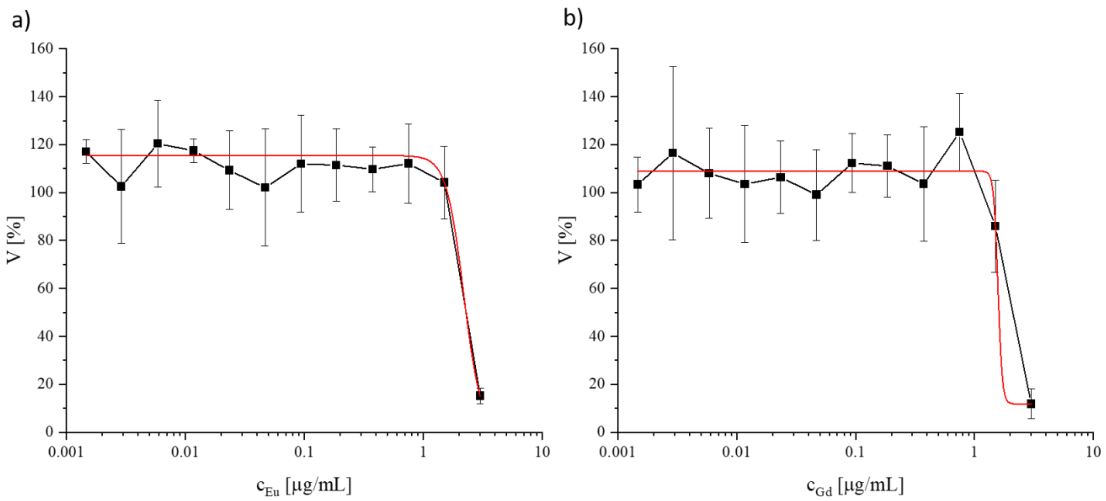

Figure 3-10. *Cell viability of HeLa cells exposed to Eu or Gd ions in DMEM cell medium (without 10 % FBS) for 24 h. (a) Eu ions. (b) Gd ions.*

3.3.2.2 Quantification of cellular uptake by ICP-MS

With the multil-labeled NPs and proteins, the cellular uptake was measured by ICP-MS. The exposure amount of gold was ca. 275-300 μg per well (137-150 μg/mL), which is a little higher than the theoretical exposure concentration. But as proved in cell viability, it is still a safe concentration. As shown in Figure 3-11, the initial exposure amounts of Eu (Tf) and iodine (BSA) in each group were almost the same. We also measured the amounts of each element in the supernatant at 4 different incubation time points shown in Figure 3-12. There was almost no decrease of each element in supernatants, demonstrating the extracellular NPs-proteins complexes were an infinite reservoir.

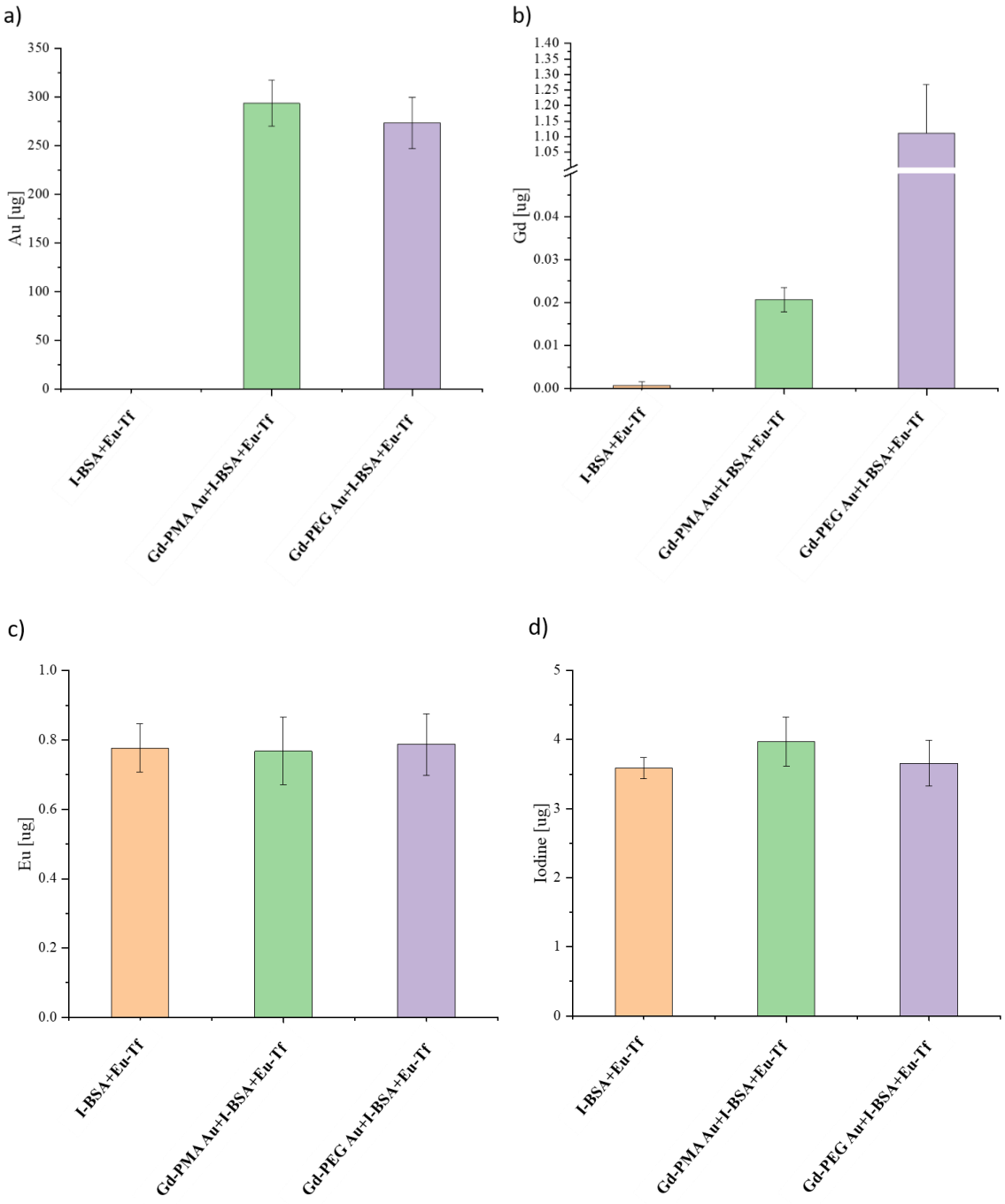

Figure 3-11. *Mass of each element of different Au NPs-proteins complexes determined by ICP- MS before exposure. (a) Au. (b) Gd. (c) Eu. (d) Iodine.*

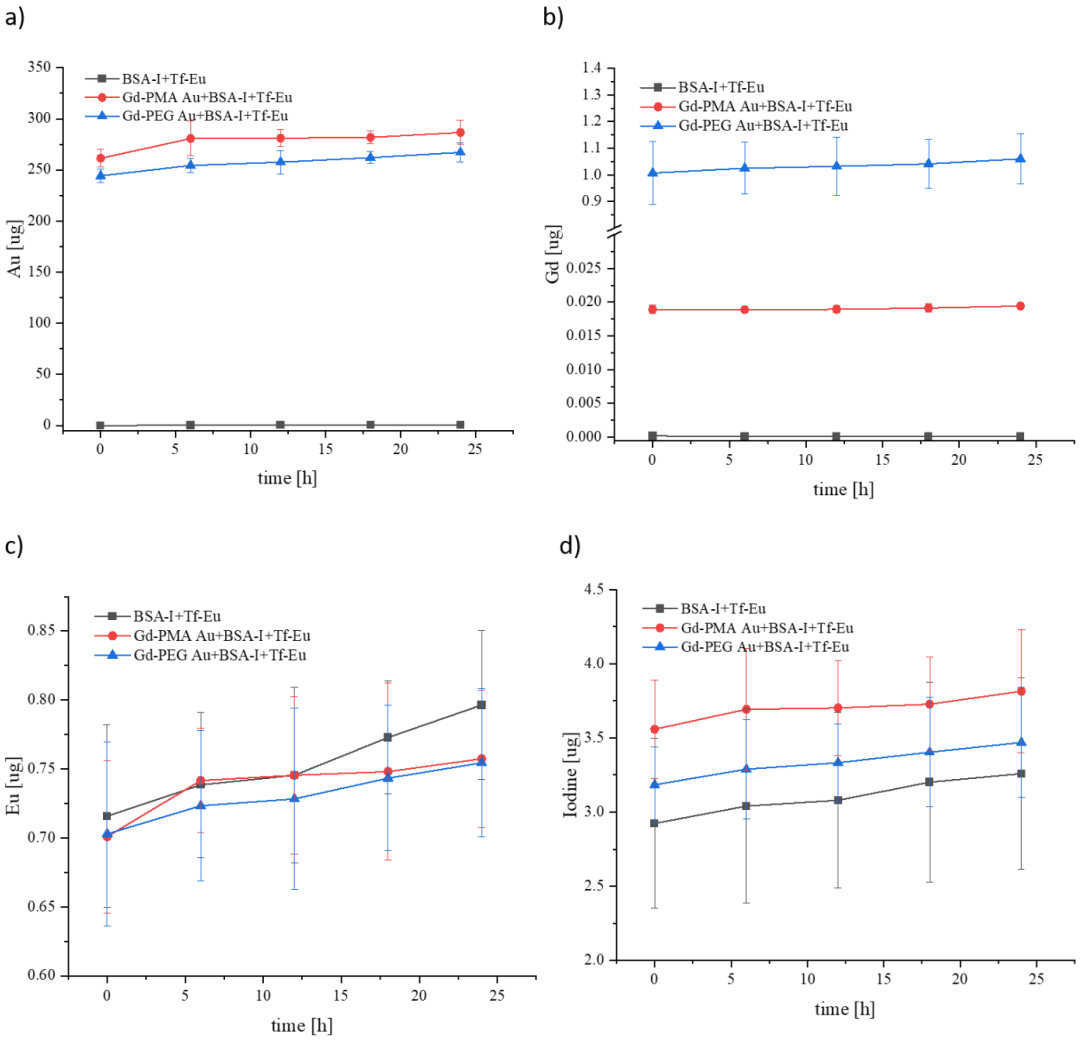

Figure 3-12. *Time-dependent mass changes of each element of different Au NPs-proteins complexes determined by ICP- MS in supernatants (0, 6, 12, 18, and 24 h). (a) Au. (b) Gd. (c) Eu. (d) Iodine.*

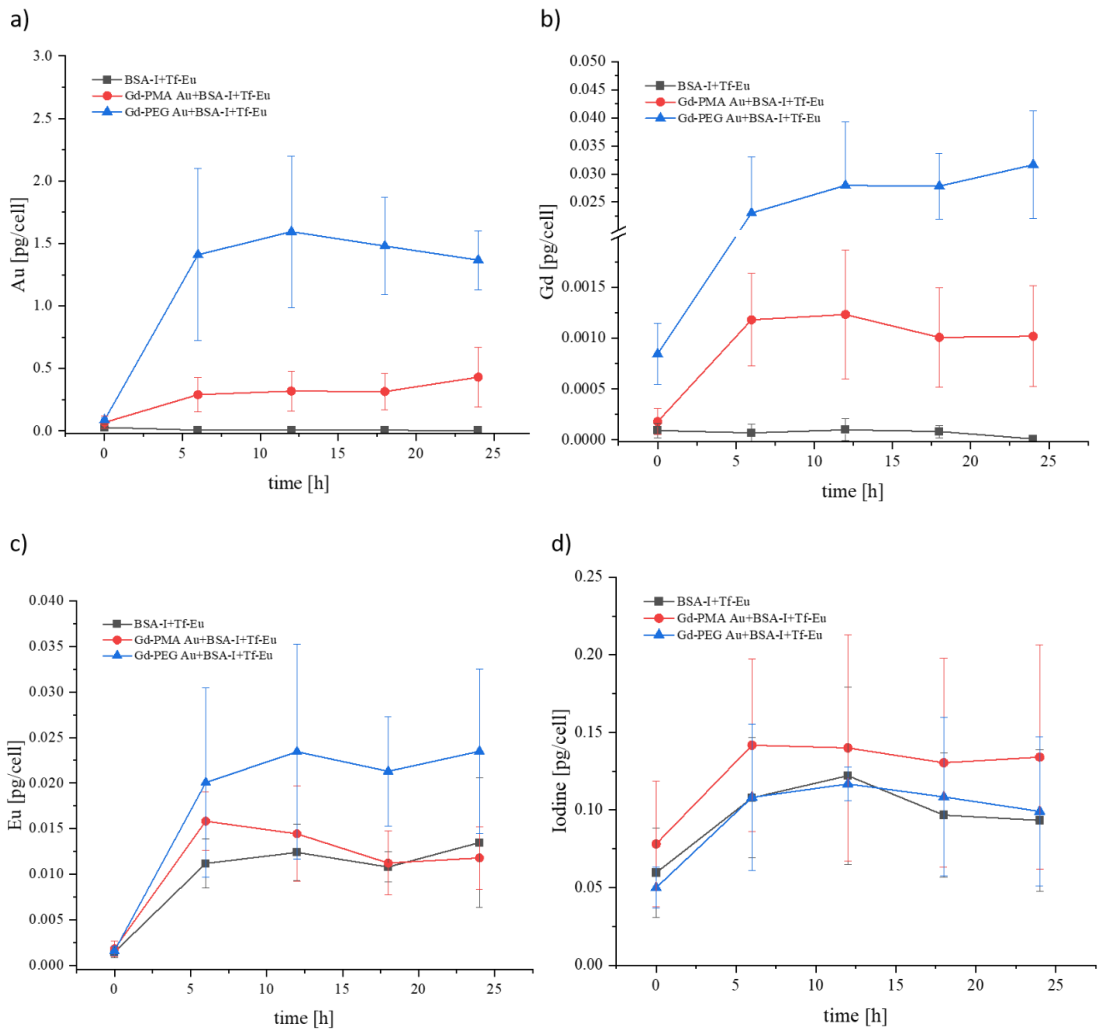

Figure 3-13. *Time-dependent mass changes of each element of different AuNPs-proteins complexes in a single cell (0, 6, 12, 18, and 24 h). (a) Au. (b) Gd. (c) Eu. (d) Iodine.*

After internalization, the accumulation of each element was increased as the incubation time, via dividing by the cell numbers, we obtained the accumulation of each element in a single cell (Figure 3-13). All elements reached a plateau after 6 h, suggesting the internalization occurred within a short time. There are some studies reported that the reduction of intracellular NPs was mainly due to cell division[128-129], which means cells will switch off the internalization process when there are enough contents in the cells. In addition, the uptake of PEGylated Au NPs was much more than that of PMA-coated NPs, which means more PEGylated NPs were taken up by cells. However, in most studies, PEGylation was used to prolong the circulation time in the body[130-131]. More interestingly, the behaviors of Tf and BSA were different, where Tf has the same trend as Au, whereas although pretty lower PMA coated Au NPs were taken up by HeLa cells, more BSA proteins were delivered into cells than PEGylated Au NPs, suggesting the formation of different protein corona around two types of NPs. It is worth noting that in order to simplify our model, we used a DMEM cell medium without FBS. Therefore, the composition of protein corona was only Tf and BSA mixture with different ratios.

We also performed a control experiment for the Gd ions and Eu ions uptake at different incubation times. Herein, the same amount of Gd or Eu ions as the labeled Au NPs were exposed to HeLa cells, as shown in Figure 3-14, unlike NPs, most ions in supernatants were internalized into cells within 6 h, indicating the significantly different internalization processes between NPs and ions. Moreover, after 6 h, the accumulation of ions decreased as time increased.

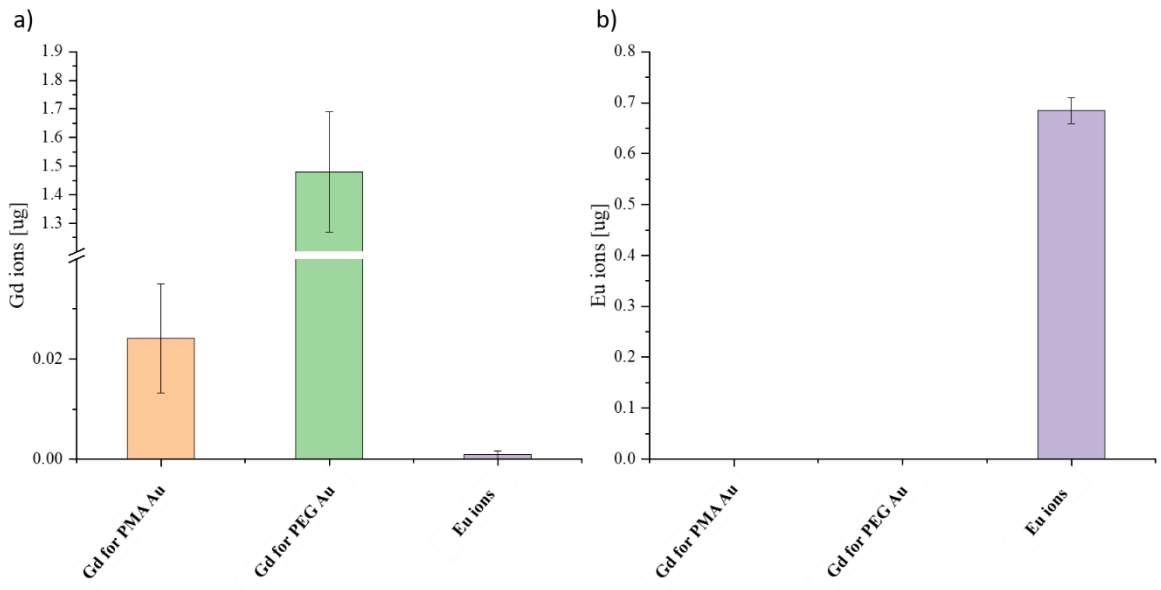

Figure 3-14. *Mass of different free ions determined by ICP-MS before exposure. (a) Gd ions mass before exposure, orange column: Gd ions with the same amount of Gd in Gd-PMA Au NPs, green column: Gd ions with the same amount of Gd in Gd-PEG Au NPs. (b) Eu ions before exposure.*

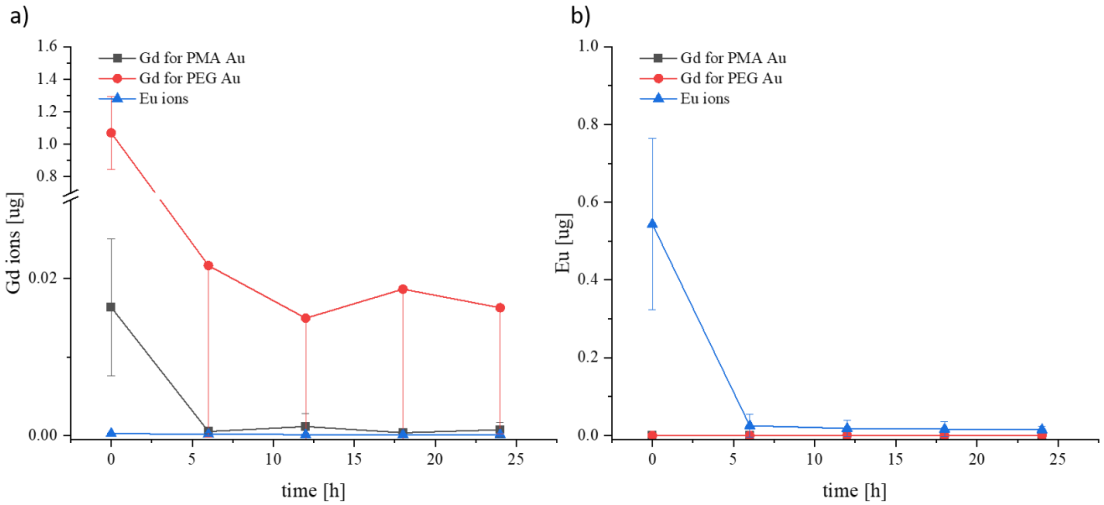

Figure 3-15. *Time-dependent mass changes of different ions determined by ICP-MS in supernatants (0, 6, 12, 18, and 24h). (a) Gd ions. (b) Eu ions.*

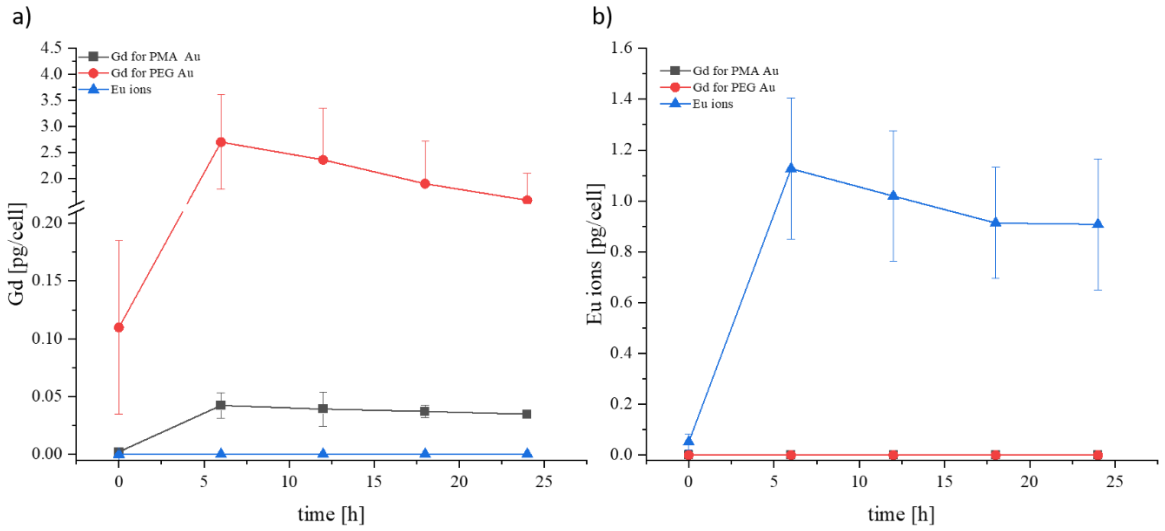

Figure 3-16. *Time-dependent mass changes of different ions in a single cell (0, 6, 12, 18, and 24 h). (a) Gd ions. (b) Eu ions.*

3.3.3 Protein adsorption measurement

3.3.3.1 Characterization of QDs

The TEM images of hydrophobic CdSe/ZnSe/ZnS QDs dispersed in hexane, hydrophilic PMA-QDs, and PEG-QDs dispersed in Milli-Q water were obtained by a JEM 2100F UHR microscope (JEOL, Japan). The histograms of size distributions of NPs were also plotted via counting 100 NPs by ImageJ software. As shown in Figure 3-17, Figure 3-18, and Figure 3-19, the sizes were 5.58 ± 0.01 nm, 5.09 ± 0.05 nm, and 5.57 ± 0.06 nm, respectively. The emission spectra were recorded upon excitation at the wavelength of 488 nm by a fluorometer (Figure 3-20). The emission spectrum of PMA-QDs was similar to that of hydrophobic CdSe/ZnSe/ZnS QDs, whereas there is a redshift for PEG-QDs, which is due to the length of PEG ligands (3k Da) was ca. 18 nm, much longer than those ligands used in other two NPs. Anyway, this will not affect the subsequent protein adsorption experiments. The Zeta potentials were also measured using Malvern NanoZS (Figure 3-21), which were -52.5 ± 0.44 mV (PMA-QDs) and -50.7 ± 0.72 mV (PEG- QDs), respectively, indicating excellent colloidal stability.

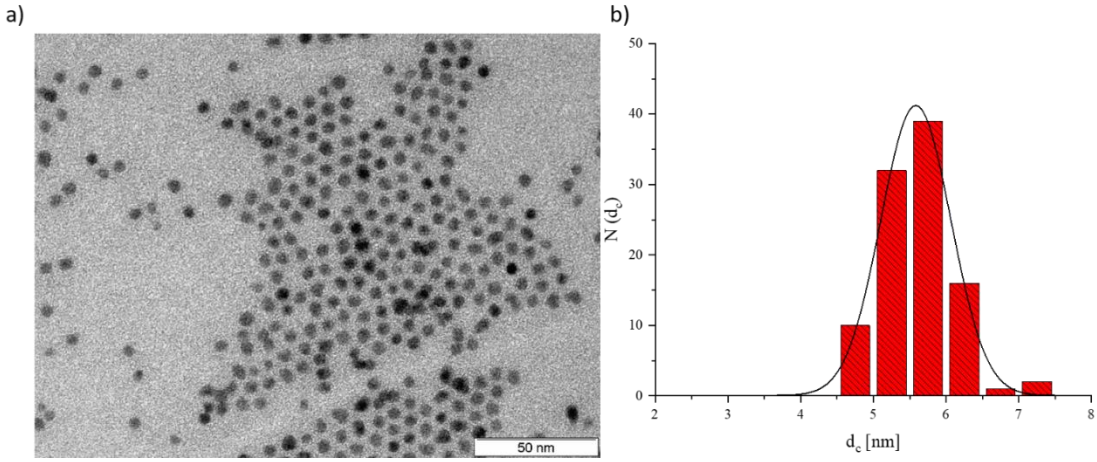

Figure 3-17. *(a) TEM image hydrophobic CdSe/ZnSe/ZnS QDs in hexane. (b) Histogram of hydrophobic CdSe/ZnSe/ZnS QD and Gaussian fitting (TEM image was taken by Stefan Werner).*

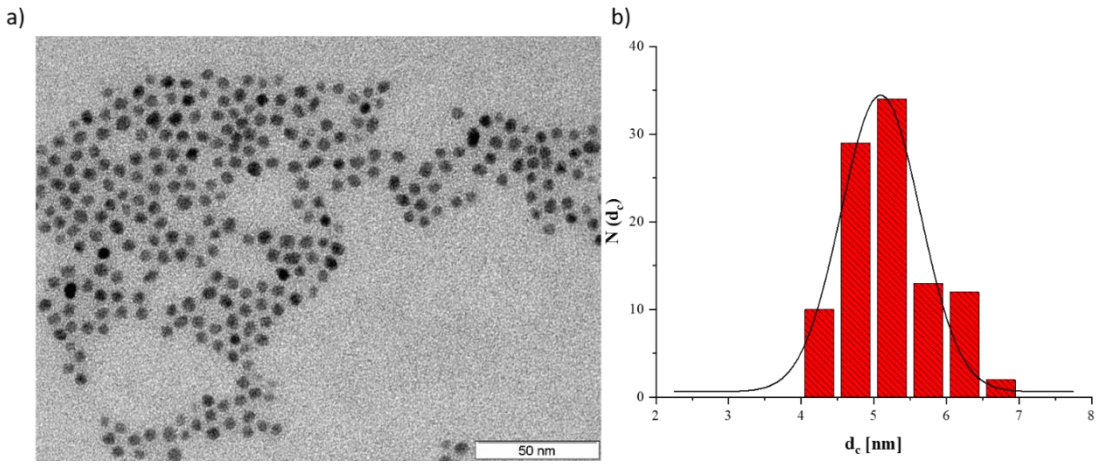

Figure 3-18. *(a) TEM image of PMA-QDs in Milli-Q water. (b) Histogram of PMA-QD and Gaussian fitting (TEM image was taken by Stefan Werner).*

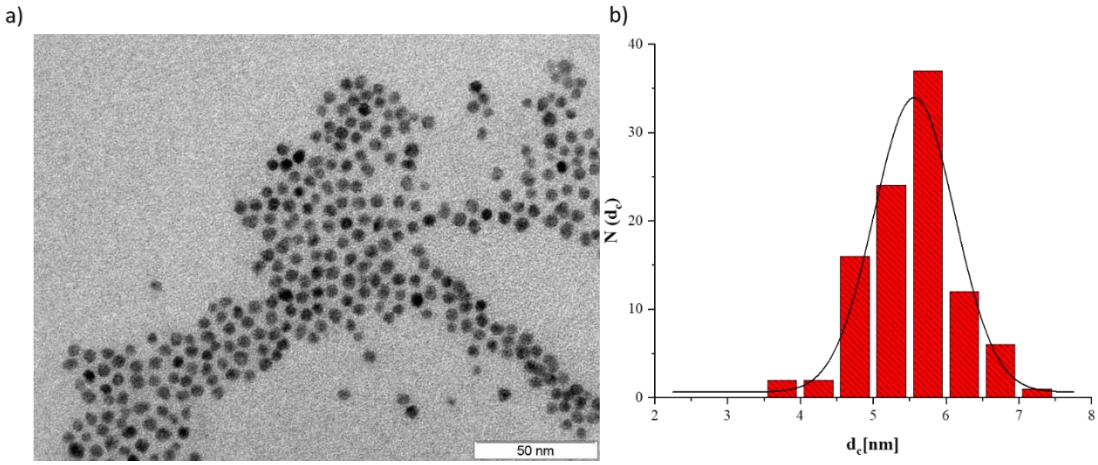

Figure 3-19. *(a) TEM image of PEG-QDs in Milli-Q water. (b) Histogram of PEG-QD and Gaussian fitting (TEM image was taken by Stefan Werner).*

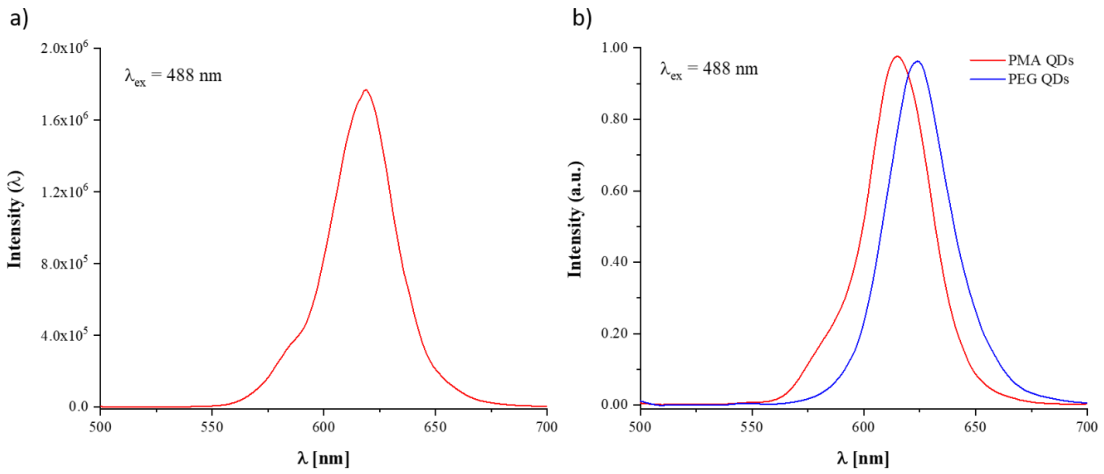

Figure 3-20. *Emission spectra of QDs upon excitation at 488 nm. (a) Hydrophobic CdSe/ZnSe/ZnS QDs. (b) PMA- QDs (red line) and PEG-QDs (blue line).*

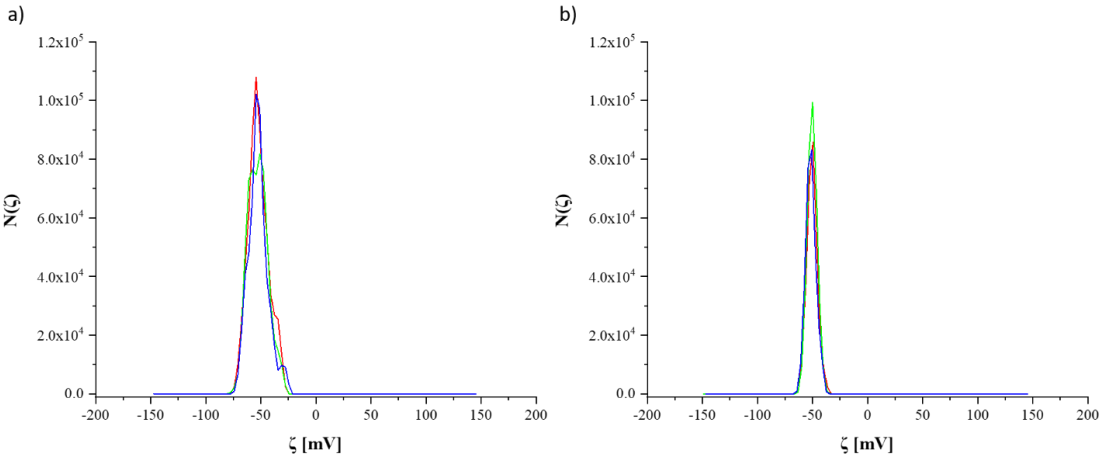

Figure 3-21. *Zeta potential of PMA-QDs and PEG-QDs dispersed in Milli-Q water. (a) PMA-QDs (-52.5 ± 0.44 mV). (b) PEG-QDs (-50.7 ± 0.72 mV).*

3.3.3.2 Protein adsorption measured by FCS

FCS is a technique based on the correlation analysis of the fluctuation of fluorescent particles in a small observation volume in liquid conditions. Some quantitative parameters, such as the diffusional coefficient, triplet, and rotation, can be fitted by applying an appropriate correlation function. By means of the Stokes- Einstein equation, the hydrodynamic size can be acquired *in situ*[132].

Here, we used a one-photon excitation system, after fitting with the correlation function, the diffusional coefficient D can be acquired by applying the following relation:

$$\tau_d = \frac{\omega_r^2}{4D}$$

Therefore, the hydrodynamic radius could be related according to the following Stokes-Einstein equation:

$$r_h = \frac{\kappa_B T}{6\pi\eta D}$$

Where the Boltzmann constant $\kappa_B = 1.38 \times 10^{-23}$ J/K, T = 298.15 K, and η is solution viscosity, in our case, all measurements were conducted at low protein concentration (<125 μM), the viscosity of protein can be ignored, and the total viscosity is the viscosity of water (0.89 mPa·S).

In this study, we performed two independent experiments with two batches of samples. As shown in Figure 3- 22 to Figure 3-25, the autocorrelation curves of NPs incubated in Tf solution and BSA solution were significantly different, either PMA-QDs or PEG-QDs, which demonstrates the hydrodynamic sizes of PMA-QDs and PEG-QDs in Tf solutions or BSA solutions were dynamically changed with different tendencies.

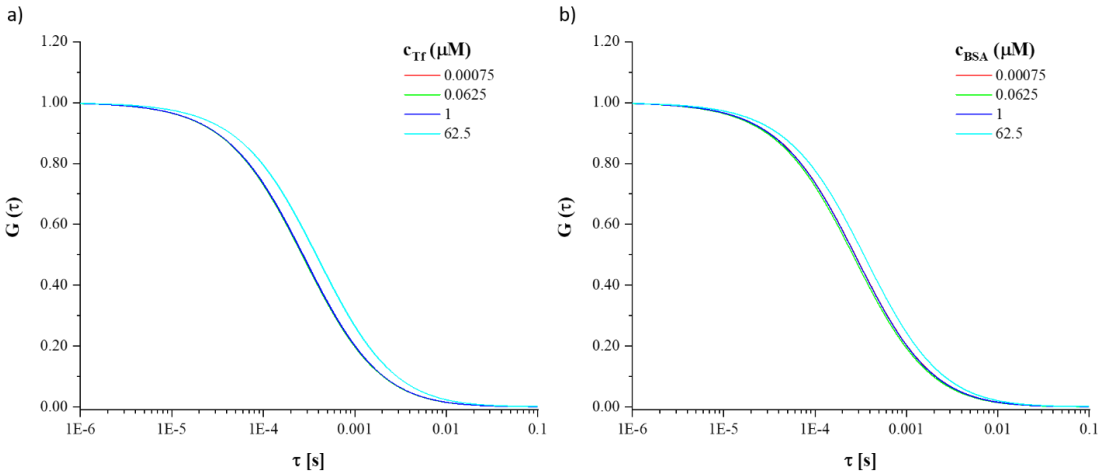

Figure 3-22. *Normalized autocorrelation curves of PMA-QDs dispersed in a series of concentrations of Tf or BSA solutions (only 4 different concentrations were shown, batch 1). (a) in Tf solution. (b) in BSA solution.*

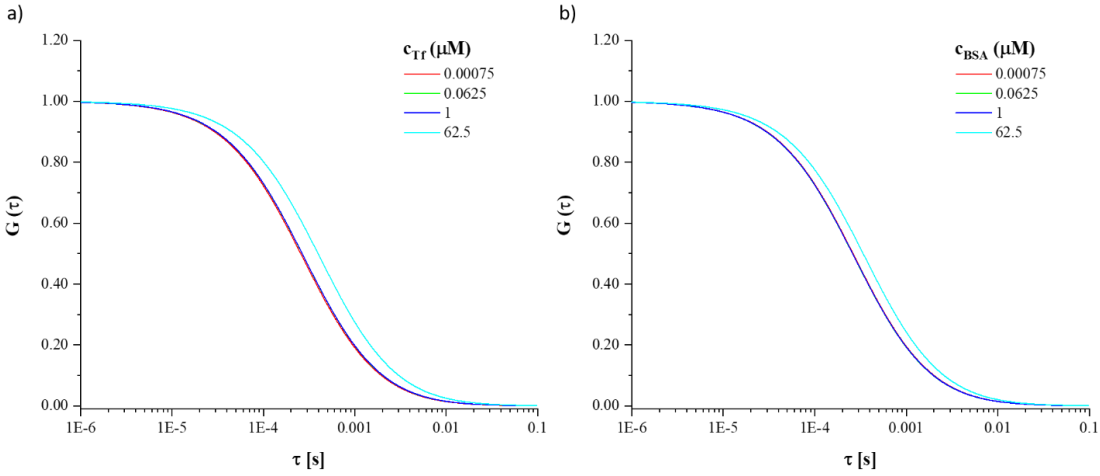

Figure 3-23. *Normalized autocorrelation curves of PMA-QDs dispersed in a series of concentrations of Tf or BSA solutions (only 4 different concentrations were shown, batch 2). (a) in Tf solution. (b) in BSA solution.*

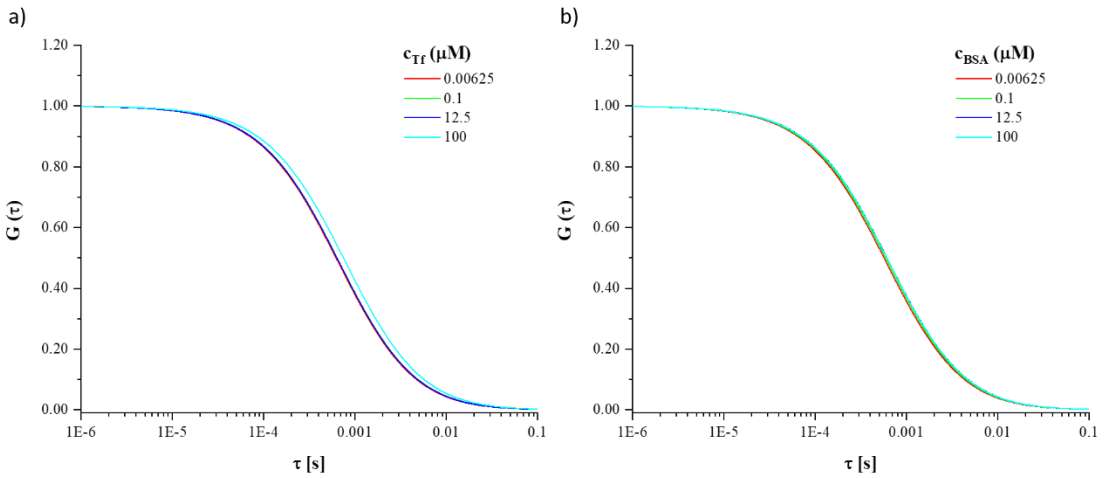

Figure 3-24. *Normalized autocorrelation curves of PEG-QDs dispersed in a series of concentrations of Tf or BSA solutions (only 4 different concentrations were shown, batch 1). (a) in Tf solution. (b) in BSA solution.*

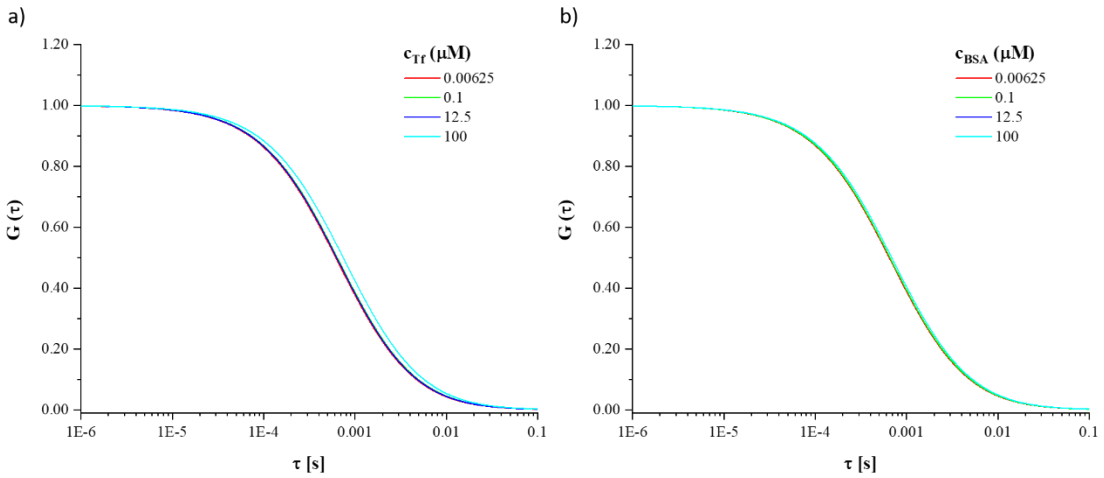

Figure 3-25. *Normalized autocorrelation curves of PEG-QDs dispersed in a series of concentrations of Tf or BSA solutions (only 4 different concentrations were shown, batch 2). (a) in Tf solution. (b) in BSA solution.*

2) Hill model for protein adsorption

As mentioned before, the protein adsorption process is closely related to the hydrodynamic sizes of NPs, therefore, we could monitor the hydrodynamic sizes change to study the binding behavior of different proteins toward different NPs. In the present study, a protein adsorption-hydrodynamic size fitting model was applied, which was widely used in our previous studies[133].

$$r_h(N_{protein}) = r_h(0)\sqrt[3]{1+\frac{V_{protein}}{V_{NP}} * N_{protein}}$$

$N_{protein}$ can be expressed by the Hill equation,

$$N_{protein} = \frac{N_{\max}}{1+(\frac{K'_d}{c(protein)})^n}$$

$N_{protein}$: the number of proteins binding to the NP

$r_h(N_{protein})$: the hydrodynamic size of the NP upon N number of proteins binding

$r_h(0)$: the hydrodynamic size of the NP without protein binding

$V_{protein}$: the volume of a single protein

V_{NP}: the volume of a single NP

N_{max}: the maximum number of proteins binding to the NP

K'_d: the dissociation coefficient

c(protein): the concentration of proteins

n: Hill coefficient

In this case, V_{BSA} is 81.7 nm^3, calculated by $V_{protein}=(M_w/N_A)/\rho_{protein}$, where M_w is the molecular weight of the protein, N_A is Avogadro constant, and $\rho_{protein}$ is the density of the protein. V_{Tf} is 294 nm^3.[134]

Figure 3-26 to Figure 3-29 show the hydrodynamic sizes of NPs-proteins complexes as protein concentration changed, as well as the fitting curves. For PMA-QDs, the hydrodynamic radii increased as the Tf solution

concentration increased within our experimental concentration range (Figure 3-26), while there was a plateau when incubated with BSA solutions (Figure 3-27). However, for PEG-QDs, there was a plateau appeared when the concentration of Tf increased to ca. 20 μM (Figure 3-28), whereas the hydrodynamic radii of PEG- QDs in BSA solutions kept unchanged (Figure 3-29). This result was consistent with a study from the Nienhaus group[135]. There was no albumin adsorption on PEGylated NPs. Interestingly, in our previous study, Pelaz et al. found there was still protein corona formed when PEGylated NPs incubated with albumin, albumin buried within the PEG shell led to half albumin size increase[136]. Of note, in that study, PEGylation was performed via EDC coupling with carboxyl groups of PMA-coated NPs, we believe that the amino groups from PEG molecules enable directly coordinate with the metal atoms from NPs core. In this case, the polymer shell would be a combination of PMA and PEG, therefore, the albumin adsorption in that study was still contributed by PMA rather than PEG.

The fitted parameters including $r_h(0)$, the maximum hydrodynamic radius upon saturating NPs surface with proteins $r_h(N_{max})$, the increase of hydrodynamic radius ΔR, K'_d, Hill coefficient n, and N_{max} were shown in Table 3-7 to Table 3-10. In a summary table shown in Table 3-11, the dissociation constant of BSA towards PMA-QDs (batch 1: 4.11μM, batch 2: 6.57 μM) was lower than that of PEG-QDs (batch 1: 35.59 μM, batch 2: 66.14 μM), indicating the higher binding affinity between BSA and PMA-QDs. For PEG-QDs, since there was no BSA adsorption upon incubation, the value of K'_d was > 1000 μM, meaning the binding between PEG-QDs and Tf was much stronger than BSA.

Up to now, we seem to find the relationship between cellular uptake and protein adsorption. For PMA-coated NPs, the binding with BSA was stronger than Tf, whereas Tf prefers binding with PEGylated NPs, therefore, as more PEGylated NPs internalized, more Tf were introduced into cells than BSA, however, despite lower PMA-coated NPs accumulated in cells, more BSA was delivered into cells due to the strong binding between BSA and PMA shells, suggesting that specific proteins can be better delivered into cells through modifying the surface chemistry of NPs.

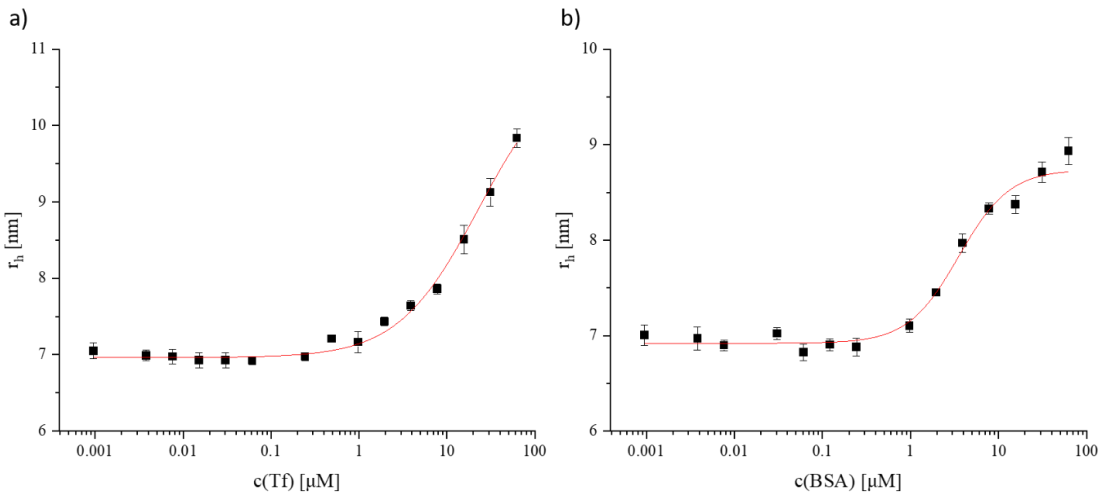

Figure 3-26. *Hydrodynamic radii, r_h, of PMA-QDs as a function of proteins (Tf or BSA) concentration in solution due to protein adsorption (batch 1). (a) in Tf solution. (b) in BSA solution.*

Table 3-7. *Parameters of proteins (Tf or BSA) adsorption onto PMA-QDs derived from the fitting of FCS data (batch 1).*

NP core	***r_c [nm]***	***NP coating***	***Protein***	***T [°C]***	***$r_h(0)$ [nm]***	***$r_h(Nmax)$ [nm]***	***ΔR [nm]***	***K'_D [µm]***	***n***	***N_{max}***
CdSe/ZnSe/ZnS	*5.09*	*PMA*	*Tf*	*25*	*6.96*	*10.795*	*3.83*	*35.59*	*0.98*	*13.42*
CdSe/ZnSe/ZnS	*5.09*	*PMA*	*BSA*	*25*	*6.92*	*8.74*	*1.82*	*4.11*	*1.52*	*17.25*

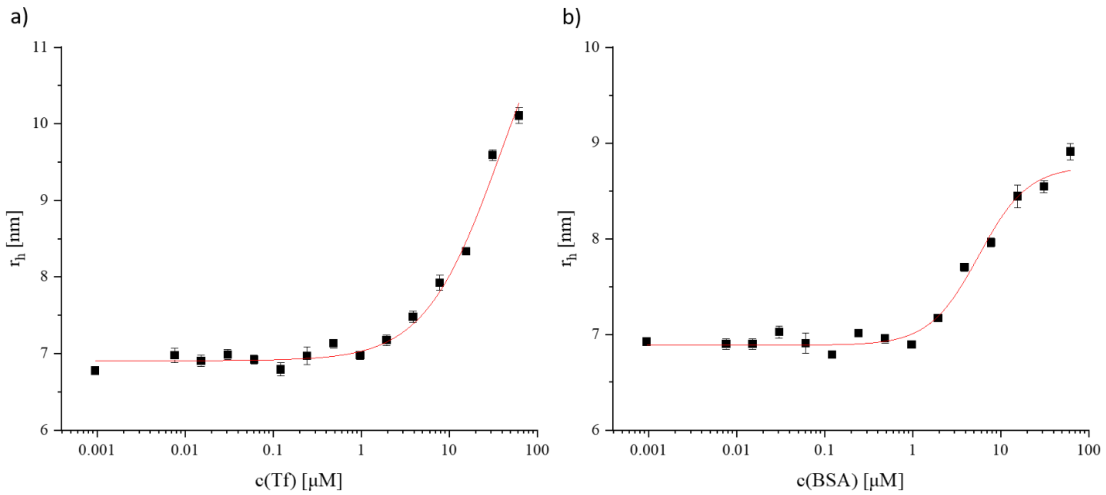

Figure 3-27. *Hydrodynamic radii, r_h, of PMA-QDs as a function of proteins (Tf or BSA) concentration in solution due to protein adsorption (batch 2). (a) in Tf solution. (b) in BSA solution.*

Table 3-8. *Parameters of proteins (Tf or BSA) adsorption onto PMA-QDs derived from the fitting of FCS data (batch 2).*

NP core	***r_c [nm]***	***NP coating***	***Protein***	***T [ºC]***	***$r_h(0)$ [nm]***	***$r_h(Nmax)$ [nm]***	***ΔR [nm]***	***K'$_D$ [µm]***	***n***	***N_{max}***
CdSe/ZnSe/ZnS	*5.09*	*PMA*	*Tf*	*25*	*6.91*	*12.37*	*5.46*	*66.14*	*1.06*	*22.20*
CdSe/ZnSe/ZnS	*5.09*	*PMA*	*BSA*	*25*	*6.89*	*8.76*	*1.87*	*6.57*	*1.56*	*17.68*

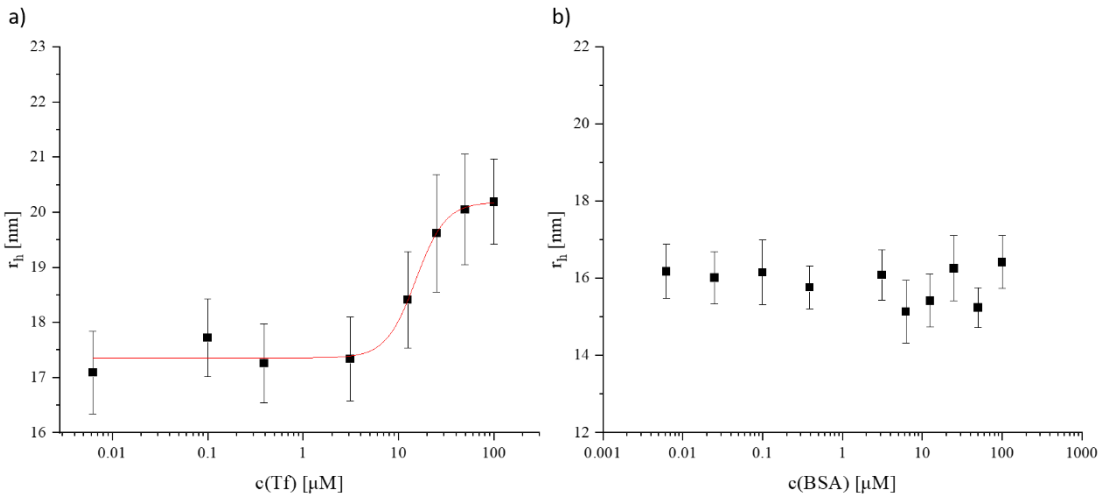

Figure 3-28. *Hydrodynamic radii, r_h, of PEG-QDs as a function of proteins (Tf or BSA) concentration in solution due to protein adsorption (batch 1). (a) in Tf solution. (b) in BSA solution.*

Table 3-9. *Parameters of proteins (Tf or BSA) adsorption onto PEG-QDs derived from the fitting of FCS data (batch 1).*

NP core	***r_c [nm]***	***NP coating***	***Protein***	***T [ºC]***	***$r_h(0)$ [nm]***	***$r_h(Nmax)$ [nm]***	***ΔR [nm]***	***K'_D [µm]***	***n***	***N_{max}***
CdSe/ZnSe/ZnS	*5.57*	*PEG*	*Tf*	*25*	*17.36*	*20.18*	*2.83*	*15.99*	*2.79*	*42.63*
CdSe/ZnSe/ZnS	*5.57*	*PEG*	*BSA*	*25*	-	-	-	-	-	-

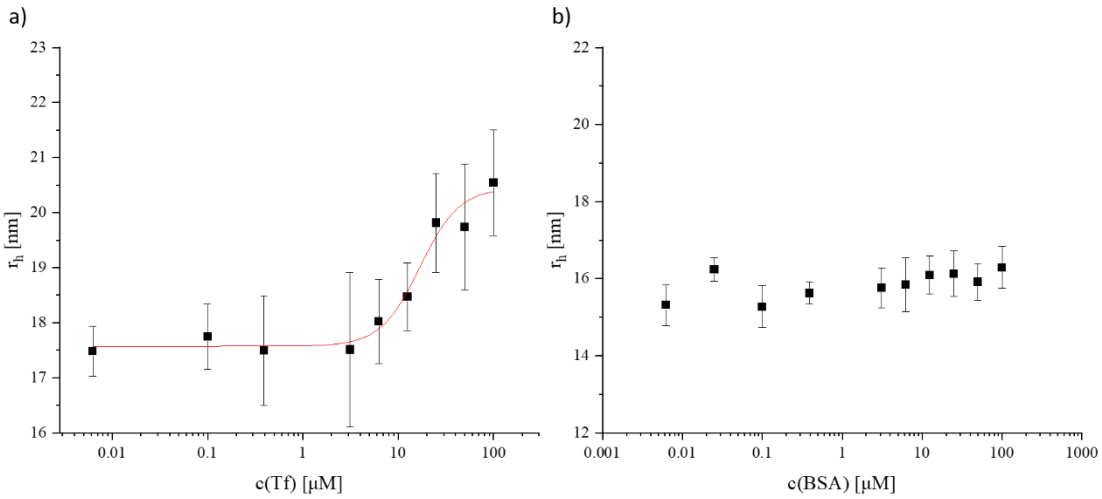

Figure 3-29. *Hydrodynamic radii, r_h, of PEG-QDs as a function of proteins (Tf or BSA) concentration in solution due to protein adsorption (batch 2). (a) in Tf solution. (b) in BSA solution.*

Table 3-10. *Parameters of proteins (Tf or BSA) adsorption onto PEG-QDs derived from the fitting of FCS data (batch 2).*

NP core	***r_c [nm]***	***NP coating***	***Protein***	***T [ºC]***	***$r_h(0)$ [nm]***	***$r_h(Nmax)$ [nm]***	***ΔR [nm]***	***K'$_D$ [µm]***	***n***	***N_{max}***
CdSe/ZnSe/ZnS	*5.57*	*PEG*	*Tf*	*25*	*17.57*	*20.45*	*2.88*	*18.17*	*2.11*	*44.53*
CdSe/ZnSe/ZnS	*5.57*	*PEG*	*BSA*	*25*	-	-	-	-	-	-

Table 3-11. *Dissociation coefficients of PMA-QDs and PEG-QDs upon proteins (Tf or BSA) adsorption.*

Batches	***NP core***	***NP coating***	***Protein***	***K'$_D$ [µM]***
1	*CdSe/ZnSe/ZnS*	*PMA*	*Tf*	*35.59*
1	*CdSe/ZnSe/ZnS*	*PMA*	*BSA*	*4.11*
2	*CdSe/ZnSe/ZnS*	*PMA*	*Tf*	*66.14*
2	*CdSe/ZnSe/ZnS*	*PMA*	*BSA*	*6.57*
1	*CdSe/ZnSe/ZnS*	*PEG*	*Tf*	*15.99*
1	*CdSe/ZnSe/ZnS*	*PEG*	*BSA*	*>1000*
2	*CdSe/ZnSe/ZnS*	*PEG*	*Tf*	*18.17*
2	*CdSe/ZnSe/ZnS*	*PEG*	*BSA*	*>1000*

3.4 Conclusion

Various factors that impact the formation of protein corona and cellular uptake, such as sizes, shapes, surface chemistry, hydrophobicity, charges, etc. In this study, we evaluated the influence of surface chemistry on protein adsorption and subsequent cellular uptake. We prepared two NPs using different surface modification strategies (PMA coating vs PEGylation). In terms of the multi-compartmental nature of NPs in biological environments, we labeled polymer shells of NPs and model proteins with specific elements, incorporating the inorganic core (Au), we built multilabeled NPs-proteins complexes. Taking advantage of the multiplexes element analysis capability of ICP-MS, we investigated the cellular uptake upon NPs-proteins complexes with different surface chemistry exposed to HeLa cells. We discovered that surface modification significantly influenced the formation of the protein corona, subsequently, the cellular uptake was also affected. To address the relationship between protein adsorption and cellular internalization of NPs. We used FCS to quantify the binding affinities of two NPs with different proteins, Tf and BSA. We found BSA prefers binding to PMA shells while there were few adsorbed on PEG shells. In contrast, PEG shells exhibit stronger binding to Tf. Therefore, we revealed the association between protein adsorption and cellular internalization. The surface chemistry of NPs closely controls the formation of the protein corona, we can use PMA-coated NPs to deliver more BSA into cells and introduce more Tf via NPs PEGylation. This study quantitatively proposes a strategy to achieve more precise protein intracellular delivery via optimizing and screening NPs engineering and binding with specific proteins.

4 Improved efficacy of atenolol by conjugating albumin- capped Au NPs

4.1 Introduction

Cardiovascular diseases are the leading cause of death around the world. According to a report from World Health Organization (WHO), there are 17.9 million people died from cardiovascular diseases each year, accounting for the global death toll of 32%[137]. β-adrenergic receptors of cardiomyocytes play an important role in regulating signal transduction and producing cyclic adenosine monophosphate (cAMP) in the pathogenesis of heart failure[138-139]. Stimulation of β-1 adrenergic receptors can induce hypertrophy and promote cardiomyocyte apoptosis[140]. In a previous study from our collaboration partners, Prof. Dr. Viacheslav Nikolaev and Dr. Alexander Froese from Universitätsklinikum Hamburg-Eppendorf (UKE), they found β-1 adrenergic receptors are distributed in both the cardiomyocytes crest and transverse (T)-tubules[141]. T- tubules are sarcolemma invaginations on the myocytes membrane, which only allowed particles below 11 nm to enter inside[142]. However, the contributions of β-1 adrenergic receptors from different areas toward heart function are still poorly understood.

Atenolol, a small molecule medication as a selective β-1 blocker, is widely used to specifically treat heart failure[143]. Owing to the small size itself, it is difficult to selectively block the β-1 adrenergic sub-receptors either in crest or T-tubules. NPs with tunable sizes and intrinsic physicochemical properties are commonly used as carriers of small molecule drugs. These nanodrugs can prolong the blood circulation time, increase drug efficacy, and modify the drug biodistribution in the body[144-146]. However, there are some natural physiological barriers in our bodies. For instance, under a normal healthy condition, the endothelial barrier hinders the transcytosis of most NPs from blood vessels to targeted tissues, which greatly constrains the delivery efficiency of nanodrugs[147-148].

As mentioned in the previous chapters, protein corona is another hurdle for the clinical translation of nanodrugs. Although the understanding of protein corona is still far from clear, an increasing number of people are coming to realize the significance of protein corona in medicine and pharmaceutics[109, 149-150]. Of note, several studies are focusing on how to utilize the protein corona. Compared to the covalent approach, Kah et al. greatly increased the loading capacity of drugs by exploiting the electrostatic interactions between protein corona and DNA as well as doxorubicin[151]. Magro et al. prepared protein corona on polysorbate 80- stabilized NPs by preincubating with apolipoprotein E4[152]. The accumulation of NPs with apolipoprotein E4 corona in the brain was 3-fold higher than NPs without protein corona. Kim et al. developed a cholesterol

conjugated DNA nanostructure to treat liver fibrosis. In that study, lipoproteins in serum were adsorbed to the nanostructure via the higher binding between cholesterol and lipoproteins, subsequently, the increased antisense oligonucleotide targeting TGF-β 1 mRNA was delivered in the liver[153].

In this study, we used Au NPs as the carriers due to their good biocompatibility and controllable sizes[154-157]. BSA was used as the protein corona layer since its excellent transcytosis capability towards capillary[158-159]. To reduce the degradation or separation of BSA from Au NPs, herein, we prepared the BSA corona by chemical conjugation instead of simple incubation. Atenolol was pre-linked with BSA via conjugation. The preparation and characterization of the albumin-atenolol capped Au NPs were performed.

4.2 Experiments and methods

4.2.1 Synthesis of 5 nm Au NPs

The 5 nm Au NPs were synthesized by a modified Brust two-phase method according to the literature[122]. Briefly, a solution of 0.300 g of $HAuCl_4 \cdot 3H_2O$ in 25 mL of Milli-Q water was prepared. 2.170 g of tetraoctylammonium bromide (TOAB, Sigma-Aldrich, #29413-6) were dissolved in 80 mL of toluene (Roth, #9558.1). The two solutions were mixed in a separation funnel and shook gently for 5 min. The toluene phase became deep orange color, and the aqueous phase turned colorless. The gold precursor in the toluene phase was transferred into a 250 mL round flask, followed by adding 25 mL of 353 mM fresh sodium borohydride ($NaBH_4$, Sigma-Aldrich, #452882) dropwise within 1 min. Within this process, the gold precursor was reduced to Au NPs and the solution color turned into red-violet. The gold mixture was transferred into a separation funnel again after 1 h stirring, and the aqueous phase was discarded. Afterward, the toluene phase was washed with HCl (25 mL, 10mM), sodium hydroxide (NaOH, 25 mL, 10mM), and three times Milli-Q water (25 mL) to remove the residual precursors and salts. Then, the Au NPs solution was transferred into a 250 mL round flask and stirred overnight. The next day, 10 mL of dodecanethiol (DDT, Sigma-Aldrich, #471364) were added to the Au NPs solution and heated to 65℃ for 3 h. When the solution was cooled down to room temperature, the NPs were centrifuged at 900 rcf for 5 min and the precipitate was discarded. The supernatant was diluted by adding a certain amount of methanol, which acts as a nonsolvent until the solution turned cloudy. The mixture was centrifuged at 900 rcf for 5 min, the precipitate was collected and resuspended in $CHCl_3$. Finally, the hydrophobic DDT-capped Au NPs were yielded.

To be administered and function in the body, NPs are supposed to be hydrophilic. Here, we used the same PMA coating strategy as in chapter 3 to make 5 nm Au NPs disperse in an aqueous solution. The $R_{P/Area}$ adopted in this case was 100 units/nm^2. After polymer coating, the PMA-coated NPs were purified by

ultracentrifuge at 50,000 rpm for 30 min (three times).

4.2.2 Preparation of BSA-atenolol conjugate

The conjugate of BSA-Atenolol was fabricated by introducing a homobifunctional linker 1,2,7,8- Diepoxyoctane (Sigma-Aldrich, #139564).

4.2.2.1 Conjugation of BSA and atenolol

In a brief procedure, 20 mg of atenolol (1 eq, Sigma-Aldrich,#A7655) was dissolved in 10 mL ethanol (96%, Roth, #T171.2) as solution A. 107.2 μL of 1,2,7,8-Diepoxyoctane with one drop of Milli-Q water was dissolved in another 10 mL of ethanol as solution B. Solution A was added to solution B dropwise and stirred overnight at room temperature. Then, most of the ethanol was slowly evaporated using a rotavapor (ca. 3 mL of ethanol remains to make atenolol soluble). 20 mL of n-hexane (95%, Roth, #3907.1) was added followed by centrifugation at 4,000 rpm for 5 min to remove excess linker. The clear up layer comprising excess linker and n-hexane was carefully discarded, leaving yellowish oil product left in the bottom layer, repeat the centrifugation to further remove the excess linker. The remaining product was evaporated completely dry and redissolved in 10 mL of BBS (50 mM, pH 10) buffer. 25 mg (0.005 eq) of BSA in 10 mL BBS was mixed with the solution above under stirring at room temperature overnight. The resulting BSA-atenolol conjugate was yielded.

4.2.2.2 Purification of BSA-atenolol conjugation

The purification procedure was performed with centrifugation filters, PD10 desalting columns, and UV- Vis spectrophotometer.

In detail, first, we prepared a series of diluted BSA and atenolol solutions in water, respectively. The UV- Vis absorption spectra were recorded and the maximum absorption peaks were determined at 278 nm for BSA and 274 nm for atenolol. Then, the as-prepared BSA-atenolol conjugate was centrifuged using a centrifugation filter (MWCO: 3k Da, 9, 000 rpm, 20 min) to separate excess atenolol molecules followed by redissolving in 3 mL of HEPES buffer (0.1M, pH 8.5). 1 mL of sample was passed the PD10 desalting column (GE Healthcare, #17085101), and the eluent was collected in a 2 mL-Eppendorf tube. Afterward, each 1 mL of HEPES buffer was passed the PD10 column, and 10 tubes of eluents were collected. Before desalting, the PD10 column was equilibrated with the HEPES buffer to allow the HEPES buffer to enter the packed bed completely. UV-Vis absorption spectra of eluent were measured by UV-Vis spectrophotometer. Tubes from No.3 to No.5 were

collected and mixed as the purified BSA-atenolol conjugation. The concentration of resulting BSA-atenolol conjugate was determined by the Bradford assay.

4.2.3 Stability test of BSA-atenolol conjugate

To test the conjugation stability, 1 mL of purified BSA-atenolol conjugate was passed the PD10 desalting column on the 3rd and 10th day again, respectively. The protocol was followed above mentioned. UV- Vis spectra were recorded and compared maximum absorption peaks in each tube.

4.2.4 Attachment of BSA-atenolol conjugate to PMA-coated Au NPs

In order to increase the binding affinity of BSA-atenolol conjugate with PMA-coated Au NPs, the EDC chemistry was adopted to form a stable amide bond among them. 0.77 mg of N- (3- Dimethylaminopropyl)- N′-ethyl- carbodiimide-hydrochloride (EDC, Sigma-Aldrich, #E7750) and 1.15 mg of N-Hydroxysuccinimide (NHS, Sigma-Aldrich, #130672) dissolved in 1 mL of Milli-Q water were mixed with 3.82 mL of PMA-Au NPs at a concentration of 164 nM in MES buffer (0.5 M, pH 6). Afterward, the mixture was incubated at 37°C for 30min under gentle shaking to activate the carboxyl groups of PMA. Next, a centrifugation filter (MWCO: 100k Da, 4,000 rpm, 6min) was used to remove the excess EDC/NHS molecules. The activated PMA- coated Au NPs were re-dissolved in HEPES buffer (0.1 M, pH 8.5) followed by adding 5 mL BSA-atenolol conjugate with a concentration of 1.9 mg/mL in HEPES buffer. The mixture was gently shaken overnight at room temperature. The next day, the buffer was exchanged with Milli-Q water using a centrifugation filter (MWCO: 100k Da, 4,000 rpm, 6min, 3 times), and the samples were purified by ultracentrifugation (40,000 rpm, 30 min) twice. The precipitate (BSA-atenolol@PMA-Au NPs) was collected and redispersed in sterilized water for further characterization. A control group with the same amount of BSA (without atenolol) was also prepared, denoted as BSA@PMA-Au NPs.

4.2.5 cAMP signals measurement

This work was done by our collaboration partner, Dr. Alexander Froese. Briefly, mouse cardiomyocytes were freshly isolated and exposed to different concentrations of BSA-atenolol@PMA-Au NPs and the control group BSA@PMA-Au NPs. The cAMP signals were measured by a fluorescence resonance energy transfer (FRET)-based cAMP sensor. The detailed protocol was referred to in the previous study[160] or our publication in the future.

4.3 Results and discussions

4.3.1 Characterization of BSA-atenolol@PMA-Au NPs

4.3.1.1 Characterization of DDT-capped Au NPs

The hydrophobic DDT-capped Au NPs were characterized by TEM and UV-Vis spectrophotometer. TEM images were taken using a JEOL JEM-1400PLUS microscope under 120 kV by deposition of the sample on top of a copper grid coated with a carbon film. Size distribution measurement was performed with Image J software and the analysis of size distribution and plotting of the histogram were done with Origin software. 100 of NPs were counted and the average diameter of the inorganic core d_{core} was determined to be 5.099 ± 0.653 nm (Figure 4-1). The UV-Vis spectrum of DDT-capped Au NPs was acquired with a UV-Vis spectrophotometer. The plasmonic peak in the absorption spectrum was at 517 nm (Figure 4-2).

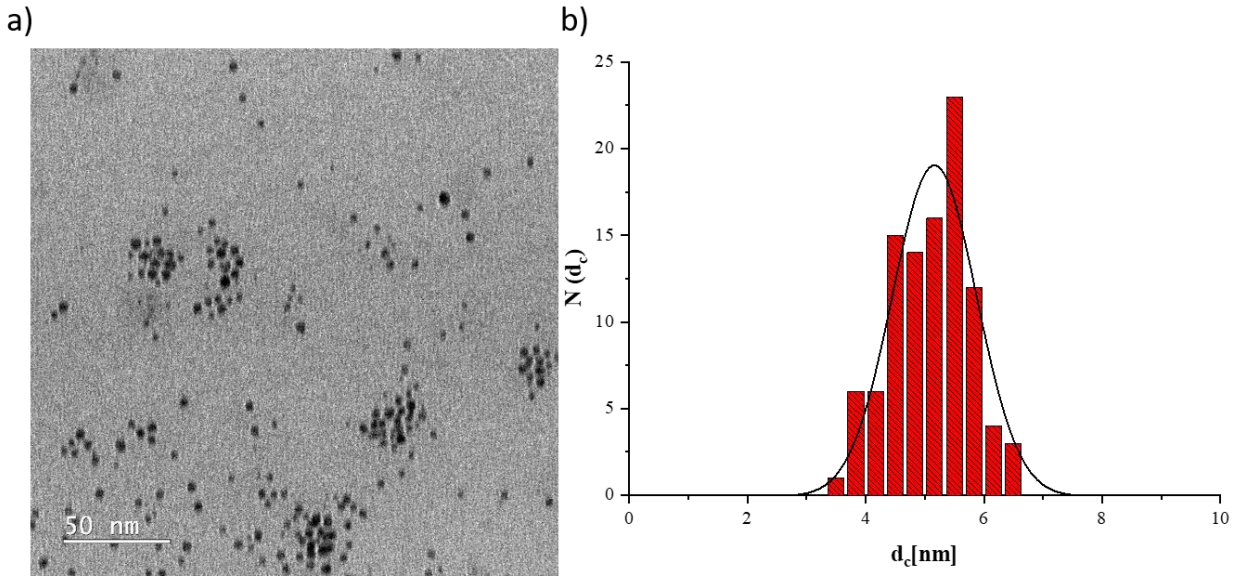

Figure 4-1. *a) TEM image of DDT-capped Au NPs dispersed in $CHCl_3$. (b) Histogram of DDT-capped Au NPs and Gaussian fitting (TEM image was taken by Marta Gallego).*

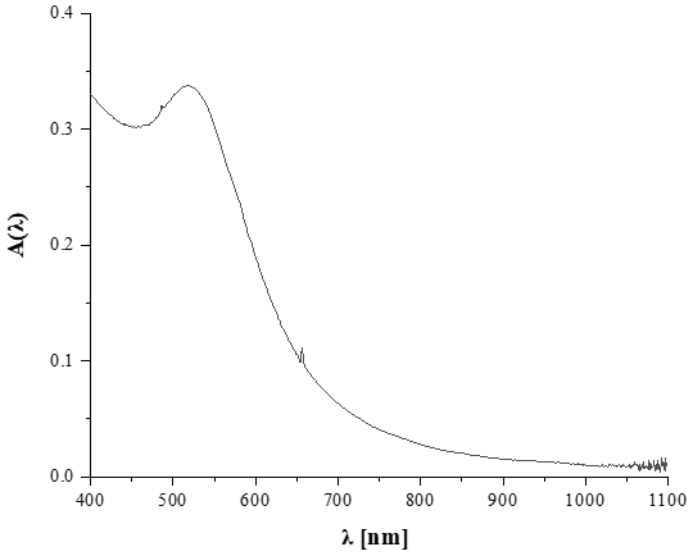

Figure 4-2. *UV-Vis spectrum of DDT-capped Au NPs dispersed in $CHCl_3$ (λ_{spr}: 517 nm).*

4.3.1.2 Purification of BSA-atenolol conjugate

Since BSA and atenolol exhibit different maximum absorption peaks (Figure 4-3), we purified our samples by comparing the UV-Vis spectra of BSA-atenolol conjugate eluent in HEPES buffer. As shown in Figure 4- 4, from tube No.3 to tube No. 5, the spectra were similar to the spectra of BSA alone, which was supposed to be our BSA-atenolol conjugate, and from tube No. 7 to tube No. 10, the spectra were consistent with the spectra of atenolol alone, which corresponding to the free atenolol. Herein, we collected tubes No.3, 4 and, 5 as purified BSA-atenolol conjugate for the following experiments.

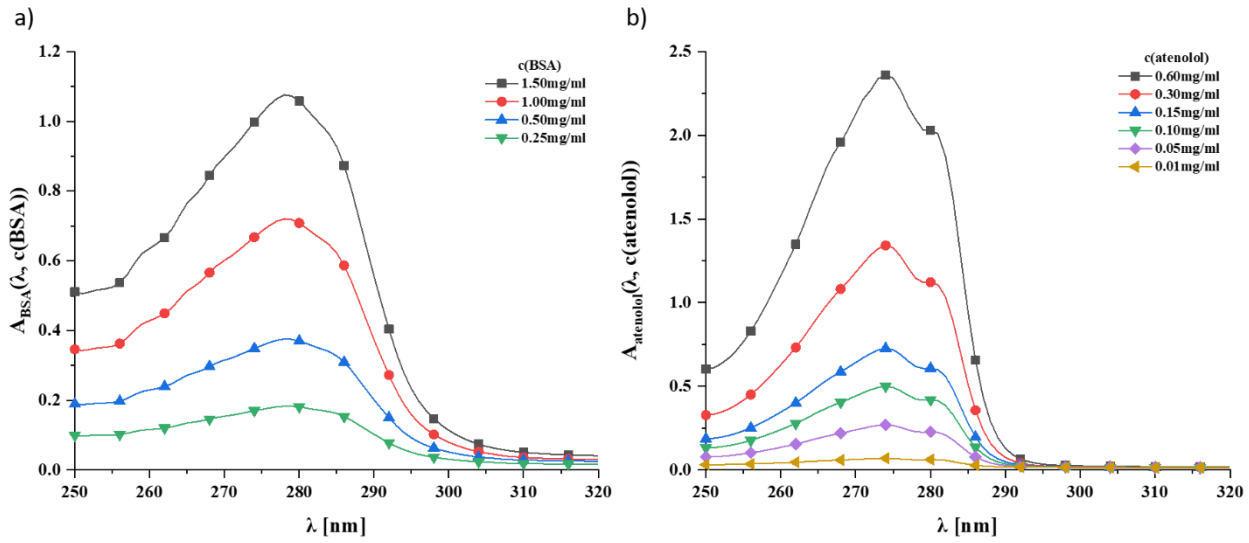

Figure 4-3. *(a) UV-Vis spectra of series of diluted free BSA solutions in Milli-Q water (λ_{BSA_max}: 278 nm). (b) UV-Vis spectra of series of diluted free atenolol solutions in Milli-Q water ($\lambda_{atenolol\_max}$: 274 nm).*

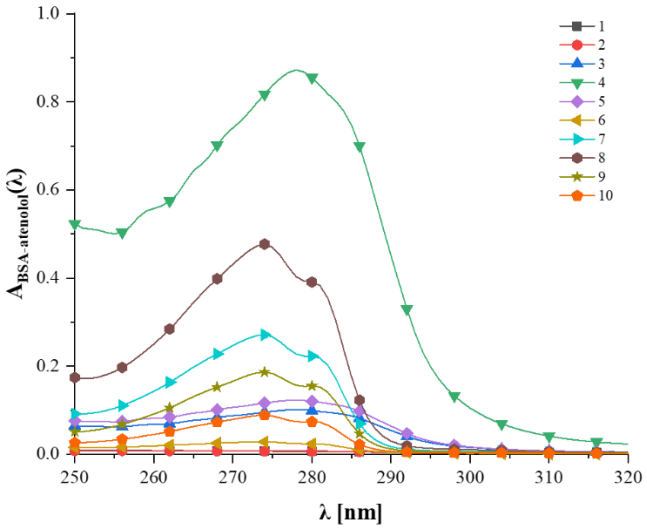

Figure 4-4. *UV-Vis spectra of BSA-atenolol conjugate eluants.*

4.3.1.3 Stability test of BSA-atenolol conjugate

Stability is a critical property for bioconjugated drugs, otherwise, the drugs can not reach the desired targets. Herein, the elutions of purified BSA-atenolol conjugate were collected, and recorded the UV-Vis absorbances (Figure 4-5). Both on the 3rd and 10th day, there was only a maximum absorption peak at 278 nm from tubes No.3 to No.5, while no absorbance was observed from tubes No.7 to No.10, indicating there was no free atenolol released at least within 10 days. Thus, the BSA-atenolol conjugate is persistently stable.

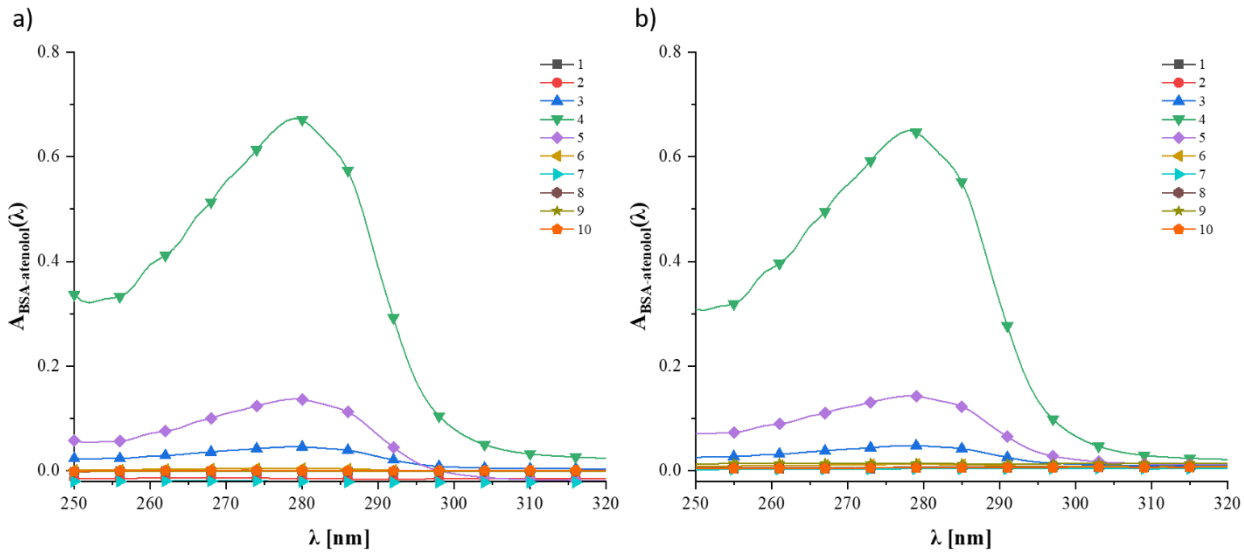

Figure 4-5. *UV-Vis spectra of purified BSA-atenolol conjugate eluants. (a) on the 3rd day, (b) on the 10th day.*

4.3.1.4 Characterization of BSA-atenolol@PMA-Au NPs

The colloidal stability of BSA-atenolol@PMA-Au NPs and BSA@PMA-Au NPs were characterized by the UV-Vis spectrophotometer, DLS, and zeta potential shown in Figure 4-6, Figure 4-7, Figure 4-8, and Figure 4-9. After attaching BSA-atenolol conjugate or BSA, the plasmonic peaks from the UV-Vis spectra were not changed. Both number distribution and intensity distribution of DLS results were monodispersed. In particular, the number distributions were 25.95 ± 0.74 nm and 23.96 ± 1.58 nm, respectively, which are larger than 11 nm, allowing us to selectively bind the β-1adrenergic receptors on the crest of cardiomyocytes. In addition, the zeta potentials were -32.5 ± 0.35 mV (BSA-atenolol@PMA-Au NPs) and -27.4 ± 0.78 mV (BSA@PMA- Au NPs), suggesting good colloidal stability of our samples.

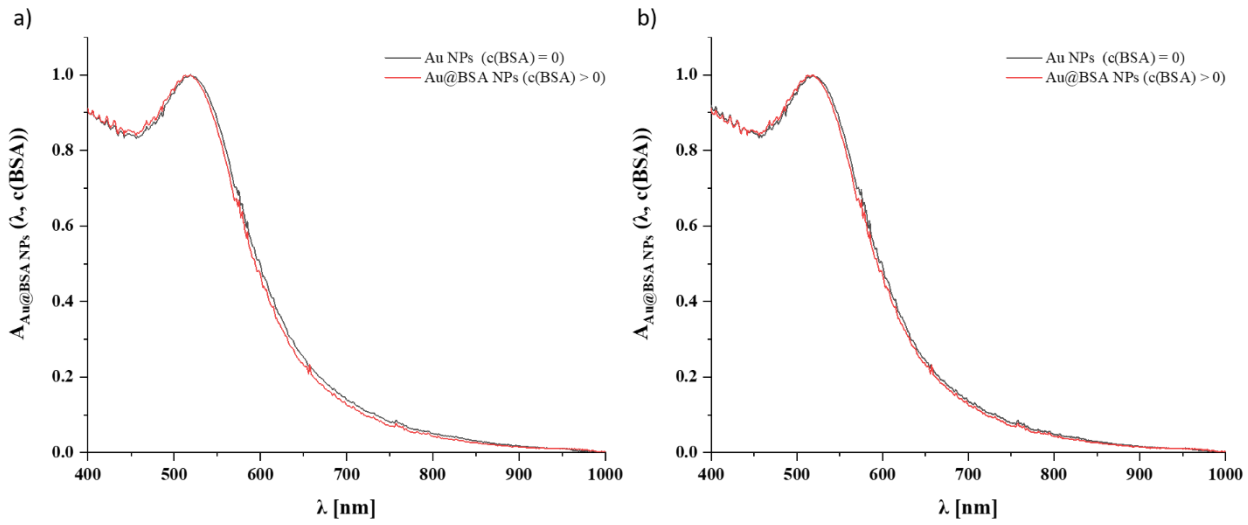

Figure 4-6. *UV-Vis spectra of BSA-atenolol@PMA-Au NPs, BSA@PMA-Au NPs, and PMA-Au NPs. (a) BSA- Atenolol@PMA-Au NPs (red line) and PMA-Au NPs (black line), (b) BSA@PMA-Au NPs (red line) and PMA-Au NPs (black line).*

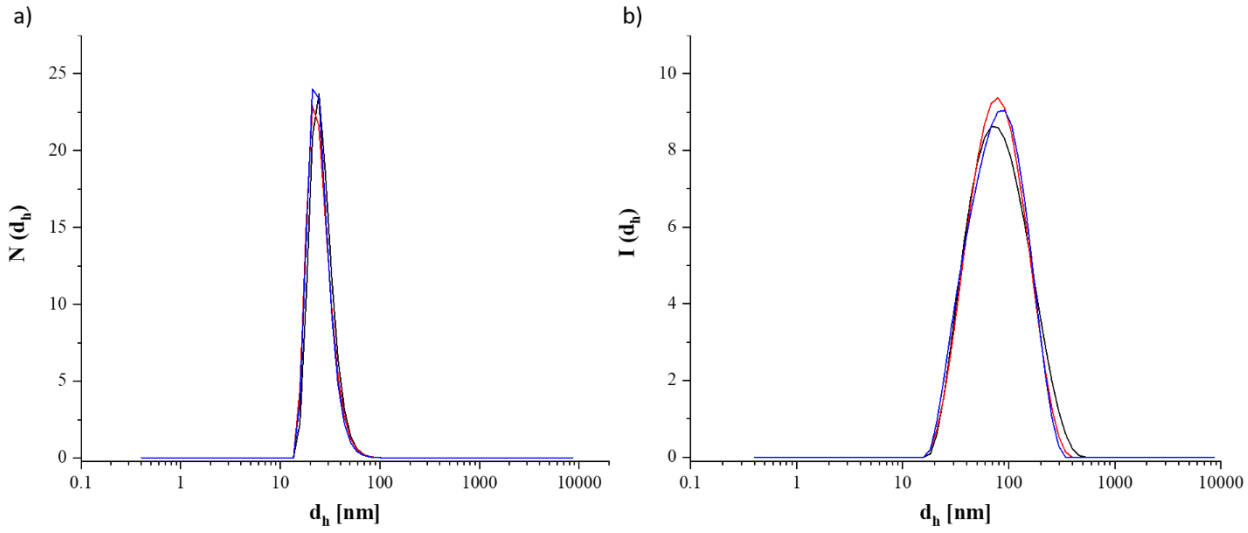

Figure 4-7. *Hydrodynamic diameters of BSA-atenolol@PMA-Au NPs.(a) number distribution (b) intensity distribution.*

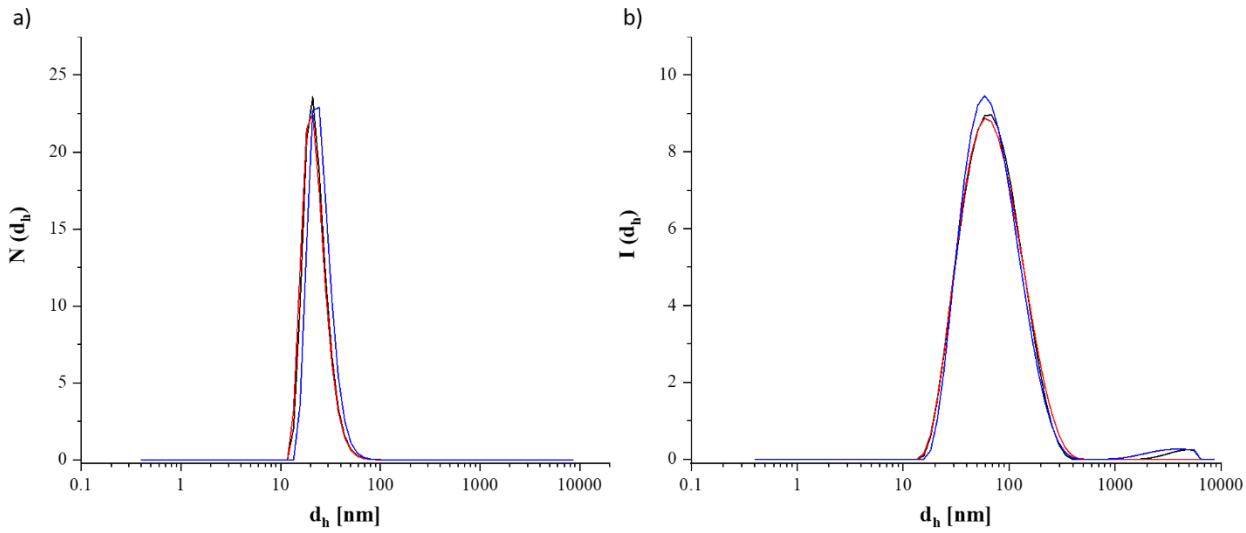

Figure 4-8. *Hydrodynamic diameters of the control sample (BSA@PMA-Au NPs).(a) number distribution (b) intensity distribution.*

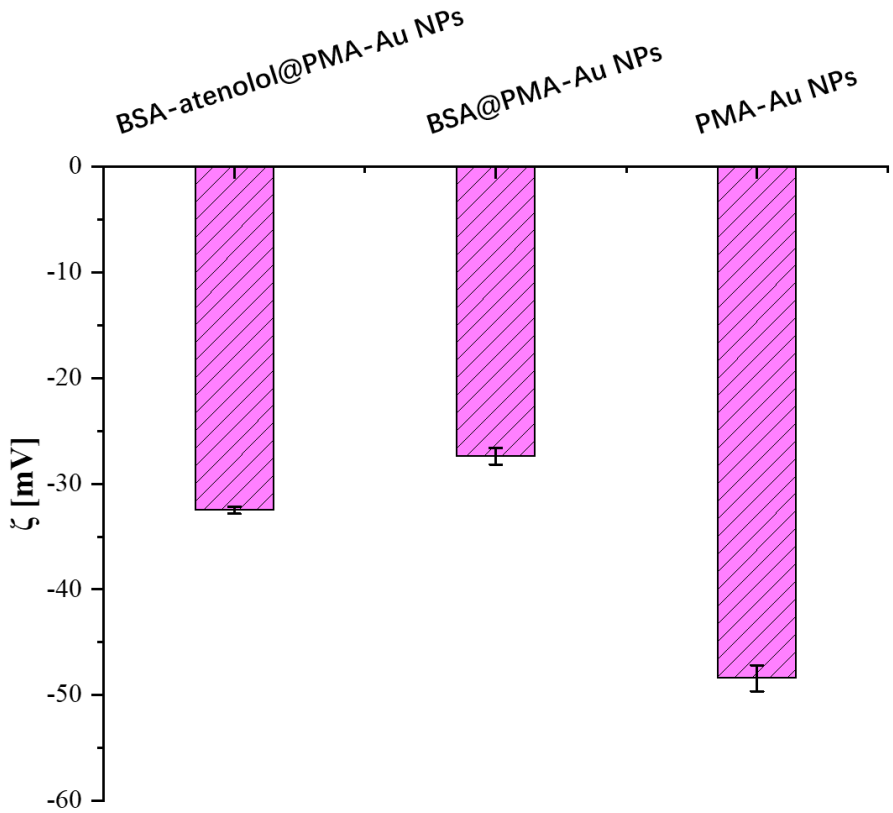

Figure 4-9. *Zeta potentials of BSA-atenolol@PMA-Au NPs， BSA@PMA-Au NPs and PMA-Au NPs.*

4.3.2 Determination of the concentration of Au NPs

The molar concentration of Au NPs was determined by ICP-MS and UV-Vis spectra. Typically, a series of Au NPs with different mass concentrations (c_{mass_AuNPs}) were measured by ICP-MS. Since the radius of Au NPs (r) can be obtained from the TEM image, the mass of one single Au NP (m_{NP}), the number of Au NPs in the series of Au NPs solutions (N), and the molar concentration of the series of Au NPs solutions (c_{molar_AuNPs})were calculated according to the following equations:

$$m_{NP} = 4/3 \cdot \pi \cdot r^3 \cdot \rho_{Au}$$

$$N = c_{mass\_AuNPs} \cdot V / m_{NP}$$

$$c_{molar\_AuNPs} = N / N_A / V$$

where ρ_{Au} is the density of Au (19.32 g/cm^3), V is the volume of Au NPs solution, and N_A is the Avogadro constant.

Then, the UV-Vis spectra of the series of Au NPs solutions were recorded and plotted absorbance at 450 nm versus the molar concentration shown in Figure 4-10. Applying the Lambert-Beer Law, $A_{450} = c_{molar\_AuNPs} \cdot l \cdot \varepsilon_{NP(450)}$, where l = 1 cm was the length of the light path in our cuvette, the molar NP extinction coefficient at 450 nm $\varepsilon_{NP(450)}$ was obtained from the slope. In the present study, $\varepsilon_{NP(450)}$ = 1.65E+7 $M^{-1} \cdot cm^{-1}$. Therefore, for any Au NPs solutions in the following experiments, the molar concentrations were obtained via the UV-Vis absorbance at 450 nm.

4.3.3 Determination of BSA concentration on Au NPs

The protein concentration on the Au NPs was determined by a modified Bradford assay. Since there is a plasmonic peak at 517 nm for 5 nm Au NPs, to determine the concentration of BSA on the Au NPs, the interference of absorbance of Au NPs is supposed to be removed. In a typical procedure, the same concentration of PMA-coated Au NPs was prepared as a blank group to eliminate the influence of absorption of Au NPs. 350 µL of each sample was mixed with 350 µL coomassie reagent and incubated for 10 min at room temperature. The UV-Vis spectra of each sample were recorded after mixing with coomassie blue, and the absorbance of Au NPs was subtracted from the Au@BSA NPs, leading to the absorbance of BSA NPs alone. Next, a net absorbance of BSA NPs at 595 nm was obtained by subtracting the absorbance of the control group. The final concentration of BSA on Au NPs is determined using the calibration curve mentioned in Chapter 3. Herein, after adding coomassie blue dye, the concentration of BSA- atenolol@PMA-Au NPs was diluted and denoted as $c_{w\ com}$(Au NPs), and the concentration of NPs before adding coomassie was designated as $c_{w/o\ com}$(Au NPs). Therefore, combining the influence of dilution of coomassie blue, we have the absorbance

of BSA NPs without Au NPs after adding coomassie blue dye($A_{BSA\ NPs/coomassie}(\lambda, c(BSA))$ (Figure 4-12):

$A_{BSA\ NPs/coomassie}(\lambda, c(BSA)) =$
$A_{Au@BSA\ NPs/coomassie}(\lambda, c(BSA)) - (c_{w\ com}(Au\ NPs)/c_{w/o\ com}(Au\ NPs)) \cdot A_{Au@BSA\ NP}(\lambda, c(BSA))$

Additionally, the absorbance of coomassie blue was also an interference for our quantification. Thus, the PMA-NPs (without BSA) sample was used as the blank sample, denoted as $A_{BSA\ NPs/coomassie}(\lambda, c(BSA) = 0)$. Finally, the absorbance of BSA NPs after excluding all interferences ($\Delta A_{BSA/coomassie}(\lambda, c(BSA) > 0)$ was expressed as follows (Figure 4-13):

$\Delta A_{BSA/coomassie}(\lambda, c(BSA) > 0) = \Delta A_{BSA\ NPs/coomassie}(\lambda, c(BSA) > 0) - \Delta A_{BSA\ NPs/coomassie}(\lambda, c(BSA) = 0)$

Thus, the concentration of BSA on the Au NPs was acquired by applying the calibration curve of BSA mentioned in chapter 3.

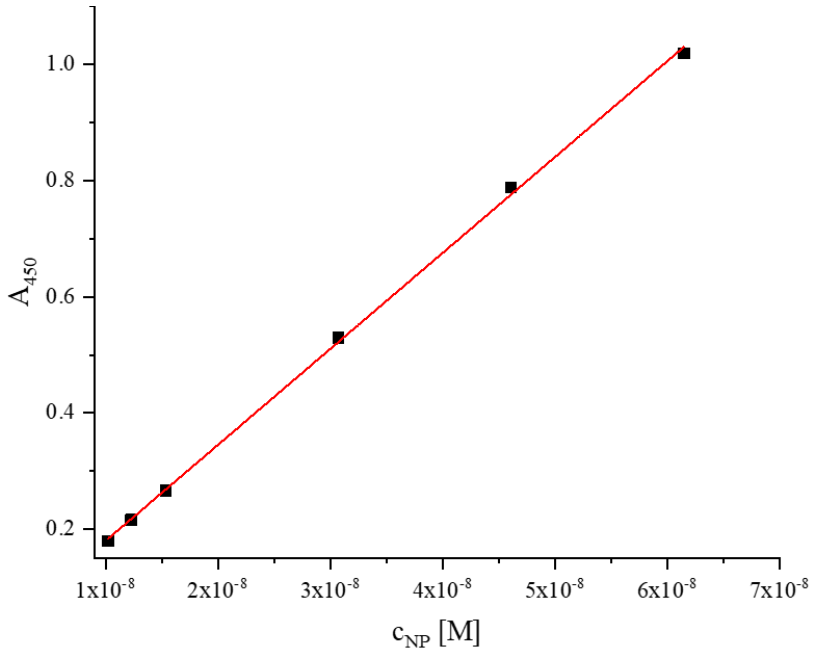

Figure 4-10. *Calibration curve of the absorbance of BSA-atenolol@PMA-Au NPs at 450 nm versus the molar concentration.*

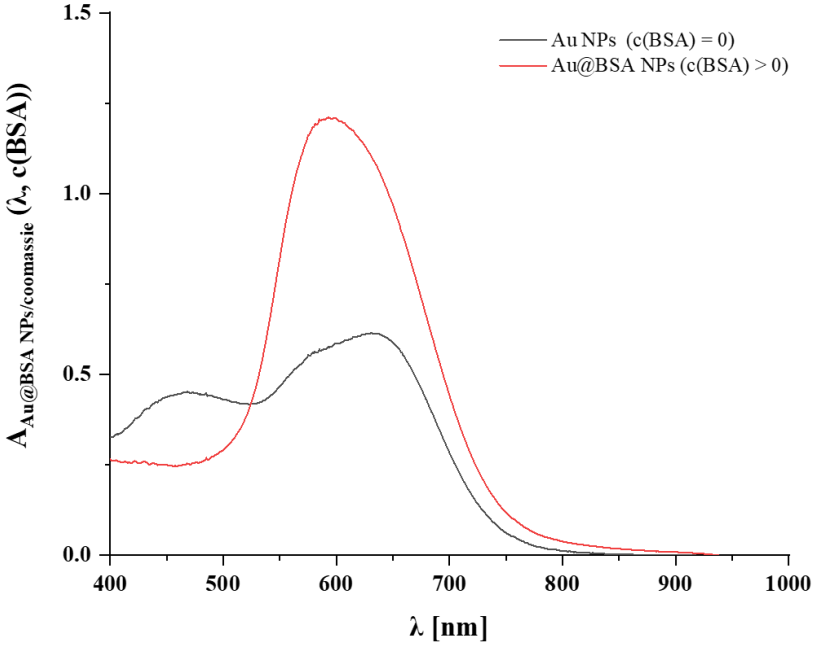

Figure 4-11. *UV-Vis spectra of BSA-atenolol@PMA-Au NPs (red line) and PMA-Au NPs (black line) after adding coomassie blue.*

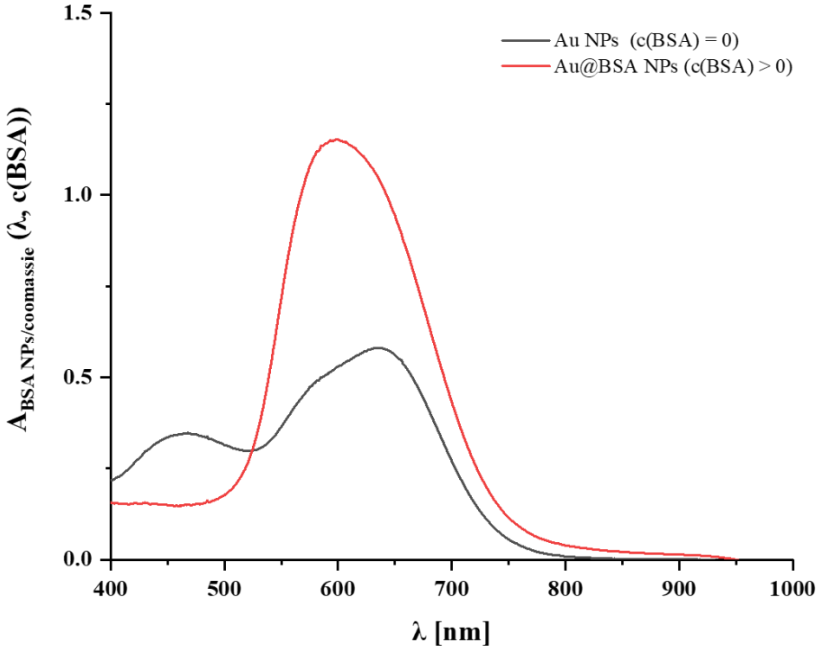

Figure 4-12. *UV-Vis spectra of BSA-atenolol@PMA-Au NPs (red line) and PMA-Au NPs (black line) after removal of the absorbance of Au NPs after adding coomassie blue (i.e. BSA-PMA NPs (red line) and PMA NPs(black line)).*

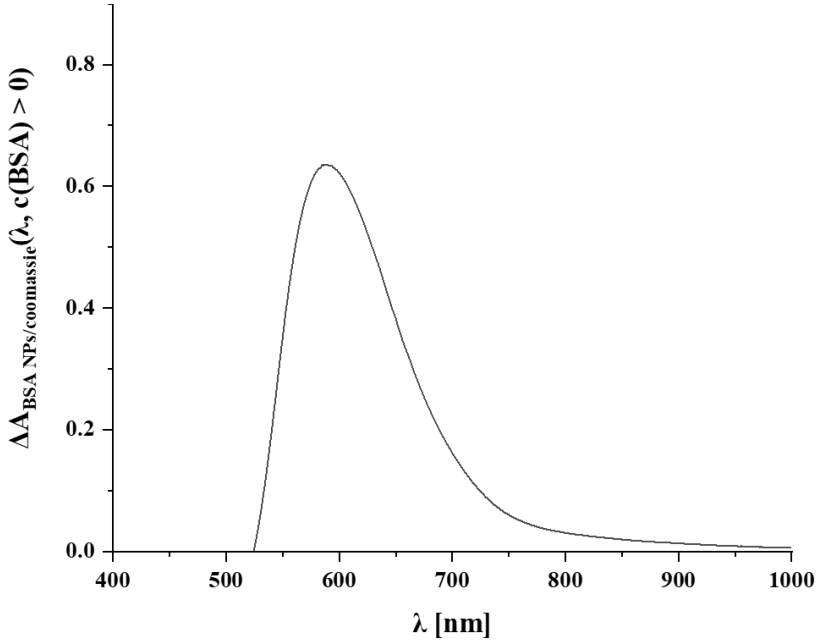

Figure 4-13. *UV-Vis spectra of BSA-atenolol@PMA-Au NPs after subtracting the infererences of Au NPs and coomassie blue after adding coomassie blue (i.e. BSA NPs).*

4.3.4 Calculation of the number of BSA molecules per Au NPs

The number of BSA per Au@BSA NPs was calculated according to the following equations:

$n_{BSA} = m_{BSA} / M_{BSA}$

$n_{NP} = c_{NP} * V$

$N = n_{BSA} / n_{NP}$

n_{BSA} : number of moles of BSA

M_{BSA} : molecular weight of BSA

n_{NP} : number of moles of NPs

c_{NP} : molar concentration of NPs

V : volume

N : number of BSA molecules per NPs

In the present study, the concentrations of BSA and Au NPs can be obtained via Bradford assay and UV- Vis spectra. Therefore, the number of BSA molecules per BSA-atenolol@PMA-Au NPs and BSA@PMA- Au NPs were 25 and 20, respectively.

4.3.5 cAMP responses upon PMA-Au@BSA-atenolol NPs exposure *in vitro*

The dynamic changes of cAMP signals in cardiomyocytes represent the distinct effects of cardiac function, mediated by the adrenergic receptors of cardiomyocytes. By monitoring the alteration of intracellular cAMP signals, the blockade effects of our NPs on β1-adrenergic receptors can be detected. As shown in Figure 4- 14, compared with the control group (BSA@PMA-Au NPs), when our BSA- atenolol@PMA- Au NPs were diluted 3 times, the blockade effect was similar to atenolol alone, which means the BSA-atenolol conjugate was still stable after attaching with Au NPs, and the inhibition effect was decreased as the concentration decreased.

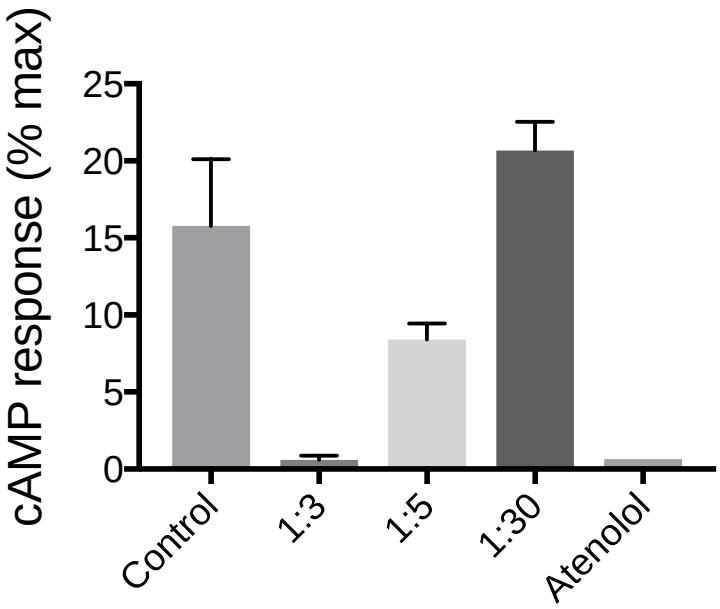

Figure 4-14. *cAMP response of BSA-atenolol@PMA-Au NPs tested in mouse cardiomyocytes (Provided by Dr. Alexander Froese*).

4.4 Conclusion

Heart failure as a global pandemic is increasing in prevalence. Atenolol, a β blocker, can slow the heart's beat and decrease blood pressure by selectively binding the β-1 adrenergic receptors. A previous study of our collaboration partners found there are different subpopulations of β-1 adrenergic receptors distributed in the T- tubules and the crest of cardiomyocytes. However, how the subpopulations of β-1 adrenergic receptors function are still less understood. Herein, we prepared the BSA-atenolol@PMA-Au NPs and evaluated the colloidal stability of NPs, as well as the stability of the BSA-atenolol conjugate. Our *in vitro* experiment indicates that BSA- atenolol@PMA-Au NPs can achieve the same inhibition of cAMP response compared to free atenolol molecules. Furthermore, the BSA-atenolol@PMA-Au NPs can exclusively bind on the subpopulation of the crest β-1 adrenergic receptors, whereas maintaining that in T-Tubules is nonbinding. In this case, we are allowed to more selectively bind the specific β-1 adrenergic receptor subpopulations and improve the therapeutic efficacy of atenolol. In addition, by linking with BSA, the endothelial barrier of NPs delivery was overcome. Therefore, the NPs distribution *in vivo* was also modified. Since the *in vitro* and *in vivo* experiments were done by our partners in UKE, we kindly recommend referring to our publication in the future to know the whole story of this project.

5 Summary and perspective

Although NPs hold great promise in diverse biomedical fields, the interactions between NPs and biological environments are still poorly understood. When exposed to biological fluids, NPs are no longer homogenous entities but are supposed to be hybrid NPs with multi-compartmental nature, including the inorganic core, polymer shell, and biomolecular layer (also called protein corona). Each compartment exhibits a unique role in the application and translation of NPs. For example, the inorganic core can be used as small molecules and biomacromolecules carriers and endow NPs with some unique physicochemical properties. The polymer shell maintains the colloidal stability of NPs in complex biological environments. The biomolecular layer determines NPs' final fate and distributions. Therefore, it is urgently necessary to figure out the biological effects of each compartment of NPs, especially in a quantitative aspect.

In the first study, we quantitatively evaluated the biodistributions of gold (gold salts and Au NPs) and iodine (KI and iohexol) in chamomile via ICP-MS. The different biodistributions of the Au NPs library revealed that both surface chemistry and size are critical for NPs transportation in plants. For instance, some surface ligands such as ACC are more easily transported to petals, probably due to ACC being an amino acid analogy, which is considered a nutrient. Among all the PMA-Au NPs, 31 nm was the simplest size for NPs transportation. In addition, iodine (both KI and iohexol) is also delivered to petals, indicating iodine is another nutrient for plants.

In the second study, we labeled each compartment of NPs with specific elements, then quantitatively investigated the cellular uptake upon exposure to the same Au NPs with two different surface chemistry. We found that surface chemistry mediates the formation of a specific protein corona and plays an important role in cellular internalization. Through FCS measurements, we further quantified the binding affinity between protein corona and NPs, suggesting that proteins can be delivered into cells more efficiently by modifying the surface chemistry of NPs and screening the high binding affinity protein with NPs.

In the third study, we developed a nanomedicine (BSA-atenolol@PMA-Au NPs) to treat heart failure. We conjugated atenolol with BSA and linked it with Au NPs. With NPs, the small molecules, atenolol, can be selectively bound to a subpopulation of β-1 adrenergic receptors in the crest of cardiomyocytes. Meanwhile, BSA facilitates the delivery of NPs to the targets. In this way, we enable a better understanding of the multi- compartmental nature of NPs and exploit the protein corona.

In the future, we will continue our studies in the following three aspects:

1. We will try to collaborate with botanists. By studying the vascular structures of plants, we hope further

address the delivery of NPs, as well as the interaction between NPs and fine vascular structures.

2. Now we know the binding affinity is critical to the formation of the protein corona. Further, we want to build an association between the specific protein corona and cell receptors. For example, to identify which types of cell receptors are responsible for the cellular uptake, how many of these cell receptors exist on the cell membrane, and how these cell receptors mediate the internalization of NPs. Furthermore, how these NPs were degraded after internalization.

3. As there are still few Au NP formulations approved in the clinic, in the next step, we will try other NPs as the alternative choices, such as organic polymers, lipid NPs, silicon NPs, etc. By evaluating the toxicity and efficacy of the NP formulations in multi-aspects, we hope to push this nanomedicine into the clinic in the near future.

References

1. Shang, J.; Ye, G.; Shi, K.; Wan, Y.; Luo, C.; Aihara, H.; Geng, Q.; Auerbach, A.; Li, F., Structural basis of receptor recognition by SARS-CoV-2. *Nature* **2020,** *581* (7807), 221-224.
2. Scudellari, M., How the coronavirus infects cells-and why Delta is so dangerous. *Nature* **2021,** *595* (7869), 640-644.
3. Hoffmann, M.; Kleine-Weber, H.; Schroeder, S.; Krüger, N.; Herrler, T.; Erichsen, S.; Schiergens, T. S.; Herrler, G.; Wu, N.-H.; Nitsche, A.; Müller, M. A.; Drosten, C.; Pöhlmann, S., SARS-CoV-2 Cell Entry Depends on ACE2 and TMPRSS2 and Is Blocked by a Clinically Proven Protease Inhibitor. *Cell* **2020,** *181* (2), 271-280.e8.
4. CDC, Understanding mRNA COVID-19 Vaccines. https://www.cdc.gov/coronavirus/2019-ncov/vaccines/different-vaccines/mrna.html.
5. NNI, https://www.nano.gov/nanotech-101/what/definition.
6. Bayda, S.; Adeel, M.; Tuccinardi, T.; Cordani, M.; Rizzolio, F., The History of Nanoscience and Nanotechnology: From Chemical–Physical Applications to Nanomedicine. *Molecules* **2020,** *25* (1), 112.
7. Krukemeyer, M.; Krenn, V.; Huebner, F.; Wagner, W.; Resch, R., History and possible uses of nanomedicine based on nanoparticles and nanotechnological progress. *J. Nanomed. Nanotechnol* **2015,** *6* (6), 336.
8. Reibold, M.; Paufler, P.; Levin, A. A.; Kochmann, W.; Pätzke, N.; Meyer, D. C., Carbon nanotubes in an ancient Damascus sabre. *Nature* **2006,** *444* (7117), 286-286.
9. Taniguchi, N., On the Basic Concept of Nanotechnology. *Proceedings of the International Conference on Production Engineering* **1974**, 6.
10. Kroto, H. W.; Heath, J. R.; O'Brien, S. C.; Curl, R. F.; Smalley, R. E., C60: Buckminsterfullerene. *Nature* **1985,** *318* (6042), 162-163.
11. Xu, X.; Ray, R.; Gu, Y.; Ploehn, H. J.; Gearheart, L.; Raker, K.; Scrivens, W. A., Electrophoretic Analysis and Purification of Fluorescent Single-Walled Carbon Nanotube Fragments. *Journal of the American Chemical Society* **2004,** *126* (40), 12736-12737.
12. Boehm, H. P.; Clauss, A.; Fischer, G. O.; Hofmann, U., Das Adsorptionsverhalten sehr dünner Kohlenstoff-Folien. *Zeitschrift für anorganische und allgemeine Chemie* **1962,** *316* (3-4), 119-127.
13. Novoselov, K. S.; Geim, A. K.; Morozov, S. V.; Jiang, D.; Zhang, Y.; Dubonos, S. V.; Grigorieva, I. V.; Firsov, A. A., Electric Field Effect in Atomically Thin Carbon Films. *Science* **2004,** *306* (5696), 666-669.
14. Melosh Nicholas, A.; Boukai, A.; Diana, F.; Gerardot, B.; Badolato, A.; Petroff Pierre, M.; Heath James, R., Ultrahigh-Density Nanowire Lattices and Circuits. *Science* **2003,** *300* (5616), 112-115.
15. Zaera, F., Nanostructured materials for applications in heterogeneous catalysis. *Chemical Society Reviews* **2013,** *42* (7), 2746-2762.
16. Daniel, M.-C.; Astruc, D., Gold nanoparticles: assembly, supramolecular chemistry, quantum-size-related properties, and applications toward biology, catalysis, and nanotechnology. *Chemical reviews* **2004,** *104* (1), 293-346.
17. Davis, S., Biomedical applications of nanotechnology—implications for drug targeting and gene therapy. *Trends in biotechnology* **1997,** *15* (6), 217-224.
18. Mitchell, M. J.; Billingsley, M. M.; Haley, R. M.; Wechsler, M. E.; Peppas, N. A.; Langer, R., Engineering precision nanoparticles for drug delivery. *Nature Reviews Drug Discovery* **2021,** *20* (2), 101-124.
19. Dragoman, M., *Atomic-Scale Electronics Beyond CMOS*. 1st ed. 2021. ed.; Springer International Publishing: 2021.
20. *Responsive Nanomaterials for Sustainable Applications*. 1st ed. 2020. ed.; Springer International Publishing: 2020.
21. *Handbook of Nanomaterials and Nanocomposites for Energy and Environmental Applications*. Springer: 2019.
22. Cooper, V. R.; Lam, C. N.; Wang, Y.; Sumpter, B. G., Chapter 14 - Noncovalent Interactions in Nanotechnology. In *Non-Covalent Interactions in Quantum Chemistry and Physics*, Otero de la Roza, A.;

DiLabio, G. A., Eds. Elsevier: 2017; pp 417-451.
23. Moore, T. L.; Rodriguez-Lorenzo, L.; Hirsch, V.; Balog, S.; Urban, D.; Jud, C.; Rothen-Rutishauser, B.; Lattuada, M.; Petri-Fink, A., Nanoparticle colloidal stability in cell culture media and impact on cellular interactions. *Chemical Society Reviews* **2015,** *44* (17), 6287-6305.
24. Lazzari, S.; Moscatelli, D.; Codari, F.; Salmona, M.; Morbidelli, M.; Diomede, L., Colloidal stability of polymeric nanoparticles in biological fluids. *Journal of Nanoparticle Research* **2012,** *14* (6), 920.
25. Feliu, N.; Docter, D.; Heine, M.; del Pino, P.; Ashraf, S.; Kolosnjaj-Tabi, J.; Macchiarini, P.; Nielsen, P.; Alloyeau, D.; Gazeau, F.; Stauber, R. H.; Parak, W. J., In vivo degeneration and the fate of inorganic nanoparticles. *Chemical Society Reviews* **2016,** *45* (9), 2440-2457.
26. Roy, S.; Liu, Z.; Sun, X.; Gharib, M.; Yan, H.; Huang, Y.; Megahed, S.; Schnabel, M.; Zhu, D.; Feliu, N., Assembly and degradation of inorganic nanoparticles in biological environments. *Bioconjugate Chemistry* **2019,** *30* (11), 2751-2762.
27. Silva, G. A., Introduction to nanotechnology and its applications to medicine. *Surgical Neurology* **2004,** *61* (3), 216-220.
28. Mijatovic, D.; Eijkel, J. C. T.; van den Berg, A., Technologies for nanofluidic systems: top-down vs. bottom-up—a review. *Lab on a Chip* **2005,** *5* (5), 492-500.
29. Iqbal, P.; Preece, J. A.; Mendes, P. M., Nanotechnology: The "Top-Down" and "Bottom-Up" Approaches. *Supramolecular Chemistry* **2012**.
30. Porter, L. A.; Choi, H. C.; Schmeltzer, J.; Ribbe, A. E.; Elliott, L. C.; Buriak, J. M., Electroless nanoparticle film deposition compatible with photolithography, microcontact printing, and dip-pen nanolithography patterning technologies. *Nano Letters* **2002,** *2* (12), 1369-1372.
31. Nikam, A. V.; Prasad, B. L. V.; Kulkarni, A. A., Wet chemical synthesis of metal oxide nanoparticles: a review. *CrystEngComm* **2018,** *20* (35), 5091-5107.
32. Pelaz, B.; Alexiou, C.; Alvarez-Puebla, R. A.; Alves, F.; Andrews, A. M.; Ashraf, S.; Balogh, L. P.; Ballerini, L.; Bestetti, A.; Brendel, C.; Bosi, S.; Carril, M.; Chan, W. C. W.; Chen, C.; Chen, X.; Chen, X.; Cheng, Z.; Cui, D.; Du, J.; Dullin, C.; Escudero, A.; Feliu, N.; Gao, M.; George, M.; Gogotsi, Y.; Grünweller, A.; Gu, Z.; Halas, N. J.; Hampp, N.; Hartmann, R. K.; Hersam, M. C.; Hunziker, P.; Jian, J.; Jiang, X.; Jungebluth, P.; Kadhiresan, P.; Kataoka, K.; Khademhosseini, A.; Kopeček, J.; Kotov, N. A.; Krug, H. F.; Lee, D. S.; Lehr, C.-M.; Leong, K. W.; Liang, X.-J.; Ling Lim, M.; Liz-Marzán, L. M.; Ma, X.; Macchiarini, P.; Meng, H.; Möhwald, H.; Mulvaney, P.; Nel, A. E.; Nie, S.; Nordlander, P.; Okano, T.; Oliveira, J.; Park, T. H.; Penner, R. M.; Prato, M.; Puntes, V.; Rotello, V. M.; Samarakoon, A.; Schaak, R. E.; Shen, Y.; Sjöqvist, S.; Skirtach, A. G.; Soliman, M. G.; Stevens, M. M.; Sung, H.-W.; Tang, B. Z.; Tietze, R.; Udugama, B. N.; VanEpps, J. S.; Weil, T.; Weiss, P. S.; Willner, I.; Wu, Y.; Yang, L.; Yue, Z.; Zhang, Q.; Zhang, Q.; Zhang, X.-E.; Zhao, Y.; Zhou, X.; Parak, W. J., Diverse Applications of Nanomedicine. *Acs Nano* **2017,** *11* (3), 2313-2381.
33. Kairdolf, B. A.; Smith, A. M.; Stokes, T. H.; Wang, M. D.; Young, A. N.; Nie, S., Semiconductor quantum dots for bioimaging and biodiagnostic applications. *Annual review of analytical chemistry* **2013,** *6*, 143-162.
34. Lane, L. A.; Qian, X.; Nie, S., SERS nanoparticles in medicine: from label-free detection to spectroscopic tagging. *Chemical reviews* **2015,** *115* (19), 10489-10529.
35. Colombo, M.; Carregal-Romero, S.; Casula, M. F.; Gutiérrez, L.; Morales, M. P.; Böhm, I. B.; Heverhagen, J. T.; Prosperi, D.; Parak, W. J., Biological applications of magnetic nanoparticles. *Chemical Society Reviews* **2012,** *41* (11), 4306-4334.
36. Ferguson, R. M.; Khandhar, A. P.; Kemp, S. J.; Arami, H.; Saritas, E. U.; Croft, L. R.; Konkle, J.; Goodwill, P. W.; Halkola, A.; Rahmer, J., Magnetic particle imaging with tailored iron oxide nanoparticle tracers. *IEEE transactions on medical imaging* **2014,** *34* (5), 1077-1084.
37. Brigger, I.; Dubernet, C.; Couvreur, P., Nanoparticles in cancer therapy and diagnosis. *Adv Drug Deliver Rev* **2012,** *64*, 24-36.
38. Sun, T.; Zhang, Y. S.; Pang, B.; Hyun, D. C.; Yang, M.; Xia, Y., Engineered Nanoparticles for Drug Delivery in Cancer Therapy. *Angewandte Chemie International Edition* **2014,** *53* (46), 12320-12364.
39. Heuer-Jungemann, A.; Feliu, N.; Bakaimi, I.; Hamaly, M.; Alkilany, A.; Chakraborty, I.; Masood, A.;

Casula, M. F.; Kostopoulou, A.; Oh, E.; Susumu, K.; Stewart, M. H.; Medintz, I. L.; Stratakis, E.; Parak, W. J.; Kanaras, A. G., The Role of Ligands in the Chemical Synthesis and Applications of Inorganic Nanoparticles. *Chemical Reviews* **2019,** *119* (8), 4819-4880.
40. Smith, D. K.; Korgel, B. A., The importance of the CTAB surfactant on the colloidal seed-mediated synthesis of gold nanorods. *Langmuir* **2008,** *24* (3), 644-649.
41. Al-Johani, H.; Abou-Hamad, E.; Jedidi, A.; Widdifield, C. M.; Viger-Gravel, J.; Sangaru, S. S.; Gajan, D.; Anjum, D. H.; Ould-Chikh, S.; Hedhili, M. N.; Gurinov, A.; Kelly, M. J.; El Eter, M.; Cavallo, L.; Emsley, L.; Basset, J.-M., The structure and binding mode of citrate in the stabilization of gold nanoparticles. *Nature Chemistry* **2017,** *9* (9), 890-895.
42. Hyeon, T.; Lee, S. S.; Park, J.; Chung, Y.; Na, H. B., Synthesis of Highly Crystalline and Monodisperse Maghemite Nanocrystallites without a Size-Selection Process. *Journal of the American Chemical Society* **2001,** *123* (51), 12798-12801.
43. Park, J.; Lee, E.; Hwang, N.-M.; Kang, M.; Kim, S. C.; Hwang, Y.; Park, J.-G.; Noh, H.-J.; Kim, J.-Y.; Park, J.-H.; Hyeon, T., One-Nanometer-Scale Size-Controlled Synthesis of Monodisperse Magnetic Iron Oxide Nanoparticles. *Angewandte Chemie International Edition* **2005,** *44* (19), 2872-2877.
44. Talapin, D. V.; Mekis, I.; Götzinger, S.; Kornowski, A.; Benson, O.; Weller, H., CdSe/CdS/ZnS and CdSe/ZnSe/ZnS Core−Shell−Shell Nanocrystals. *The Journal of Physical Chemistry B* **2004,** *108* (49), 18826-18831.
45. Pellegrino, T.; Manna, L.; Kudera, S.; Liedl, T.; Koktysh, D.; Rogach, A. L.; Keller, S.; Rädler, J.; Natile, G.; Parak, W. J., Hydrophobic Nanocrystals Coated with an Amphiphilic Polymer Shell: A General Route to Water Soluble Nanocrystals. *Nano Letters* **2004,** *4* (4), 703-707.
46. Lin, C. A. J.; Sperling, R. A.; Li, J. K.; Yang, T. Y.; Li, P. Y.; Zanella, M.; Chang, W. H.; Parak, W. J., Design of an amphiphilic polymer for nanoparticle coating and functionalization. *Small* **2008,** *4* (3), 334-341.
47. Carrillo-Carrion, C.; Bocanegra, A. I.; Arnaiz, B.; Feliu, N.; Zhu, D.; Parak, W. J., Triple-labeling of polymer-coated quantum dots and adsorbed proteins for tracing their fate in cell cultures. *Acs Nano* **2019,** *13* (4), 4631-4639.
48. Colombo, M.; Fiandra, L.; Alessio, G.; Mazzucchelli, S.; Nebuloni, M.; De Palma, C.; Kantner, K.; Pelaz, B.; Rotem, R.; Corsi, F.; Parak, W. J.; Prosperi, D., Tumour homing and therapeutic effect of colloidal nanoparticles depend on the number of attached antibodies. *Nature Communications* **2016,** *7* (1), 13818.
49. Veronese, F. M.; Pasut, G., PEGylation, successful approach to drug delivery. *Drug discovery today* **2005,** *10* (21), 1451-1458.
50. Alconcel, S. N.; Baas, A. S.; Maynard, H. D., FDA-approved poly (ethylene glycol)–protein conjugate drugs. *Polymer Chemistry* **2011,** *2* (7), 1442-1448.
51. Verbeke, R.; Lentacker, I.; De Smedt, S. C.; Dewitte, H., The dawn of mRNA vaccines: The COVID-19 case. *Journal of Controlled Release* **2021,** *333*, 511-520.
52. FDA, FDA Approves Treatment for Rare Blood Disease. https://www.fda.gov/news-events/press-announcements/fda-approves-treatment-rare-blood-disease.
53. Sperling, R. A.; Parak, W. J., Surface modification, functionalization and bioconjugation of colloidal inorganic nanoparticles. *Philosophical Transactions of the Royal Society A: Mathematical, Physical and Engineering Sciences* **2010,** *368* (1915), 1333-1383.
54. Chen, O.; Zhao, J.; Chauhan, V. P.; Cui, J.; Wong, C.; Harris, D. K.; Wei, H.; Han, H.-S.; Fukumura, D.; Jain, R. K.; Bawendi, M. G., Compact high-quality CdSe–CdS core–shell nanocrystals with narrow emission linewidths and suppressed blinking. *Nature Materials* **2013,** *12* (5), 445-451.
55. Lima, T.; Bernfur, K.; Vilanova, M.; Cedervall, T., Understanding the Lipid and Protein Corona Formation on Different Sized Polymeric Nanoparticles. *Scientific Reports* **2020,** *10* (1), 1129.
56. Cedervall, T.; Lynch, I.; Lindman, S.; Berggård, T.; Thulin, E.; Nilsson, H.; Dawson, K. A.; Linse, S., Understanding the nanoparticle–protein corona using methods to quantify exchange rates and affinities of proteins for nanoparticles. *Proceedings of the National Academy of Sciences* **2007,** *104* (7), 2050-2055.
57. Lundqvist, M.; Stigler, J.; Elia, G.; Lynch, I.; Cedervall, T.; Dawson, K. A., Nanoparticle size and surface properties determine the protein corona with possible implications for biological impacts. *Proceedings*

of the National Academy of Sciences **2008,** *105* (38), 14265-14270.
58. Milani, S.; Baldelli Bombelli, F.; Pitek, A. S.; Dawson, K. A.; Rädler, J., Reversible versus Irreversible Binding of Transferrin to Polystyrene Nanoparticles: Soft and Hard Corona. *Acs Nano* **2012,** *6* (3), 2532-2541.
59. Tenzer, S.; Docter, D.; Kuharev, J.; Musyanovych, A.; Fetz, V.; Hecht, R.; Schlenk, F.; Fischer, D.; Kiouptsi, K.; Reinhardt, C., Rapid formation of plasma protein corona critically affects nanoparticle pathophysiology. *Nat Nanotechnol* **2013,** *8* (10), 772-781.
60. Ritz, S.; Schöttler, S.; Kotman, N.; Baier, G.; Musyanovych, A.; Kuharev, J.; Landfester, K.; Schild, H.; Jahn, O.; Tenzer, S.; Mailänder, V., Protein Corona of Nanoparticles: Distinct Proteins Regulate the Cellular Uptake. *Biomacromolecules* **2015,** *16* (4), 1311-1321.
61. Jafari, S.; Izadi, Z.; Alaei, L.; Jaymand, M.; Samadian, H.; Kashani, V. o.; Derakhshankhah, H.; Hayati, P.; Noori, F.; Mansouri, K.; Moakedi, F.; Janczak, J.; Soltanian Fard, M. J.; Fayaz bakhsh, N., Human plasma protein corona decreases the toxicity of pillar-layer metal organic framework. *Scientific Reports* **2020,** *10* (1), 14569.
62. Chen, F.; Wang, G.; Griffin, J. I.; Brenneman, B.; Banda, N. K.; Holers, V. M.; Backos, D. S.; Wu, L.; Moghimi, S. M.; Simberg, D., Complement proteins bind to nanoparticle protein corona and undergo dynamic exchange in vivo. *Nat Nanotechnol* **2017,** *12* (4), 387-393.
63. Sanfins, E.; Augustsson, C.; Dahlbäck, B.; Linse, S.; Cedervall, T., Size-Dependent Effects of Nanoparticles on Enzymes in the Blood Coagulation Cascade. *Nano Letters* **2014,** *14* (8), 4736-4744.
64. Kong, H.; Xia, K.; Ren, N.; Cui, Y.; Liu, R.; Li, Q.; Lv, M.; Shi, J.; Yan, Q.; Cui, Z.; Fan, C.; Zhu, Y.; Wang, L., Serum protein corona-responsive autophagy tuning in cells. *Nanoscale* **2018,** *10* (37), 18055-18063.
65. Bertrand, N.; Grenier, P.; Mahmoudi, M.; Lima, E. M.; Appel, E. A.; Dormont, F.; Lim, J.-M.; Karnik, R.; Langer, R.; Farokhzad, O. C., Mechanistic understanding of in vivo protein corona formation on polymeric nanoparticles and impact on pharmacokinetics. *Nature Communications* **2017,** *8* (1), 777.
66. Wilhelm, S.; Tavares, A. J.; Dai, Q.; Ohta, S.; Audet, J.; Dvorak, H. F.; Chan, W. C. W., Analysis of nanoparticle delivery to tumours. *Nature Reviews Materials* **2016,** *1* (5), 16014.
67. Schöttler, S.; Becker, G.; Winzen, S.; Steinbach, T.; Mohr, K.; Landfester, K.; Mailänder, V.; Wurm, F. R., Protein adsorption is required for stealth effect of poly(ethylene glycol)- and poly(phosphoester)-coated nanocarriers. *Nat Nanotechnol* **2016,** *11* (4), 372-377.
68. Schlenoff, J. B., Zwitteration: Coating Surfaces with Zwitterionic Functionality to Reduce Nonspecific Adsorption. *Langmuir* **2014,** *30* (32), 9625-9636.
69. Wang, M.; Sun, Y.; Cao, X.; Peng, G.; Javed, I.; Kakinen, A.; Davis, T. P.; Lin, S.; Liu, J.; Ding, F.; Ke, P. C., Graphene quantum dots against human IAPP aggregation and toxicity in vivo. *Nanoscale* **2018,** *10* (42), 19995-20006.
70. Rodriguez, P. L.; Harada, T.; Christian, D. A.; Pantano, D. A.; Tsai, R. K.; Discher, D. E., Minimal" Self" peptides that inhibit phagocytic clearance and enhance delivery of nanoparticles. *Science* **2013,** *339* (6122), 971-975.
71. Field, C. B., V. Barros, T.F. Stocker, D. Qin, D.J. Dokken, K.L. Ebi, M.D. Mastrandrea, K.J. Mach, G.-K. Plattner, S.K. Allen, M. Tignor, and P.M. Midgley *Managing the Risks of Extreme Events and Disasters to Advance Climate Change Adaptation*; IPCC, 2012.
72. Kerr Richard, A., Humans Are Driving Extreme Weather; Time to Prepare. *Science* **2011,** *334* (6059), 1040-1040.
73. Agreement, P. In *Paris agreement*, Report of the Conference of the Parties to the United Nations Framework Convention on Climate Change (21st Session, 2015: Paris). Retrived December, HeinOnline: 2015; p 2017.
74. Lewis, S. L., The Paris Agreement has solved a troubling problem. *Nature* **2016,** *532* (7599), 283-283.
75. Buriak, J. M.; Liz-Marzán, L. M.; Parak, W. J.; Chen, X., Nano and Plants. *Acs Nano* **2022,** *16* (2), 1681-1684.
76. Brack, D. In *Forests and climate change*, Proceedings of Background Study Prepared for the

Fourteenth Session of the United Nations Forum on Forests, United Nations Forum on Forests New York, NY, USA: 2019.
77. Bezner-Kerr, R.; McGuire, K. L.; Nigh, R.; Rocheleau, D.; Soluri, J.; Perfecto, I.; Hemming, D., Effects of industrial agriculture on climate change and the mitigation potential of small-scale agro-ecological farms. *Anim Sci Rev* **2011,** *69*.
78. Khanal, R. C., Climate change and organic agriculture. *Journal of Agriculture and Environment* **2009,** *10*, 116-127.
79. Felton, A.; Lindbladh, M.; Brunet, J.; Fritz, Ö., Replacing coniferous monocultures with mixed-species production stands: an assessment of the potential benefits for forest biodiversity in northern Europe. *Forest ecology and management* **2010,** *260* (6), 939-947.
80. Qin, Y.; Xiao, X.; Wigneron, J.-P.; Ciais, P.; Brandt, M.; Fan, L.; Li, X.; Crowell, S.; Wu, X.; Doughty, R.; Zhang, Y.; Liu, F.; Sitch, S.; Moore, B., Carbon loss from forest degradation exceeds that from deforestation in the Brazilian Amazon. *Nature Climate Change* **2021,** *11* (5), 442-448.
81. Wheeler, T.; von Braun, J., Climate Change Impacts on Global Food Security. *Science* **2013,** *341* (6145), 508-513.
82. Hussein, A. K., Applications of nanotechnology to improve the performance of solar collectors–Recent advances and overview. *Renewable and Sustainable Energy Reviews* **2016,** *62*, 767-792.
83. He, X.; Hwang, H.-M., Nanotechnology in food science: Functionality, applicability, and safety assessment. *journal of food and drug analysis* **2016,** *24* (4), 671-681.
84. Navalakhe, R. M.; Nandedkar, T. D., Application of nanotechnology in biomedicine. **2007**.
85. Ali Mansoori, G.; Bastami, T. R.; Ahmadpour, A.; Eshaghi, Z., Environmental application of nanotechnology. *Annual review of nano research* **2008**, 439-493.
86. Sun, Q.; Li, Z.; Searles, D. J.; Chen, Y.; Lu, G.; Du, A., Charge-controlled switchable CO2 capture on boron nitride nanomaterials. *Journal of the American Chemical Society* **2013,** *135* (22), 8246-8253.
87. Jambor, A.; Beyer, M., New cars—new materials. *Materials & design* **1997,** *18* (4-6), 203-209.
88. Zhou, Z.; Zeng, L.; Xiong, G.; Yang, L.; Yuan, H.; Yu, J.; Xu, S.; Wang, D.; Zhang, X.; Liu, H., Multifunctional electrocatalyst of NiCo-NiCoP nanoparticles embedded into P-doped carbon nanotubes for Energy-Saving hydrogen production and upgraded conversion of formaldehyde. *Chemical Engineering Journal* **2021,** *426*, 129214.
89. Lu, J.; Chen, Z.; Ma, Z.; Pan, F.; Curtiss, L. A.; Amine, K., The role of nanotechnology in the development of battery materials for electric vehicles. *Nat Nanotechnol* **2016,** *11* (12), 1031-1038.
90. Cohen, Y.; Yasuor, H.; Tworowski, D.; Fallik, E.; Poverenov, E., Stimuli-Free Transcuticular Delivery of Zn Microelement Using Biopolymeric Nanovehicles: Experimental, Theoretical, and In Planta Studies. *Acs Nano* **2021,** *15* (12), 19446-19456.
91. Kwak, S.-Y.; Lew, T. T. S.; Sweeney, C. J.; Koman, V. B.; Wong, M. H.; Bohmert-Tatarev, K.; Snell, K. D.; Seo, J. S.; Chua, N.-H.; Strano, M. S., Chloroplast-selective gene delivery and expression in planta using chitosan-complexed single-walled carbon nanotube carriers. *Nat Nanotechnol* **2019,** *14* (5), 447-455.
92. Demirer, G. S.; Zhang, H.; Matos, J. L.; Goh, N. S.; Cunningham, F. J.; Sung, Y.; Chang, R.; Aditham, A. J.; Chio, L.; Cho, M.-J., High aspect ratio nanomaterials enable delivery of functional genetic material without DNA integration in mature plants. *Nat Nanotechnol* **2019,** *14* (5), 456-464.
93. Xia, X.; Shi, B.; Wang, L.; Liu, Y.; Zou, Y.; Zhou, Y.; Chen, Y.; Zheng, M.; Zhu, Y.; Duan, J.; Guo, S.; Jang, H. W.; Miao, Y.; Fan, K.; Bai, F.; Tao, W.; Zhao, Y.; Yan, Q.; Cheng, G.; Liu, H.; Jiao, Y.; Liu, S.; Huang, Y.; Ling, D.; Kang, W.; Xue, X.; Cui, D.; Huang, Y.; Cui, Z.; Sun, X.; Qian, Z.; Gu, Z.; Han, G.; Yang, Z.; Leong, D. T.; Wu, A.; Liu, G.; Qu, X.; Shen, Y.; Wang, Q.; Lowry, G. V.; Wang, E.; Liang, X.-J.; Gardea-Torresdey, J.; Chen, G.; Parak, W. J.; Weiss, P. S.; Zhang, L.; Stenzel, M. M.; Fan, C.; Bush, A. I.; Zhang, G.; Grof, C. P. L.; Wang, X.; Galbraith, D. W.; Tang, B. Z.; Offler, C. E.; Patrick, J. W.; Song, C.-P., From mouse to mouse-ear cress: Nanomaterials as vehicles in plant biotechnology. *Exploration* **2021,** *1* (1), 9-20.
94. Hofmann, T.; Lowry, G. V.; Ghoshal, S.; Tufenkji, N.; Brambilla, D.; Dutcher, J. R.; Gilbertson, L. M.; Giraldo, J. P.; Kinsella, J. M.; Landry, M. P., Technology readiness and overcoming barriers to sustainably implement nanotechnology-enabled plant agriculture. *Nature Food* **2020,** *1* (7), 416-425.

95. Hu, P.; An, J.; Faulkner, M. M.; Wu, H.; Li, Z.; Tian, X.; Giraldo, J. P., Nanoparticle charge and size control foliar delivery efficiency to plant cells and organelles. *Acs Nano* **2020,** *14* (7), 7970-7986.
96. Avellan, A.; Yun, J.; Morais, B. P.; Clement, E. T.; Rodrigues, S. M.; Lowry, G. V., Critical Review: Role of Inorganic Nanoparticle Properties on Their Foliar Uptake and in Planta Translocation. *Environmental Science & Technology* **2021,** *55* (20), 13417-13431.
97. Hubbell, J. A.; Chilkoti, A., Nanomaterials for drug delivery. *Science* **2012,** *337* (6092), 303-305.
98. Jiang, Q.; Liu, S.; Liu, J.; Wang, Z. G.; Ding, B., Rationally designed DNA-origami nanomaterials for drug delivery in vivo. *Advanced Materials* **2019,** *31* (45), 1804785.
99. Witwer, K. W.; Wolfram, J., Extracellular vesicles versus synthetic nanoparticles for drug delivery. *Nature Reviews Materials* **2021,** *6* (2), 103-106.
100. Manzari, M. T.; Shamay, Y.; Kiguchi, H.; Rosen, N.; Scaltriti, M.; Heller, D. A., Targeted drug delivery strategies for precision medicines. *Nature Reviews Materials* **2021,** *6* (4), 351-370.
101. Abdel-Mageed, H. M.; AbuelEzz, N. Z.; Radwan, R. A.; Mohamed, S. A., Nanoparticles in nanomedicine: a comprehensive updated review on current status, challenges and emerging opportunities. *Journal of Microencapsulation* **2021,** *38* (6), 414-436.
102. Shukla, R.; Thok, K.; Kakade, S.; Handa, M.; Beg, S., Clinical translation status of nanoformulations. In *Nanoformulation Strategies for Cancer Treatment*, Elsevier: 2021; pp 303-338.
103. Yan, Y.; Gause, K. T.; Kamphuis, M. M.; Ang, C.-S.; O'Brien-Simpson, N. M.; Lenzo, J. C.; Reynolds, E. C.; Nice, E. C.; Caruso, F., Differential roles of the protein corona in the cellular uptake of nanoporous polymer particles by monocyte and macrophage cell lines. *Acs Nano* **2013,** *7* (12), 10960-10970.
104. Reddy, S. T.; van der Vlies, A. J.; Simeoni, E.; Angeli, V.; Randolph, G. J.; O'Neil, C. P.; Lee, L. K.; Swartz, M. A.; Hubbell, J. A., Exploiting lymphatic transport and complement activation in nanoparticle vaccines. *Nature Biotechnology* **2007,** *25* (10), 1159-1164.
105. Dobrovolskaia, M. A.; Aggarwal, P.; Hall, J. B.; McNeil, S. E., Preclinical Studies To Understand Nanoparticle Interaction with the Immune System and Its Potential Effects on Nanoparticle Biodistribution. *Molecular Pharmaceutics* **2008,** *5* (4), 487-495.
106. Deng, Z. J.; Liang, M.; Monteiro, M.; Toth, I.; Minchin, R. F., Nanoparticle-induced unfolding of fibrinogen promotes Mac-1 receptor activation and inflammation. *Nat Nanotechnol* **2011,** *6* (1), 39-44.
107. Xiao, W.; Gao, H., The impact of protein corona on the behavior and targeting capability of nanoparticle-based delivery system. *International Journal of Pharmaceutics* **2018,** *552* (1), 328-339.
108. Mirshafiee, V.; Mahmoudi, M.; Lou, K.; Cheng, J.; Kraft, M. L., Protein corona significantly reduces active targeting yield. *Chemical communications* **2013,** *49* (25), 2557-2559.
109. Cai, R.; Chen, C., The crown and the scepter: roles of the protein corona in nanomedicine. *Advanced Materials* **2019,** *31* (45), 1805740.
110. Piella, J.; Bastús, N. G.; Puntes, V., Size-dependent protein–nanoparticle interactions in citrate-stabilized gold nanoparticles: the emergence of the protein corona. *Bioconjugate chemistry* **2017,** *28* (1), 88-97.
111. Ding, L.; Yao, C.; Yin, X.; Li, C.; Huang, Y.; Wu, M.; Wang, B.; Guo, X.; Wang, Y.; Wu, M., Size, shape, and protein corona determine cellular uptake and removal mechanisms of gold nanoparticles. *Small* **2018,** *14* (42), 1801451.
112. Cheng, X.; Tian, X.; Wu, A.; Li, J.; Tian, J.; Chong, Y.; Chai, Z.; Zhao, Y.; Chen, C.; Ge, C., Protein corona influences cellular uptake of gold nanoparticles by phagocytic and nonphagocytic cells in a size-dependent manner. *ACS applied materials & interfaces* **2015,** *7* (37), 20568-20575.
113. Madathiparambil Visalakshan, R.; González García, L. E.; Benzigar, M. R.; Ghazaryan, A.; Simon, J.; Mierczynska-Vasilev, A.; Michl, T. D.; Vinu, A.; Mailänder, V.; Morsbach, S., The influence of nanoparticle shape on protein corona formation. *Small* **2020,** *16* (25), 2000285.
114. Yu, Q.; Zhao, L.; Guo, C.; Yan, B.; Su, G., Regulating protein corona formation and dynamic protein exchange by controlling nanoparticle hydrophobicity. *Frontiers in bioengineering and biotechnology* **2020,** *8*, 210.
115. Pustulka, S. M.; Ling, K.; Pish, S. L.; Champion, J. A., Protein nanoparticle charge and hydrophobicity govern protein corona and macrophage uptake. *ACS Applied Materials & Interfaces* **2020,** *12*

(43), 48284-48295.
116. Johnston, B. D.; Kreyling, W. G.; Pfeiffer, C.; Schäffler, M.; Sarioglu, H.; Ristig, S.; Hirn, S.; Haberl, N.; Thalhammer, S.; Hauck, S. M., Colloidal stability and surface chemistry are key factors for the composition of the protein corona of inorganic gold nanoparticles. *Advanced Functional Materials* **2017,** *27* (42), 1701956.
117. Stepien, G.; Moros, M.; Pérez-Hernández, M.; Monge, M.; Gutiérrez, L.; Fratila, R. M.; las Heras, M. d.; Menao Guillen, S.; Puente Lanzarote, J. J.; Solans, C., Effect of surface chemistry and associated protein corona on the long-term biodegradation of iron oxide nanoparticles in vivo. *ACS applied materials & interfaces* **2018,** *10* (5), 4548-4560.
118. Qu, S.; Sun, F.; Qiao, Z.; Li, J.; Shang, L., In situ investigation on the protein corona formation of quantum dots by using fluorescence resonance energy transfer. *Small* **2020,** *16* (21), 1907633.
119. Yan, H.; Cacioppo, M.; Megahed, S.; Arcudi, F.; Đorđević, L.; Zhu, D.; Schulz, F.; Prato, M.; Parak, W. J.; Feliu, N., Influence of the chirality of carbon nanodots on their interaction with proteins and cells. *Nature Communications* **2021,** *12* (1), 7208.
120. Miclăuş, T.; Beer, C.; Chevallier, J.; Scavenius, C.; Bochenkov, V. E.; Enghild, J. J.; Sutherland, D. S., Dynamic protein coronas revealed as a modulator of silver nanoparticle sulphidation in vitro. *Nature Communications* **2016,** *7* (1), 1-10.
121. Hadjidemetriou, M.; Al-Ahmady, Z.; Kostarelos, K., Time-evolution of in vivo protein corona onto blood-circulating PEGylated liposomal doxorubicin (DOXIL) nanoparticles. *Nanoscale* **2016,** *8* (13), 6948-6957.
122. Hühn, J.; Carrillo-Carrion, C.; Soliman, M. G.; Pfeiffer, C.; Valdeperez, D.; Masood, A.; Chakraborty, I.; Zhu, L.; Gallego, M.; Yue, Z., Selected standard protocols for the synthesis, phase transfer, and characterization of inorganic colloidal nanoparticles. *Chemistry of Materials* **2017,** *29* (1), 399-461.
123. Kriemen, E.; Holzapfel, M.; Ruf, E.; Rehbein, J.; Maison, W., Synthesis and Structural Analysis of 1,4,7,10-Tetraazacyclododecane-1,4,7,10--tetraazidoethylacetic Acid (DOTAZA) Complexes. *European Journal of Inorganic Chemistry* **2015,** *2015* (32), 5368-5378.
124. Kreyling, W. G.; Abdelmonem, A. M.; Ali, Z.; Alves, F.; Geiser, M.; Haberl, N.; Hartmann, R.; Hirn, S.; De Aberasturi, D. J.; Kantner, K., In vivo integrity of polymer-coated gold nanoparticles. *Nat Nanotechnol* **2015,** *10* (7), 619-623.
125. Ma, X.; Hartmann, R.; Jimenez de Aberasturi, D.; Yang, F.; Soenen, S. J. H.; Manshian, B. B.; Franz, J.; Valdeperez, D.; Pelaz, B.; Feliu, N.; Hampp, N.; Riethmüller, C.; Vieker, H.; Frese, N.; Gölzhäuser, A.; Simonich, M.; Tanguay, R. L.; Liang, X.-J.; Parak, W. J., Colloidal Gold Nanoparticles Induce Changes in Cellular and Subcellular Morphology. *Acs Nano* **2017,** *11* (8), 7807-7820.
126. Liu, X.; Atwater, M.; Wang, J.; Huo, Q., Extinction coefficient of gold nanoparticles with different sizes and different capping ligands. *Colloids and Surfaces B: Biointerfaces* **2007,** *58* (1), 3-7.
127. Präbst, K.; Engelhardt, H.; Ringgeler, S.; Hübner, H., Basic colorimetric proliferation assays: MTT, WST, and resazurin. In *Cell viability assays*, Springer: 2017; pp 1-17.
128. Liu, Z.; Escudero, A.; Carrillo-Carrion, C.; Chakraborty, I.; Zhu, D.; Gallego, M.; Parak, W. J.; Feliu, N., Biodegradation of Bi-labeled polymer-coated rare-earth nanoparticles in adherent cell cultures. *Chemistry of Materials* **2019,** *32* (1), 245-254.
129. Bourquin, J.; Septiadi, D.; Vanhecke, D.; Balog, S.; Steinmetz, L.; Spuch-Calvar, M.; Taladriz-Blanco, P.; Petri-Fink, A.; Rothen-Rutishauser, B., Reduction of nanoparticle load in cells by mitosis but not exocytosis. *Acs Nano* **2019,** *13* (7), 7759-7770.
130. Kim, J.-Y.; Kim, J.-K.; Park, J.-S.; Byun, Y.; Kim, C.-K., The use of PEGylated liposomes to prolong circulation lifetimes of tissue plasminogen activator. *Biomaterials* **2009,** *30* (29), 5751-5756.
131. Kim, K. P.; Cha, J. D.; Jang, E. H.; Klumpp, J.; Hagens, S.; Hardt, W. D.; Lee, K. Y.; Loessner, M. J., PEGylation of bacteriophages increases blood circulation time and reduces T-helper type 1 immune response. *Microbial biotechnology* **2008,** *1* (3), 247-257.
132. Röcker, C.; Pötzl, M.; Zhang, F.; Parak, W. J.; Nienhaus, G. U., A quantitative fluorescence study of protein monolayer formation on colloidal nanoparticles. *Nat Nanotechnol* **2009,** *4* (9), 577-580.
133. Del Pino, P.; Pelaz, B.; Zhang, Q.; Maffre, P.; Nienhaus, G. U.; Parak, W. J., Protein corona formation

around nanoparticles–from the past to the future. *Materials Horizons* **2014,** *1* (3), 301-313.
134. Mahmoudi, M.; Abdelmonem, A. M.; Behzadi, S.; Clement, J. H.; Dutz, S.; Ejtehadi, M. R.; Hartmann, R.; Kantner, K.; Linne, U.; Maffre, P.; Metzler, S.; Moghadam, M. K.; Pfeiffer, C.; Rezaei, M.; Ruiz-Lozano, P.; Serpooshan, V.; Shokrgozar, M. A.; Nienhaus, G. U.; Parak, W. J., Temperature: The "Ignored" Factor at the NanoBio Interface. *Acs Nano* **2013,** *7* (8), 6555-6562.
135. Wang, H.; Shang, L.; Maffre, P.; Hohmann, S.; Kirschhöfer, F.; Brenner-Weiß, G.; Nienhaus, G. U., The Nature of a Hard Protein Corona Forming on Quantum Dots Exposed to Human Blood Serum. *Small* **2016,** *12* (42), 5836-5844.
136. Pelaz, B.; del Pino, P.; Maffre, P.; Hartmann, R.; Gallego, M.; Rivera-Fernández, S.; de la Fuente, J. M.; Nienhaus, G. U.; Parak, W. J., Surface Functionalization of Nanoparticles with Polyethylene Glycol: Effects on Protein Adsorption and Cellular Uptake. *Acs Nano* **2015,** *9* (7), 6996-7008.
137. WHO, https://www.who.int/en/news-room/fact-sheets/detail/cardiovascular-diseases-(cvds).
138. Nikolaev Viacheslav, O.; Moshkov, A.; Lyon Alexander, R.; Miragoli, M.; Novak, P.; Paur, H.; Lohse Martin, J.; Korchev Yuri, E.; Harding Sian, E.; Gorelik, J., β2-Adrenergic Receptor Redistribution in Heart Failure Changes cAMP Compartmentation. *Science* **2010,** *327* (5973), 1653-1657.
139. Bristow, M. R., β-Adrenergic Receptor Blockade in Chronic Heart Failure. *Circulation* **2000,** *101* (5), 558-569.
140. Engelhardt, S.; Hein, L.; Wiesmann, F.; Lohse Martin, J., Progressive hypertrophy and heart failure in β1-adrenergic receptor transgenic mice. *Proceedings of the National Academy of Sciences* **1999,** *96* (12), 7059-7064.
141. Froese, A.; Nikolaev, V. O., Abstract 464: Two Different Microdomains of β1-adrenoreceptor Signaling Revealed by Live Cell Imaging. *Circulation Research* **2017,** *121* (suppl_1), A464-A464.
142. Parfenov, A. S.; Salnikov, V.; Lederer, W. J.; Lukyánenko, V., Aqueous Diffusion Pathways as a Part of the Ventricular Cell Ultrastructure. *Biophysical Journal* **2006,** *90* (3), 1107-1119.
143. Wadworth, A. N.; Murdoch, D.; Brogden, R. N., Atenolol. *Drugs* **1991,** *42* (3), 468-510.
144. Jin, Q.; Deng, Y.; Chen, X.; Ji, J., Rational Design of Cancer Nanomedicine for Simultaneous Stealth Surface and Enhanced Cellular Uptake. *Acs Nano* **2019,** *13* (2), 954-977.
145. Ventola, C. L., Progress in Nanomedicine: Approved and Investigational Nanodrugs. *P T* **2017,** *42* (12), 742-755.
146. Pearce, A. K.; O'Reilly, R. K., Insights into Active Targeting of Nanoparticles in Drug Delivery: Advances in Clinical Studies and Design Considerations for Cancer Nanomedicine. *Bioconjugate Chemistry* **2019,** *30* (9), 2300-2311.
147. Yazdani, S.; Jaldin-Fincati, J. R.; Pereira, R. V. S.; Klip, A., Endothelial cell barriers: Transport of molecules between blood and tissues. *Traffic* **2019,** *20* (6), 390-403.
148. Barua, S.; Mitragotri, S., Challenges associated with penetration of nanoparticles across cell and tissue barriers: A review of current status and future prospects. *Nano Today* **2014,** *9* (2), 223-243.
149. Hamad-Schifferli, K., Exploiting the novel properties of protein coronas: emerging applications in nanomedicine. *Nanomedicine* **2015,** *10* (10), 1663-1674.
150. Simon, J.; Müller, L. K.; Kokkinopoulou, M.; Lieberwirth, I.; Morsbach, S.; Landfester, K.; Mailänder, V., Exploiting the biomolecular corona: pre-coating of nanoparticles enables controlled cellular interactions. *Nanoscale* **2018,** *10* (22), 10731-10739.
151. Kah, J. C. Y.; Chen, J.; Zubieta, A.; Hamad-Schifferli, K., Exploiting the Protein Corona around Gold Nanorods for Loading and Triggered Release. **2012,** - *6* (- 8), - 6740.
152. Dal Magro, R.; Albertini, B.; Beretta, S.; Rigolio, R.; Donzelli, E.; Chiorazzi, A.; Ricci, M.; Blasi, P.; Sancini, G., Artificial apolipoprotein corona enables nanoparticle brain targeting. *Nanomedicine: Nanotechnology, Biology and Medicine* **2018,** *14* (2), 429-438.
153. Kim, K.-R.; Kim, J.; Back, J. H.; Lee, J. E.; Ahn, D.-R., Cholesterol-Mediated Seeding of Protein Corona on DNA Nanostructures for Targeted Delivery of Oligonucleotide Therapeutics to Treat Liver Fibrosis. *Acs Nano* **2022**.
154. Shukla, R.; Bansal, V.; Chaudhary, M.; Basu, A.; Bhonde, R. R.; Sastry, M., Biocompatibility of gold nanoparticles and their endocytotic fate inside the cellular compartment: a microscopic overview. *Langmuir*

2005, *21* (23), 10644-10654.
155. Adewale, O. B.; Davids, H.; Cairncross, L.; Roux, S., Toxicological behavior of gold nanoparticles on various models: Influence of physicochemical properties and other factors. *International journal of toxicology* **2019,** *38* (5), 357-384.
156. Jana, N. R.; Gearheart, L.; Murphy, C. J., Seeding growth for size control of 5− 40 nm diameter gold nanoparticles. *Langmuir* **2001,** *17* (22), 6782-6786.
157. Bastús, N. G.; Comenge, J.; Puntes, V., Kinetically controlled seeded growth synthesis of citrate-stabilized gold nanoparticles of up to 200 nm: size focusing versus Ostwald ripening. *Langmuir* **2011,** *27* (17), 11098-11105.
158. Milici, A. J.; Watrous, N. E.; Stukenbrok, H.; Palade, G. E., Transcytosis of albumin in capillary endothelium. *Journal of Cell Biology* **1987,** *105* (6), 2603-2612.
159. Ghitescu, L.; Fixman, A.; Simionescu, M.; Simionescu, N., Specific binding sites for albumin restricted to plasmalemmal vesicles of continuous capillary endothelium: receptor-mediated transcytosis. *Journal of Cell Biology* **1986,** *102* (4), 1304-1311.
160. Börner, S.; Schwede, F.; Schlipp, A.; Berisha, F.; Calebiro, D.; Lohse, M. J.; Nikolaev, V. O., FRET measurements of intracellular cAMP concentrations and cAMP analog permeability in intact cells. *Nature Protocols* **2011,** *6* (4), 427-438.

Acknowledgment

Four years are long enough for a person to have scientific training, to become a scientist, whereas four years are also so short that I still do not have much time to improve my German, or experience the German culture. I still remember the first day I came to Hamburg alone, it was the first time I came to a foreign country, and for me everything was new. But soon, the friendly passersby, conversable taxi driver, and also my kind landlady made me feel so safe and comfortable in Hamburg. Since then, I realized Hamburg should be a lovely city and started my Ph.D. training here. Now, the four years journey is coming to the end, it is pleasant and unforgettable. It will be one of the most important experiences in my life. At this moment, I would like to thank everyone who helped, supported, and accompanied me during my Ph.D. life, especially during the annoying COVID-19 pandemic, I cannot finish my Ph.D. research without these people. In particular, I want to thank the following people who played significant roles in my Ph.D. study.

First of all, I would like to thank Prof. Dr. Wolfgang J. Parak for allowing me to study in his group. He guided me enter into the new field of nano-bio interaction, I think I will work for it all my life. I was deeply impressed by his rigorous attitude toward science, which is also greatly influencing me and my academic career in the future. I appreciate his recommendation letter for my postdoctoral position, now I have a chance to go deeper into life science with NPs.

I want to thank Dr. Neus Feliu Torres for her supervision of my experiments. She brought a relaxing and pleasant atmosphere to this group, and she can always give me some detailed suggestions, particularly her pursing to control variables. I benefit quite a lot from it.

I would like to give a special thanks to Dr. Alaaldin M. Alkilany, who taught me how to do science correctly. He made me down-to-earth and showed me how to conduct a scientific experiment independently. Although he only supervised me for one year, I cherish the time working with him. It means a lot.

Thank Yang Liu for the Au NPs library preparation and analysis in the chamomile project. Many thanks to Dr. Huijie Yan for the help in cell experiments and flow cytometry. Thank Dr. Malte Holzapfel for the DOTA chelator labeling and purification. Thank Dr. Alexander Froese for the cell experiments in the cardiovascular project. Thank Marta Gallego, Andreas Kornowski, and Stefan Werner for kindly taking the TEM images.

Also, I would like to thank my colleagues for providing a comfortable environment. I have spent wonderful four years with them. Thank Marten Rittner for his help in many lab stuff.

I am grateful to acknowledge China Scholarship Council for providing my Ph.D. scholarship. It changed my career and also my life.

Last but not least, I would like to thank my parents, who give me endless love and make me feel infinite power all the time. Love them forever.

Abbreviations

NPs	nanoparticles
ICP-MS	inductively coupled plasma mass spectrometry
Au	gold
HeLa	human cervical cancer cells
BSA	bovine serum albumin
RBD	receptor-binding domain
NNI	National Nanotechnology Initiative
Ag	silver
STM	scanning tunneling microscope
AFM	atomic force microscope
SPM	scanning probe microscope
EUV	extreme ultraviolet lithography
QDs	quantum dots
SERS	surface-enhanced Raman scattering
MRI	magnetic resonance imaging
MPI	magnetic particle imaging
EPR	enhanced permeability and retention
CTAB	cetyltrimethylammonium bromide
NRs	nanorods
PBS	phosphate buffer
PMA	poly (isobutylene-alt-maleic anhydride)-graft-dodecyl
DDA	dodecylamine
PEG	poly (ethylene glycol)
PEO	polyethylene oxide
FDA	U.S. Food and Drug Administration
$CHCl_3$	chloroform
GQDs	graphene quantum dots
IAPP	islet amyloid polypeptide
$HAuCl_4 \bullet 3H_2O$	gold (III) chloride trihydrate
KI	Potassium iodide
ATT	6-aza-2-thiothymine

ACC	acetylcysteine
m/z	mass-to-charge
HCl	hydrochloric acid
TEM	transmission electron microscopy
UV-Vis	ultraviolet-visible
DLS	dynamic light scaterring
EMA	European medicines agency
THP-1	human monocytic cells
dTHP-1	differentiated macrophage-like cells
FCS	fluorescence correlation spectroscopy
Gd	gadolinium
DOTA	1,4,7,10-tetraazacyclododecane-1,4,7,10-tetraacetic acid
PET	positron emission tomography
SPECT	single-photon emission computed tomography
Gd_2O_3	gadolinium (III) oxide
NH_4OAc	ammonium acetate
THF	tetrahydrofuran
DMF	dimethylformamide
BBS	borate buffered saline
$GdCl_3 \cdot 6H_2O$	gadolinium (III) chloride hexahydrate
MES	4- Morpholineethanesulfonic acid
EDC	N-(3-Dimethylaminopropyl)-N′-ethyl carbodiimide hydrochloride
Tf	holo-bovine-transferrin
$EuCl_3$	europium (III) chloride
HEPES	N-2-Hydroxyethylpiperazine-N'-2-ethane sulphonic acid
SDS-PAGE	sodium dodecyl sulfate-polyacrylamide gel electrophoresis
ATCC	American Type Culture Collection
FBS	fetal bovine serum
P/S	Penicillin-Streptomycin
HNO_3	nitric acid
CAN	Fraunhofer Zentrum für Angewandte Nanotechnologie
R6G	rhodamine 6G
ω_r	lateral focus radius
ω_z	axial focus radius

CPM	counts per molecule
S/N	signal-to-noise
$G(\tau)$	correlation function
A	amplitude
N	average number of molecules in the observation volume
i	index of component (1, 2, 3)
Φ_i	fractional intensity
f_i	fraction of molecules
η_i	molecular brightness
$\tau_{d,i}$	diffusional correlation time
S	structural parameter
α_i	anomaly parameter
D	diffusional coefficient
κ_B	Boltzmann constant
$N_{protein}$	the number of proteins binding to the NP
$r_h(N_{protein})$	the hydrodynamic size of the NP upon N number of proteins binding
$r_h(0)$	the hydrodynamic size of the NP without protein binding
$V_{protein}$	the volume of a single protein
V_{NP}	the volume of a single NP
N_{max}	the maximum number of proteins binding to the NP
K'_d	the dissociation coefficient
c(protein)	the concentration of proteins
n	Hill coefficient
M_w	molecular weight
N_A	Avogadro constant
$\rho_{protein}$	the density of the protein
ΔR	the increase in hydrodynamic radius
WHO	World Health Organization
cAMP	cyclic adenosine monophosphate
UKE	Universitätsklinikum Hamburg-Eppendorf
TOAB	tetraoctylammonium bromide
$NaBH_4$	sodium borohydride
NaOH	sodium hydroxide
DDT	dodecanethiol

NHS	N-Hydroxysuccinimide
FRET	fluorescence resonance energy transfer
c_{mass_AuNPs}	the mass concentration of Au NPs
m_{NP}	the mass of one single NP
c_{molar_AuNPs}	the molar concentration of Au NPs
r	the radius of Au NPs
ρ_{Au}	the density of Au
V	the volume of Au NPs solution
$\varepsilon_{NP(450)}$	the molar NP extinction coefficient at 450 nm
l	the length of the light path of the cuvette
$c_{w\ com}$(Au NPs)	the concentration of Au NPs after adding coomassie blue
$c_{w/o\ com}$(Au NPs)	the concentration of Au NPs before adding coomassie blue
n_{BSA}	the number of moles of BSA
M_{BSA}	the molecular weight of BSA
n_{NP}	the number of moles of NPs
c_{NP}	the molar concentration of NPs

Publications

1. Sanchez-Cano, C.; Alvarez-Puebla, R. A.; Abendroth, J. M.; Beck, T.; Blick, R.; Cao, Y.; Caruso, F.; Chakraborty, I.; Chapman, H. N.; Chen, C.; **Qi, B.**, X-ray-based techniques to study the nano–bio interface. *Acs Nano* **2021,** *15* (3), 3754-3807.
2. Kang, Y.; Nack, L. M.; Liu, Y.; **Qi, B.**; Huang, Y.; Liu, Z.; Chakraborty, I.; Schulz, F.; Ahmed, A. A.; Clavo Poveda, M., Quantitative considerations about the size dependence of cellular entry and excretion of colloidal nanoparticles for different cell types. *ChemTexts* **2022,** *8* (1), 1-8.
3. Liu, Y.; Körnig, C.; **Qi, B.**; Schmutzler, O.; Staufer, T.; Sanchez-Cano, C.; Magel, E.; Feliu, N.; Grüner, F.; Parak, W.; Size- and ligand-dependent transport of nanoparticles in Matricaria chamomile as demonstrated by mass spectroscopy and X-ray fluorescence imaging. *Acs Nano* **2022,** *16* (8), 12941-12951.

Eidesstattliche Versicherung/ Declaration on oath

Hiermit versichere ich an Eides statt, die vorliegende Dissertationsschrift selbst verfasst und keine anderen als die angegebenen Hilfsmittel und Quellen benutzt zu haben.

Hamburg, den 09.06.2022

Bing Qi